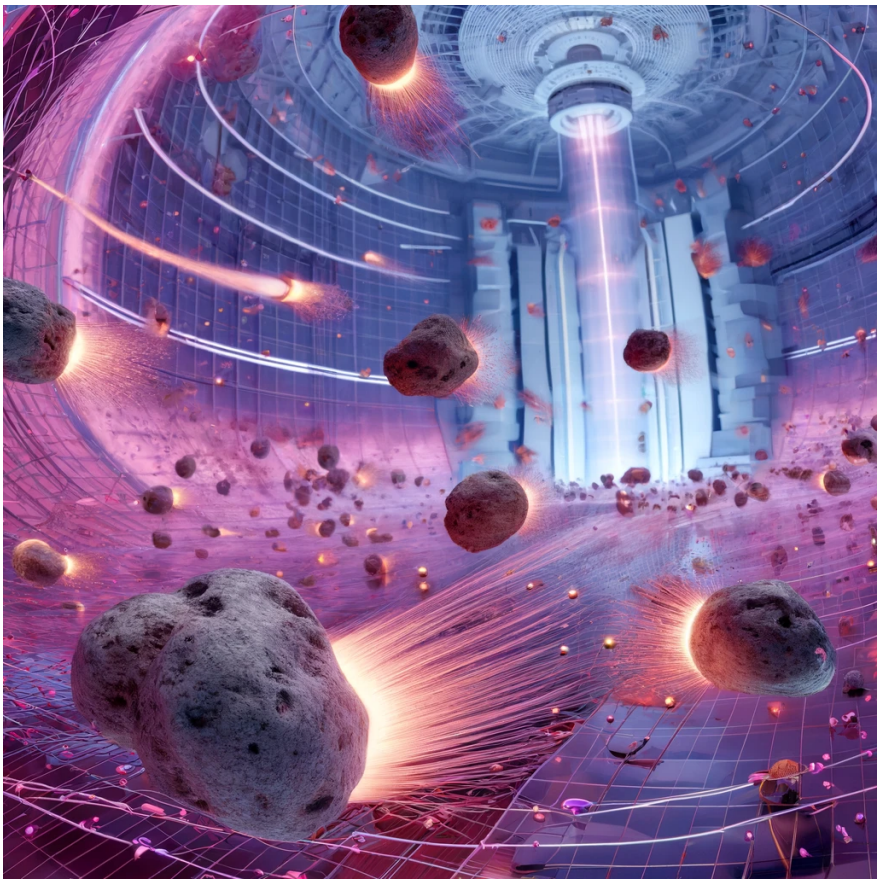

(This image was created with the assistance of AI and does not reflect reality.)

The pellet rocket effect in magnetic confinement fusion plasmas

Thesis for the degree of Master of Science in Physics

NICO JOEL GUTH

DEPARTMENT OF PHYSICS

CHALMERS UNIVERSITY OF TECHNOLOGY
Gothenburg, Sweden 2024
www.chalmers.se

Master's Thesis 2024

The pellet rocket effect in magnetic confinement fusion plasmas

NICO JOEL GUTH

CHALMERS
UNIVERSITY OF TECHNOLOGY

Department of Physics
Division of Subatomic, High Energy and Plasma Physics
Plasma Theory Research Group
Chalmers University of Technology
Gothenburg, Sweden 2024

The pellet rocket effect in magnetic confinement fusion plasmas

Supervisors: Oskar Vallhagen, Department of Physics
István Pusztai, Department of Physics
Sarah Newton, Department of Physics and
Culham Centre for Fusion Energy (UK)
Examiner: Tünde Fülöp, Department of Physics

Master's Thesis 2024
Department of Physics
Division of Subatomic, High Energy and Plasma Physics
Plasma Theory Research Group
Chalmers University of Technology
SE-412 96 Gothenburg
Sweden
Telephone +46 31 772 1000

Cover: Artist's impression of pellets in a tokamak being accelerated by rocket-like dynamics. This image was created with the assistance of AI. It does not reflect any physical reality, and the illustrated dynamics and structures are portrait incorrectly.

Typeset in LaTeX
Gothenburg, Sweden 2024

The pellet rocket effect in magnetic confinement fusion plasmas
Nico Joel Guth
Department of Physics
Chalmers University of Technology

Abstract

Nuclear fusion power generation is widely regarded as a promising technology for a clean and sustainable future. To achieve positive energy gain from fusion, the fuel (deuterium and tritium) has to be sustained at temperatures around ten times hotter than the core of the sun. Most of the power plant designs are currently based on magnetic confinement fusion (MCF), where this fusion plasma is isolated and compressed by strong magnetic fields. Refuelling, control of the plasma density profile and mitigation of off-normal events (disruptions) are done by injecting fast tiny pellets of dense frozen material, which quickly disintegrate from the extreme heat in the fusion plasma. While the efficiency of this material deposition in the plasma depends on the pellet trajectory, the dynamics involved are poorly understood. This thesis develops a semi-analytical model for the so-called *pellet rocket effect*, which accelerates and deflects pellets in a fusion plasma. Asymmetries in the heat flux onto the pellet surface enhance the ablation on one side of the pellet. Consequently, the pellet is pushed in the opposite direction to the ejected material, similarly to a rocket. This effect was shown in experiments to significantly modify the pellet trajectory. Projections for reactor scale devices indicate that it may even stop the pellet before it reaches the plasma core, which would severely limit the effectiveness of pellet injection methods. Our model predicts magnitudes of the pellet rocket acceleration (10^5 to $10^6\,\mathrm{m/s^2}$) similar to the results of more sophisticated simulations and experimental observations. Thus, the essential physics of the pellet rocket effect are successfully captured in our model. With further validation and potential improvements, we expect that this approach can be used to inform the planning and operation of pellet injection in future power plants.

Keywords: fusion plasma, magnetic confinement, pellet injection, ablation, pellet rocket acceleration, asymmetric heating, NGS model

Acknowledgements

I hereby want to express my deepest gratitude towards all the wonderful people who made my time at Chalmers and in Gothenburg, a truly unforgettable experience. Not only did all of them fill my journey with joy, but each person uniquely supported me in achieving this master's degree. First, I want to deeply thank my examiner Tünde for giving me the opportunity to work on this thesis project at the Chalmers Plasma Theory group. She creates an environment that enables everyone to flourish, both personally and academically. Tünde provided me with invaluable guidance for both my thesis and also for my scientific career in general. Next, I am incredibly thankful towards my main supervisor, Oskar, who spent countless hours explaining and discussing in detail the ideas and concepts behind my thesis. Without Oskar, I would have never been able to carry out this project. Additionally, all of my supervisors, Oskar, István, Sarah and Tünde gave me fantastic feedback and advice during our weekly meetings and by thoroughly reviewing everything I have written in this thesis. I could have never imagined receiving such excellent supervision, and I greatly appreciate all the time and effort they invested in supporting me. I also want to thank Per Helander for allowing us to expand on his ideas about modelling the pellet rocket effect and for the fruitful discussions we had. Overall, every member of the Chalmers Plasma Theory group made the everyday experience at the office very enjoyable, and I am grateful to each one of them. Last but not least, I want to thank all of my friends and family, both here in Gothenburg and in Germany, for their support and for bringing immense amounts of happiness into my life.

Nico Joel Guth, Gothenburg, June 2024

List of Acronyms

Below is the list of acronyms that have been used throughout this thesis, listed in alphabetical order:

AUG	ASDEX Upgrade tokamak
HFS	high-field side
LFS	low-field side
MCF	magnetic confinement fusion
NGS	neutral gas shielding
SPI	shattered pellet injection

Contents

1

Introduction

One of the main challenges of the 21st century is finding sustainable ways for humanity to use and generate energy, while the demand for electrical energy is constantly growing. Therefore, new power plants are being built worldwide and the efficiency of power generation technology has to be improved through continuous research. At the same time, climate change forces us to shift from burning fossil fuels, such as coal or gas, to renewable energy sources, such as solar or wind power, thereby reducing the emission of greenhouse gases (IPCC, 2023). However, most renewable energy sources rely on environmental conditions, leading to a time-varying amount of produced power (Chen, 2011).

An alternative to fossil fuels for baseload power plants is nuclear power. Instead of releasing the energy stored in the chemical bonds of the fuel, nuclear power uses the binding energy between the protons and neutrons inside atomic nuclei. Not only does this reduce the direct emission of greenhouse gases to virtually zero, it also increases the efficiency of energy released per mass of fuel by a factor of around a million. Two different types of nuclear energy generation are possible, nuclear fission and nuclear fusion. While nuclear fission has been in use supplying power to the electricity grid since 1954, nuclear fusion is the only naturally occurring energy source that humanity does not directly use yet. Both concepts use the same fundamental physics principles. However, the technology needed for controlled power generation differs drastically.

1.1 Nuclear fusion as a sustainable energy source

Nuclear fission is the process of splitting heavy atomic nuclei such as certain uranium isotopes into lighter atomic nuclei. The total mass of the reaction products can be smaller than that of the reactants. Energy conservation and the equivalence of energy and mass, as described by Einstein's famous equation $E = mc^2$, means that the mass difference has to be converted into energy. The resulting kinetic energy of the fission products or additional photons can then be extracted in the form of heat. Nuclear fusion uses the opposite process, where light nuclei such as various hydrogen isotopes are combined into heavier nuclei, and again the mass of the fusion products is less than the combined mass before fusion. At first sight, it might seem unreasonable that energy can be gained by both breaking apart or creating nuclear bonds. However, the energy needed to break nuclear bonds depends heavily on

the number of protons and neutrons in the nucleus, as shown in fig. 1.1. Breaking apart, for example, deuterium (H^2 or D) into hydrogen (H^1) and a neutron requires around[1] 2 MeV. Therefore, the fusion process $H^1 + n \rightarrow H^2$ releases 2 MeV of energy. For elements lighter than iron (Fe^{56}), the binding energy generally increases with the number of nucleons and here a fusion process releases energy, but for heavier elements the binding energy decreases and fission releases energy.

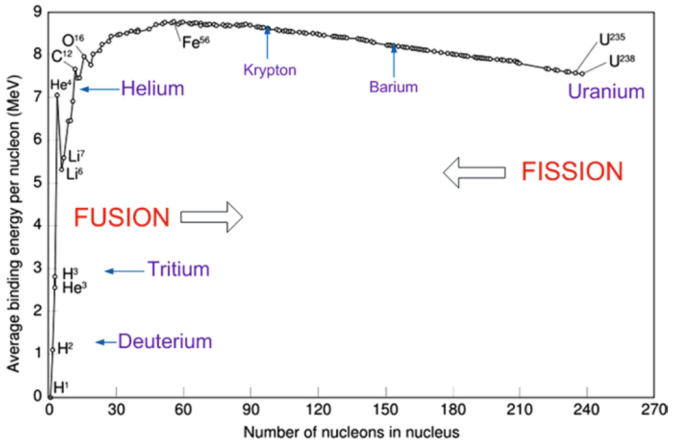

Figure 1.1: Nuclear binding energy dependence on the atomic number for common isotopes. Taken from Chen (2011).

The main technological difficulty of a nuclear fission power plant is to control the amount of fission activity. Since fission of U^{235} occurs under atmospheric pressures and temperatures, it is easily sustained and leads to nuclear chain reactions. A nuclear meltdown, where these chain reactions cannot be sufficiently moderated, can cause disasters such as the one in Chernobyl in 1986. In a meltdown, highly radioactive material can leak into the atmosphere or the groundwater, and can contaminate wide areas, making them uninhabitable for a long time. While the much improved safety of modern fission power plants makes similar disasters highly unlikely, a major remaining problem is the disposal of long-lived radioactive waste. Some of the fission products remain highly radioactive for as long as a million years.

Controlled nuclear fusion is currently in the experimental phase, and several technological questions regarding the design and maintenance of power plants are still open. However, the main difficulty in controlling the energy generation at the heart of a fusion reactor is quite the opposite to a fission reactor. Extreme temperatures are needed for fusion reactions to occur, which makes it very challenging to sustain them in significant amounts (Freidberg, 2007). A failure in the reactor would simply stop nearly all fusion activity, and no nuclear chain reactions have to be moderated, even though off-normal events can significantly damage the reactor vessel itself.

The major advantage of nuclear fusion is the lack of long-lived radioactive waste, that would require safe storage for thousands of years, as in the case of nuclear fission. None of the fusion fuels or fusion products have high levels of radioactivity.

[1] One electronvolt (eV) is equivalent to the energy gained by an electron travelling along a potential difference of 1 V.

The only involved radioactive isotope is tritium (H^3 or T), which emits low energy β-radiation, that is unable to penetrate even the outer dead skin layer of humans. Nonetheless, safety measures have to be implemented to avoid larger leaks of tritium into groundwater, since related health risks have not been ruled out. A more serious challenge regarding radioactivity is posed by the reactor wall components. The energy from nuclear fusion is mostly captured as the highly energetic neutrons, released by the fusion reactions, deposit their energy in an absorbing "blanket" material. It is an ongoing effort to choose the best materials to both increase efficiency and decrease the amount of activated waste. Especially, structural steel around the reactor vessel can be activated to high levels of radioactivity, which means it has to be safely extracted and replaced during maintenance. However, the short half lives of those activated steels requires storage of only around 100 years (Freidberg, 2007).

Nuclear fusion also has the additional advantage of abundant fuel material. Though there is some theoretical flexibility in the choice of fuel for nuclear fusion, the most promising candidates are deuterium and tritium (Chen, 2011). While deuterium is naturally abundant in water, with 0.015 % of hydrogen atoms in water being deuterium, tritium has a half-life of 12 years and is thus not naturally occurring on earth (Freidberg, 2007). However, tritium can be obtained by splitting, for example, lithium (Li^6) by a neutron into helium (He^4) and tritium (H^3). In the context of fusion, lithium is abundant on earth, and thus a shortage of fuel is not foreseen.

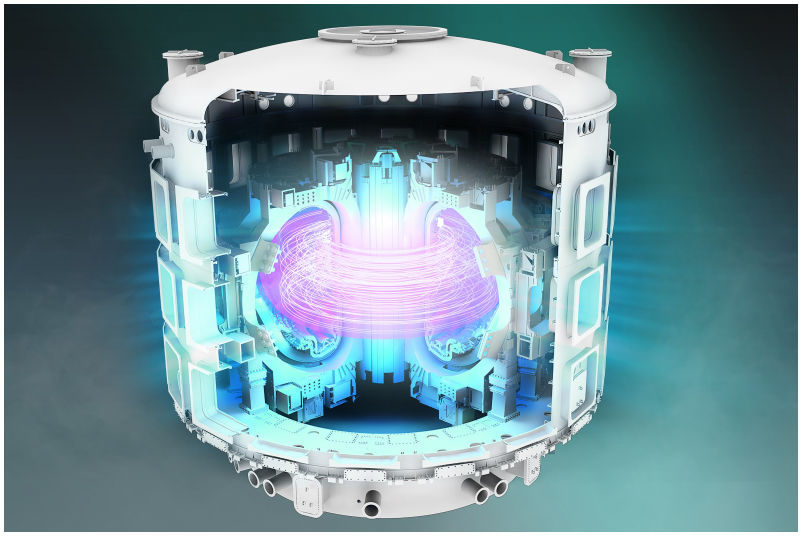

Figure 1.2: Illustration of the ITER tokamak, currently under construction in France. Shown is the cryostat with a diameter and height of around 30 m containing superconducting magnetic coils, which surround the vacuum vessel filled with the fusion plasma. Credit ©ITER Organization, `https://www.iter.org/`.

Many ideas on controlled nuclear fusion have been put forward in over 70 years of research. The most promising concept so far is magnetic confinement fusion (MCF). At the temperatures of around 100 million degrees kelvin needed for nuclear fusion to occur, any material is in a plasma state. In a plasma, the thermal kinetic energy is large enough to ionize most of the plasma particles, i.e. separate the electrons from the atomic nuclei. Therefore, particles in a plasma are electrically charged and

interact strongly with electromagnetic fields. This is used in MCF to compress the fusion fuel and isolate it. Any interaction with outside material would cool down the fusion fuel rapidly. The physical principles of MCF, in particular that of the tokamak design, are detailed in chapter 2. For now, it suffices to think of MCF as levitating extremely hot plasma, with a density much lower than air, in a large toroidal (donut-shaped) vacuum chamber, as illustrated in fig. 1.2 for the case of the ITER tokamak. The magnetic field is mainly pointing in the toroidal direction and is strongest close to the centre. An additional twisting of the field lines is generated by a toroidal plasma current externally induced by a strong electric field. ITER is the next step MCF device, currently being built in the south of France. It is expected to be one of the first MCF devices to achieve a net energy gain and to demonstrate the feasibility of a nuclear fusion power plant. DT plasma operation in ITER is scheduled for 2035.

1.2 Pellet injection for fuelling and controlling fusion plasmas

Once the fusion plasma is magnetically confined and heated, it has to be sustained. Not only is the fusion fuel gradually being used up, but instabilities in the plasma necessitate control of the temperature and density profile inside the torus. In the case of large-scale instabilities, the plasma confinement is lost, and the fusion extinguishes in a thermal quench. This thermal quench is often followed by a current quench, where the external electric field may accelerate electrons in the plasma to relativistic energies, forming a beam of so-called runaway electrons. Consequently, most of the energy stored in the fusion plasma quickly leaves the confinement region, which can damage or potentially destroy the reactor walls and components. These violent events are called disruptions and have to be mitigated efficiently (Hender et al., 2007; Hollmann et al., 2015).

The injection of cold, dense material into the plasma can both help sustain the plasma in the case of additional fuel material or reduce the risk of damage during disruptions, mainly in the case of impurities (Hollmann et al., 2015). While it was thought initially to be easiest to pump this material in as a gas, it was realized that gas cannot easily penetrate the plasma, since it is heated up too quickly at the plasma edge and most of the material is repelled. Instead, the state-of-the-art approach for injecting material into a fusion plasma is to shoot it in as solid cryogenic pellets at high velocities. Both the fuel and noble gas impurities are in a gaseous form under atmospheric conditions. Therefore, the material has to be cooled to only a few degrees kelvin and must be compressed to high densities to become a solid pellet. The low densities found in the fusion plasma enable even tiny pellets of millimetre scale to have large effects (Pégourié, 2007).

The extreme heat flux from the fusion plasma on these frozen pellets causes them to disintegrate in only a few milliseconds. Depending on the size of the pellet and the injection speed, this might be fast enough to stop it from reaching the core of the MCF device.

Once the material of the pellet is ionized, it begins to spread around the fusion plasma. However, this homogenization is not fully symmetric, as the still cold but ionized material mostly drifts outwards. This material outflow is instrumental in setting limits on how much of the material of the pellet is deposited in the plasma and how much is lost to the reactor walls as prompt mass loss (Panadero et al., 2023; Samulyak, 2023). If the pellet is injected from the outside of the torus, i.e. the low-field side (LFS), fuelling the plasma core is only possible if the pellet penetrates deep into the plasma. This favours injection from the inside of the torus, i.e. the high-field side (HFS). However, due to the limited space for reactor components, HFS pellet injection is technologically challenging and might not be possible in many MCF devices, especially in the use case of disruption mitigation.

The material deposition profile depends highly on the pellet's trajectory through the plasma and the rate of ablation, i.e. how quickly the outer shells of the material are sublimated and removed. Therefore, the planning and execution of pellet injection procedures in fusion plasmas requires efficient and accurate models that predict these dynamics. The physics around pellet injection, which is important for this thesis, is explained in chapter 3.

The ablation rate of pellets in MCF has been studied extensively, and many models exist which predict this rate in good agreement with past and current MCF experiments. Widely used for its low computational complexity is a semi-analytical model called the neutral gas shielding (NGS) model by Parks and Turnbull (1978). The ablated material is assumed to form a dense cloud of neutrally charged gas around the pellet, which strongly shields the pellet from the heat flux of incoming plasma electrons (and ions). While this model is one of the earliest models and contains many approximations, more sophisticated models do not yield significantly higher accuracy (Pégourié, 2007). For example, it was found that the pellet is further shielded by the ionized part of the ablation cloud, which surrounds the neutral gas cloud. Including this ionized ablation cloud (or plasmoid) in theoretical models did not significantly change the predictions of the ablation rate. However, it is important in the context of this thesis. The ablation dynamics are further detailed qualitatively in section 3.1 and the NGS model is explained in detail in section 4.2.

1.3 The pellet rocket effect

The trajectory of pellets in MCF has been studied less extensively. Initially, it was assumed that pellets in MCF devices travel along a straight line at constant velocity, since the pellet is neutrally charged and injected at very high speeds. However, experimental observations, as shown in fig. 1.3, strongly suggest that pellets injected into MCF devices are both deflected and slowed down significantly, which could affect the fuelling efficiency and deposition profile. While the exact physics behind this pellet acceleration (or deceleration) is not fully understood yet, it is commonly attributed to a phenomenon called the *pellet rocket effect*, which is the main subject of this thesis.

A rocket generates thrust by expelling mass at high velocity in one direction. Mo-

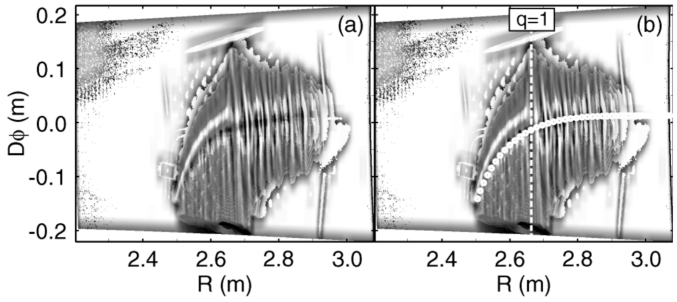

Figure 1.3: Experimental observation of a pellet deflected in the toroidal direction ($D\phi$) in the Tore Supra tokamak. Shown is the time-integrated ablation pattern as measured from the H_α emission of the ablated material. The estimated pellet trajectory is indicated in the right image. Taken from Waller et al. (2003).

mentum conservation dictates that the momentum (mass times velocity) carried by this material must be compensated by an equal but opposite momentum gain by the rocket. The same principle is believed to accelerate pellets in MCF[2]. An asymmetry in the heat source around the pellet leads to an enhanced ablation on the more strongly heated side. The ablated material is continuously heated, which generates pressure in the neutral ablation cloud. The resulting pressure asymmetry pushes the pellet towards the less strongly heated side and accelerates the ablated material the other way. Equivalent pressure dynamics are found in a rocket engine nozzle. The physics behind pellet trajectories and pellet acceleration is detailed further in section 3.2.

Previously, two models have been developed to predict the pellet rocket acceleration. Senichenkov et al. (2007) assumed the ablation cloud to be homogeneous and attributed the acceleration purely to an enhanced ablation rate on one side of the pellet. Szepesi et al. (2007) proposed a semi-empirical model based on the NGS model, in which the pressure asymmetry is the driving factor of the acceleration but must be given as a model parameter. These models are not widely used. Therefore, we attempt with this thesis to develop a semi-analytical model by building on those previous ideas on the pellet rocket effect. The basis of our model is the NGS model to describe the spherically symmetric ablation dynamics of a pellet from first principles. The asymmetric ablation dynamics are then modelled as a perturbation on top of the NGS model. The scope of the thesis limits our attention to the case of hydrogenic pellets. While our model presumably works for any MCF device and any direction of acceleration, it is applied here only to the case of radial pellet acceleration in tokamaks during LFS injection. The model derivation is detailed in sections 4.1 to 4.3. The results are then compared to recent 3D Lagrangian particle simulation studies on the same pellet acceleration effect by Samulyak (2023) in section 4.4.

The final part of this thesis, chapter 5, discusses the limitations of our model and the impact this may have on the presented results. An outlook is given for possible future modelling efforts on the pellet rocket effect.

[2]Even other solid material in a tokamak like metallic dust experiences this rocket acceleration (Lazzaro et al., 2020).

2

Plasma physics and magnetic confinement fusion (MCF)

For nuclear fusion to occur, the kinetic energy of two colliding nuclei must allow them to overcome their mutual electrostatic repulsion and get sufficiently close that the attractive nuclear force can dominate. Quantum mechanical tunnelling effects allow nuclei to fuse at energies much lower than the full height of the so-called Coulomb potential barrier between them. Even though the sun's core has temperatures of around $15 \times 10^6\,\mathrm{K}$ only a tiny fraction of the protons fuse every second (Chen, 2011). The sun can thus sustain fusion for billions of years, but fusion on earth can only be a viable energy source with a much higher efficiency. The hydrogenic fusion reaction with the highest reactivity at the lowest required temperature is

$$\mathrm{D} + \mathrm{T} \longrightarrow \mathrm{He}^4 + \mathrm{n}\,,$$

which still only reaches significant reactivities above temperatures around $100 \times 10^6\,\mathrm{K}$. This corresponds to particle kinetic energies of around 10 keV. The energy released is 17.6 MeV per fusion reaction, of which around 20 % is given to the helium ion as kinetic energy and the rest is released as kinetic energy of the neutron. The charged, heavy helium ion is usually stopped inside the plasma close to the reaction region and deposits it energy to heat the plasma. The light, uncharged neutron can escape the plasma nearly unaffected, while being highly energetic. Fusion reactors will be built such that the dense material around the fusion plasma is designed to capture the neutron's energy and use the corresponding heat to generate electricity. Since the energy gain per fusion reaction is so high[1], the plasma does not need to contain much fuel and can be 5 orders of magnitude less dense than air. A typical fusion plasma[2] has a particle density of around $10^{20}\,\mathrm{m}^{-3}$ at pressures around 7 atmospheres (Freidberg, 2007).

Material which is hot enough to reach significant fusion activity would be driven to expand quickly. Allowing this expansion to happen would rapidly cool down the plasma and the burning plasma would extinguish. Additionally, the plasma would touch any material it is surrounded by and deposit its energy there. This approach of allowing fusion to happen for a very short time is the basis of inertial confinement fusion (ICF). A different approach is to trap the fusion plasma, which

[1] At significant reactivities.

[2] Only in the case of magnetic confinement fusion.

consists of charged particles, by magnetic fields. Most modern concepts for fusion energy generation are based on this magnetic confinement fusion (MCF) approach, which is the focus of this thesis.

This chapter covers the essential dynamics of a magnetized plasma in section 2.1, leading up to the design of MCF devices, as described in section 2.2. The definition of a plasma is detailed in section 2.1.1, before moving on to the motion of individual particles subjected to magnetic and electric fields in sections 2.1.2 and 2.1.3. The properties of such particle motions are crucial for the design of MCF devices, and are also important for the dynamics of ionized material ablated from a pellet, as described later in section 3.1.2.

2.1 Dynamics of magnetized plasma

Plasma is commonly referred to as the fourth state of matter. Instead of containing nearly exclusively neutrally charged atoms, as in the states of gases, fluids or solids, a significant fraction of the particles in a plasma are ions and electrons, not bound to each other. Generally, the amount of ionization in a plasma can vary, but typical fusion plasmas can be considered fully ionized. Plasma can be defined concisely by the single sentence: "A plasma is a quasineutral gas of charged and neutral particles which exhibits collective behavior" (Chen, 2016, p. 2). To fully understand this sentence, the concepts of *quasineutrality* and *collective behaviour* must be explained.

2.1.1 Definition of plasma

In essence, *quasineutrality* means that even though the plasma contains charged particles, these charges cancel each other over macroscopic distances and the plasma appears as neutrally charged. Consequently, the total number of positive and negative charges in a plasma must be approximately equal. Pondering on this definition, one might confuse it with the concept of neutrality in the other states of matter, since atoms consist of the positively charged protons and the negatively charged electrons. However, the length scale over which a plasma is considered neutral is much larger than the size of atomic orbits, while being much smaller than the length scale L of the plasma itself. This is quantified by the so-called Debye length

$$\lambda_\mathrm{D} \approx \sqrt{\frac{\varepsilon_0 T_e}{n_e e^2}} \ll L\,, \tag{2.1}$$

which determines the length scale over which the electrostatic potential decreases exponentially around the plasma particles[3] (Chen, 2016). The physical constants ε_0 and e are the vacuum permittivity and the elementary charge, respectively. The plasma parameters are the electron temperature[4] T_e and the electron density n_e. In MCF, the Debye length is typically on the order of 0.1 mm.

[3]This formula is only valid in the case of one singly charged ion species.

[4]Note that in plasma physics, and in this thesis, temperature is by convention given in units of energy (typically eV) by including a factor of the Boltzmann constant k_B in the definition.

A plasma contains many particles inside the radius of one Debye length, i.e.

$$N_{\mathrm{D}} \approx \frac{4}{3}\pi\lambda_{\mathrm{D}}^3 n_e \gg 1\,, \tag{2.2}$$

where N_{D} is the number of particles inside a Debye sphere (Chen, 2016). Individual particles interact with one another electromagnetically within the Debye sphere, without forming bound structures like atoms. Beyond the Debye length, particles no longer see the individual charges of other particles, and the plasma instead shows *collective behaviour*. For a plasma to display such a behaviour, electromagnetic interactions must dominate over collisions with neutrals. This sets an additional constraint on the density of neutral particles in the plasma.

2.1.2 Charged particle in a magnetic field

Despite the quasineutrality of a plasma, external electric and magnetic fields applied to a plasma affect the dynamics drastically due to the collective behaviour of the charged particles. The exact response of a plasma to external electric and magnetic fields is extremely complex. Thus, it is useful to initially consider how an individual particle of charge q moves due to the electromagnetic force

$$\vec{F} = q\left(\vec{E} + \vec{v} \times \vec{B}\right)\,, \tag{2.3}$$

where $\vec{v}$ is the particle velocity and $\vec{E}$ and $\vec{B}$ are the electric and magnetic fields respectively.

In a homogenous magnetic field, without an electric field, the particle can move freely along the magnetic field. In the plane perpendicular to $\vec{B}$, the particle must undergo a circular orbit, since the force is also perpendicular to $\vec{v}$ and constant. This movement is called gyration and has the gyro frequency[5] and gyro radius[6],

$$\omega_{\mathrm{c}} = \frac{qB}{m} \qquad \text{and} \tag{2.4}$$

$$r_{\mathrm{L}} = \frac{v_\perp}{\omega_{\mathrm{c}}}\,, \tag{2.5}$$

with the particle mass m and the particle velocity $v_\perp$ perpendicular to $\vec{B}$. Note that the direction of gyration is opposite for ions and electrons, as illustrated in fig. 2.1a (Freidberg, 2007).

2.1.3 Particle drifts in magnetized plasma

The charged particle motion becomes more complex in a non-uniform electromagnetic field, but the gyration, i.e. spiralling motion around the magnetic field line, generally persists. Thus, it is helpful to describe the motion of the point around which the particle gyrates, the so-called guiding centre.

[5] Also called cyclotron frequency.
[6] Also called Larmor radius.

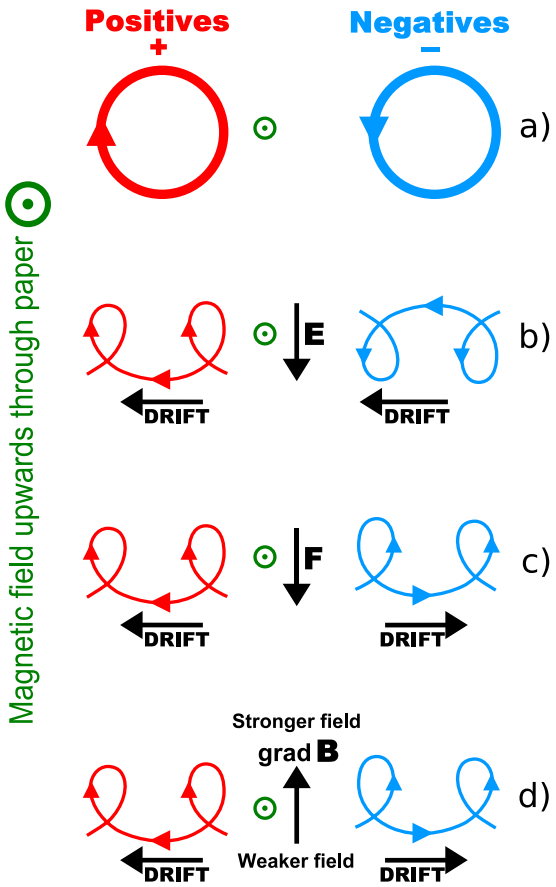

Figure 2.1: Illustration of charged particle drifts. Taken from `https://en.wikipedia.org/wiki/Guiding_center` and edited slightly.

Since the magnetic field only acts on the particle in the perpendicular plane, the motion can be split up into motion along and across magnetic field lines. Any parallel component of a general force $\vec{F}$ on the particle, for example from an electric field $F_\parallel = qE_\parallel$, is unaffected by the magnetic field and accelerates the particle such that $\dot{v} = F_\parallel/m$.

Allowing for general force components perpendicular to the magnetic field, the particle is accelerated on one side of the gyro orbit and decelerated on the other side. This causes the guiding centre to not be accelerated, but to undergo a drift at constant velocity

$$\vec{v}_{\vec{F}\times\vec{B}} = \frac{1}{q}\frac{\vec{F}\times\vec{B}}{B^2} \tag{2.6}$$

which is perpendicular to both $\vec{B}$ and $\vec{F}$, as illustrated in fig. 2.1c. Applying this to the case of an electric field, the charge factor in the force $F_\perp = qE_\perp$ cancels out and particles experience the so-called the $\vec{E}\times\vec{B}$ drift, which is independent of the charge, as shown in fig. 2.1b.

A spatially varying magnetic field strength imposes a force $\vec{F} = \vec{\nabla}(\vec{\mu}\cdot\vec{B})$ on a particle of magnetic moment μ. The charged particles in the plasma gyrate, and their magnetic moment $\mu = mv_\perp^2/2B$ opposes the external magnetic field, making the plasma diamagnetic. Thus, the particles are decelerated in the parallel direction in a region of increasing magnetic field strength, which is the so-called magnetic mirror effect. In the perpendicular plane, the resulting grad$B$ drift

$$v_{\mathrm{grad}B} = \frac{\mu}{q}\frac{\vec{B}\times\vec{\nabla}B}{B^2} \tag{2.7}$$

essentially separates negative from positive charges, as illustrated in fig. 2.1d.

Three additional smaller drifts[7] are related to the particle's inertia. If the magnetic field lines are curved, the particle following this curve experiences an outward centrifugal force. Due to eq. (2.6), this results in a drift, called the curvature drift, pointing in the same direction as the grad$B$ drift and thereby enhancing the charge separation. However, the charge separation is opposed by a drift related to the increase in electric field strength over time coupled to the particle inertia, called

[7] Since these drifts only play a secondary role in this thesis, they are only briefly mentioned.

the polarization drift. Lastly, an effective drift in a plasma due to averaged fluid properties is the so-called diamagnetic drift. This drift is caused by a plasma pressure gradient and is perpendicular to both this pressure gradient and the magnetic field but in opposite directions for ions and electrons (Freidberg, 2007).

2.2 Tokamak design

The net effect of a magnetic field on plasma motion is used to isolate the plasma in a MCF device. Several magnetic field configurations have been proposed and tested over the last 70 years, but two concepts remain the major candidates for MCF, the stellarator and the tokamak. Both designs rely on closing the magnetic field lines into a "loop" so that the charged particles, i.e. the plasma constituents, ideally circle around in the device. However, as detailed further down, the plasma can only be confined if the magnetic field lines are additionally "twisted". The difference in the two concepts is mainly that a stellarator generates the full magnetic field by using external coils, while a tokamak induces a current in the plasma, which twists the magnetic field lines. The scope of this thesis is focused on the tokamak design[8].

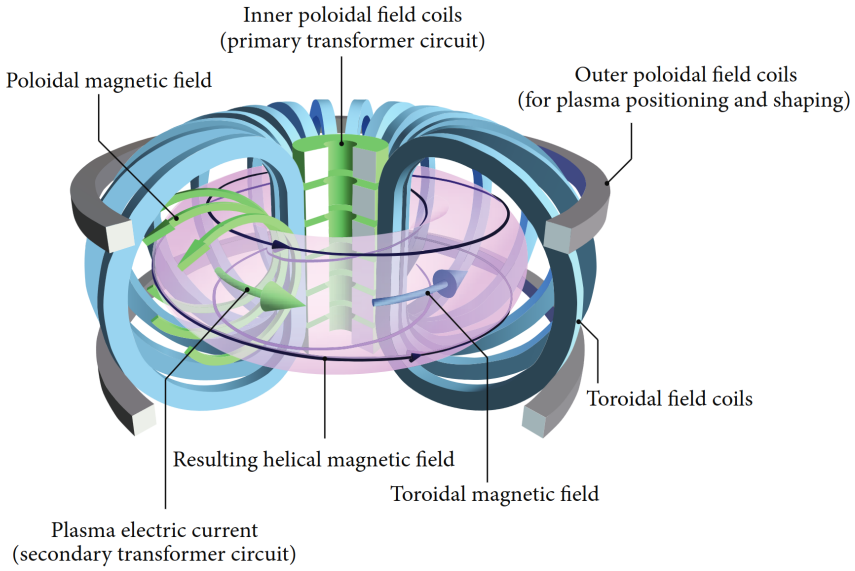

Figure 2.2: Illustration of the magnetic field in a tokamak. Specifically, shown are the poloidal and toroidal fields and the components that generate them. Taken from Li et al. (2014).

In a tokamak, the main magnetic field, which defines the donut-shape of the plasma, is the *toroidal* magnetic field, as illustrated in fig. 2.2 by a blue arrow. It is generated by current flowing through external, D-shaped toroidal field coils. For geometric reasons[9], this magnetic field is stronger on the inner side of the caged plasma (pink in fig. 2.2) than on the outer side. The former is thus called the high-field side (HFS)

[8]Details of the tokamak design such as heating of the plasma, divertors, disruption mitigation and many others are not elaborated on in this thesis.

[9]Apply Ampere's law to a toroidal loop at a given radius within the toroidal field coils.

and the latter is called the low-field side (LFS). That is, to a first approximation, the gradient of the magnetic field points inwards along the major radius of the torus, i.e. of a tokamak, which is measured from the vertical symmetry axis. The minor radius is measured from the toroidal symmetry axis.

It is this gradient along the major radius together with the curvature of the field lines that would lead to a loss of confinement without the "twist" of the field lines. Additionally, the corresponding mechanism also plays an important role in the pellet ablation cloud dynamics, as explained in section 3.1.2. The grad$B$ drift points in opposite vertical directions for the positively charged ions and the negatively charged electrons. The opposing polarization drift, due to the increasing vertical electric field, slightly reduces the extent of this effective vertical charge separation inside the plasma, but a significant electric field is generated. This vertical electric field then causes the plasma particles to drift outwards, i.e. down the magnetic field gradient, due to the $\vec{E} \times \vec{B}$ drift. In a purely toroidal magnetic field, both of these drifts would transport the plasma particles away from the centre of the torus and cause them to exit the confinement region (Freidberg, 2007).

In a tokamak, this problem is avoided by introducing an additional weaker poloidal magnetic field, as illustrated in fig. 2.2 by the green arrows around the plasma. This poloidal field twists the field lines into a helical shape, as shown by the black lines. The plasma particles follow the helical path, circling around the torus. The effect of the dominantly vertical grad$B$ drift is thus cancelled out, as particles spend a roughly equal amount of time on the upper part of the plasma as on the lower part. Overall, the drifts are mitigated and the plasma is magnetically confined.

The poloidal magnetic field in a tokamak is mainly produced by an induced plasma current in the toroidal direction. Since the resistivity of the hot fusion plasma is much lower than in a regular conductor, a comparatively low electric field is sufficient to drive plasma currents of up to tens of MA. This electric field in a tokamak is often induced by a central solenoid, as shown in fig. 2.2 by the inner poloidal field coils. The solenoid current is slowly increased, which generates a changing magnetic field and thus induces an electric current. Since this transformer-like induced current cannot be increased indefinitely, a tokamak is operated in a pulsed procedure. Additionally, outer poloidal field coils help to shape the magnetic field and stabilize the plasma.

The main driving factor of plasma instabilities in a tokamak is the strong toroidal current. When instabilities grow large enough so that the energy confinement is lost, i.e. in a disruption event, the plasma rapidly cools down in a thermal quench. This causes the resistivity in the plasma to rapidly increase. However, the highly inductive plasma tends to then keep the current running by inducing a strong toroidal electric field during the current quench. This strong toroidal electric field can accelerate energetic electrons to significant fractions of the speed of light because, unlike in the other states of matter, above a critical velocity, electrons in a plasma interact less and less with the surrounding plasma particles, which decreases the effective drag force. Those electrons are called runaway electrons and can be seeded from various sources in a disrupting plasma. Mitigating disruptions is one of the major challenges in designing a fusion power plant to limit the risk of serious damage to

the device components. The most advanced method is to control the cooling process and evolution of the current and electric field by the injection of additional cool and dense material, in the form of cryogenic pellets (Hender et al., 2007).

3

Pellet injection

Understanding the dynamics of what happens after a pellet enters the fusion plasma is of utmost importance when developing and operating pellet injection schemes in MCF devices such as tokamaks. The main idea is that the frozen material of the pellet is continuously ablated, i.e. sublimated and removed, while traversing the fusion plasma, thereby depositing fuel or impurities in the plasma. The ablated material will be quickly ionized and homogenizes along the field lines. This not only serves the purpose of replenishing the fuel in the fusion plasma. Pellet injection is also used to control the density profile of the plasma, to control edge localized modes and to mitigate disruptions. Adding density and/or lowering the plasma temperature can greatly influence the plasma dynamics in both the core and the edge (Pégourié, 2007).

In the case of disruption mitigation, large amounts of pellet material have to quickly be deposited in the plasma. However, large pellets cannot disintegrate fast enough and could possibly pass through the plasma and damage the opposite wall. Instead of just shooting in the pellet whole, it can be directed at a target[1], which shatters the pellet into many tiny pellet shards before entering the plasma and thereby maximizes the quick deposition of material in the plasma, starting from the edge. This method is called shattered pellet injection (SPI) and is essential to mitigate disruptions in future fusion reactors (Commaux et al., 2010; Hollmann et al., 2015).

Optimally, a disruption event in a MCF power plant would be detected as early as possible[2] when signals of the instability onset become apparent during the precursor stage. Then, SPI can decrease the negative impact of the disruption in three major ways (Hollmann et al., 2015; Vallhagen, 2023). First, a tokamak is designed so that most of the hot plasma exhaust is directed towards a region of more durable material, called the divertor. However, during a disruption, localized heat fluxes can be too large even for the divertor[3] material and can damage it. Injecting pellets that contain impurities such as neon or argon[4] can dissipate some of the energy homogeneously through emission of radiation in atomic processes. Second, during the current quench of a disruption, the plasma current can leak to the device components and induce

[1] Often a bend in the guiding tube.

[2] Fast detection of disruptions is still a major challenge in tokamaks because of the high neutron flux and the thick metal walls.

[3] Other wall components can also be damaged by the intense radiation or through heat conduction.

[4] Neon and argon are noble gases that emit radiation at the right temperature and do not integrate into the MCF device components.

strong eddy currents or halo currents. Combined with the strong magnetic fields, this can put the structural device components under intense physical stress. The pellet induced cooling of the plasma can be used to tune the plasma resistivity, which then mitigates untolerable stresses. Last, runaway electrons can be mitigated by increasing the density in the plasma, which effectively increases the drag felt by electrons in the plasma.

Theoretical predictions are used to help plan pellet injection schemes, so that the material is efficiently delivered at the right location in the plasma. A first important prediction is the ablation rate, i.e. how fast the pellet[5] loses material to the plasma. The dynamics involved are further explained in section 3.1, with a focus on the inner cloud of neutral gas in section 3.1.1 and a focus on the outer cloud of cold plasma in section 3.1.2. Another important factor is how fast and in what way the cold plasma equilibrates with the hot fusion plasma, which is also briefly touched upon in section 3.1.2. Finally, the full effect of an injected pellet can only be estimated if the pellet trajectory is accurately predicted, which is the topic of section 3.2.

3.1 Ablation dynamics

Immediately after a pellet of frozen material is exposed to the high heat flux in a fusion plasma, the outer layers of the pellet sublimate and form a dense cold cloud around the pellet, as illustrated in fig. 3.1. Close to the pellet, this ablation cloud is a nearly spherical neutral gas and further away the material ionizes and forms an elongated plasma cloud, called the plasmoid. The ablation cloud absorbs or scatters most of the energy of the incident electrons and ions, which effectively shields the pellet from the heat flux. Ions in a fusion plasma have a much lower thermal speed than electrons and are stopped more easily. Thus, electrons are the main heat source reaching the pellet. Overall, pellet ablation dynamics can be seen as a self-regulating process, where the ablation cloud establishes itself to largely shield the pellet from the incoming heat. The ablation rate and shielding capability balance each other so that the cloud has the right density. Since the ablation cloud adapts nearly instantaneously[6] to changes in the pellet and outside plasma conditions, it is sufficient to treat the cloud in a quasi steady state approximation.

In the case of hydrogenic pellets, where the sublimation energy per molecule[7] is low (around 0.01 eV/molecule), the pellet is nearly fully shielded from the incident energy flux from the plasma (Pégourié, 2007). Impurities like neon and argon have comparable sublimation energies (Gebhart et al., 2020). However, impurities like carbon or beryllium have sublimation energies of 1 to 10 eV/atom (Parks et al., 1988), which results in only partial shielding. This thesis is restricted to the case of hydrogenic pellets.

Most of the dynamics explained in this chapter are based on theoretical models

[5] In the following, the word pellet is used to refer to both whole pellets or pellet shards in the case of SPI.

[6] On timescales faster than 1 µs (Parks & Turnbull, 1978).

[7] Frozen hydrogen sublimates as a molecular H_2 gas instead of an atomic H_1 gas.

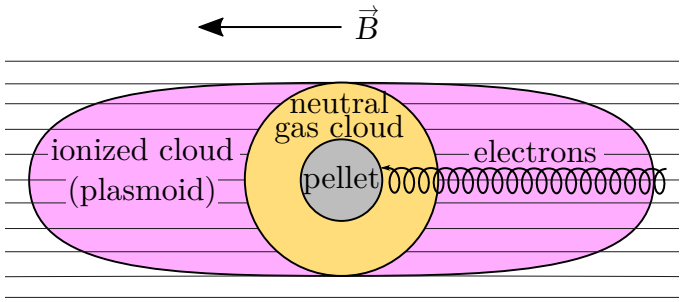

Figure 3.1: Illustration of the ablation cloud that shields an injected pellet. The neutral part of the ablation cloud expands nearly spherically (shown in orange) and once the material is ionized it expands along the field lines (shown in pink). Note that the shown proportions are not to scale. In reality, the plasmoid is much larger than the neutral gas cloud, which in turn is much larger than the pellet and the electron gyration radius is even smaller. Inspired by Baylor (2016).

rather than experimental observations. Time-resolved measurements of pellet ablation dynamics are rare and difficult to perform. Pellets have typical lifetimes of a few ms, speeds of 100 to 1000 m/s and sizes on the mm scale. Nevertheless, measurements of general properties, such as the pellet trajectory, the ablation profile and material deposition profile[8] were able to validate some quantitative predictions of theoretical models (Pégourié, 2007). Thus, the following qualitative description presents the most likely underlying dynamics.

3.1.1 Neutral gas ablation cloud

Directly after leaving the pellet surface, the ablated molecules form a cold neutral gas. Electrons traverse the neutral gas along the field lines and deposit their energy through processes such as absorption, atomic excitation, dissociation and scattering. Because of this continuous heating, the gas expands and is accelerated outwards nearly spherically symmetrically. At the same time, a continuous outflow of particles from the pellet surface supplies the cloud with newly ablated material. Close to the pellet surface, the neutral gas cloud is very dense, with pressures of around a hundred atmospheres, but still much less dense than the pellet itself. Further outwards, the density and pressure quickly drop, while the temperature and flow velocity are continuously increased. Since the pressure of the fusion plasma is still several orders of magnitude lower than in the ablation cloud, back pressure effects from the outside are negligible. Once the flow velocity becomes sonic, i.e. reaches the speed of sound in the gas, the expansion becomes the driving factor for further acceleration to supersonic speeds. This transonic acceleration effect can be seen as similar to the dynamics in a convergent-divergent nozzle, such as those used for rocket propulsion (Parks & Turnbull, 1978).

As they flow away from the pellet, the ablated molecules dissociate into hydrogen atoms, and these atoms eventually ionize. While the material is fully dissociated

[8] Obtained by spectroscopy.

inside the sonic radius, ionization occurs at higher energies and therefore in the supersonic part further outwards. When the ablated material ionizes, the kinetic energy is reduced[9] and the flow velocity rapidly slows down to subsonic speeds. The resulting shock front thus separates the neutral part of the ablation cloud from the nearly fully ionized part (Ishizaki et al., 2003; Pégourié, 2007).

The ablation cloud was first modelled as this transonic phenomenon by Parks and Turnbull (1978). They developed a semi-analytical model for the neutral gas dynamics, commonly referred to as the neutral gas shielding (NGS) model, and provided scaling laws for ablation properties such as the ablation rate. Even though the NGS model contains many strong assumptions, it agrees surprisingly well with experimental measurements of pellet lifetimes and ablation rates (Pégourié, 2007). It is thus still used for ablation rate predictions in pellet injection simulations. The success of the NGS model is the reason it was chosen to be the basis of our model for the pellet rocket effect. The details of the NGS model and how we extend it to include asymmetric dynamics are explained in section 4.2. While Parks and Turnbull (1978) assumed the ionization to play no significant role in the shielding dynamics, we have to account for this effect in our model and the relevant physics is explained qualitatively in the next section.

3.1.2 Plasmoid ablation cloud

Once the ablated material is ionized, it is effectively a magnetized plasma like the fusion plasma around it. However, the density is still very high ($\sim 10^{24}\,\mathrm{particles/m^3}$) compared to the fusion plasma density ($\sim 10^{20}\,\mathrm{particles/m^3}$) and the temperature is only 1 to 4 eV (Matsuyama, 2022; Müller et al., 2002). The external heating and the outflow of particles drives the ionized cloud to further expand. But since the charged particles are confined to the magnetic field lines, expansion perpendicular to the field lines is prevented. Instead, the cold plasma cloud expands along the field lines at its ion sound speed and forms initially a cigar shaped plasmoid.

The plasmoid contributes at least in three separate ways to the shielding of the heat flux (Pégourié, 2007). The most important shielding mechanism is the elastic and inelastic scattering of incoming ions and electrons, similarly to the gas shielding. Furthermore, a slight potential difference arises between the neutral ablation cloud and the plasmoid because the electrons of the fusion plasma penetrate deeper than the ions. This potential difference then repels incoming electrons and shields the pellet electrostatically. Conversely, ions in the plasmoid are slightly attracted towards the pellet, but they deposit their energy already after a short path through the neutral cloud and do not heat the pellet surface. Lastly, the plasmoid is diamagnetic. This means that the magnetic field is slightly expelled from the plasmoid and the field lines are somewhat bent around the pellet. This partially deflects the incoming heat flux and shields the pellet magnetically.

Since the plasmoid is initially localized around the pellet, it does not benefit from the (drift cancelling) poloidal twist of the field lines that is the concept of the tokamak.

[9] Ionization leads to an energy sink in the ablation cloud.

Therefore, the same $\vec{E} \times \vec{B}$ drift, that would affect a fusion plasma in a purely toroidal magnetic field, also leads to a drift of ionized ablation material down the magnetic field gradient, i.e. outwards along the major radius. As illustrated in fig. 3.2, this produces a finite plasmoid shielding length along the field lines hitting the pellet. This phenomenon is important for our model and is further explained and quantified in section 4.3. During the initial phase of the plasmoid expansion, the acceleration of the outward $\vec{E} \times \vec{B}$ drift is determined by the balance of the grad$B$ drift, the curvature drift and the opposing polarization drift. During the later phases, additional effects define the plasmoid motion as it continues to move away from the pellet. These effects include the depletion of the plasmoid charge due to plasma waves and ohmic currents exiting the plasmoid parallel to the field lines. The full dynamics of the drift of the ionized ablation material has been studied by Vallhagen et al. (2023).

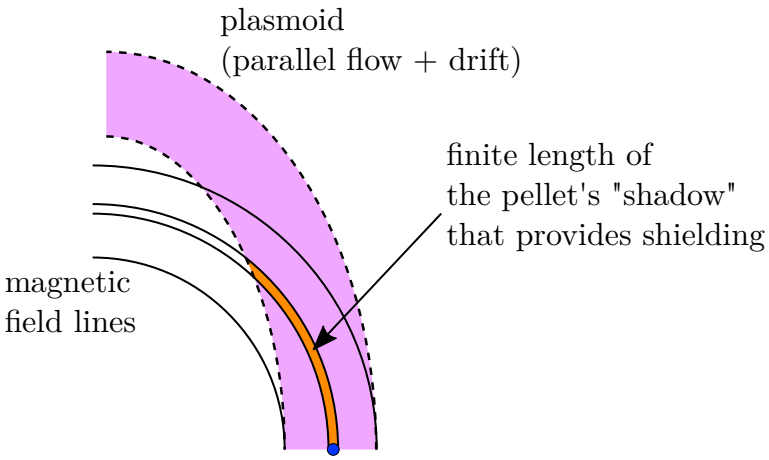

Figure 3.2: Illustration of the $\vec{E} \times \vec{B}$ drift induced plasmoid shielding length along the field lines hitting the pellet. The proportions do not reflect reality. Inspired by Samulyak (2023).

The plasmoid expansion along the field lines continues until the pressure and density have equilibrated with the background plasma. Eventually, the material deposited on one field line almost fully covers the corresponding flux surface due to the poloidal twist of the field lines. This poloidal homogenization process is typically completed in around 1 ms after ablation (Pégourié, 2007). Additionally, the pellet deposits its material on the different magnetic flux surfaces along its trajectory. Thus, the pellet effectively modifies the density profile of the plasma along the minor radius, depending on how fast it disintegrates and if it reaches into the plasma core. However, the outward drift can push some of the deposited material out of the confinement region before it completes one poloidal turn. This material is lost to the device walls, which can severely limit the fuelling efficiency. Since the pellet rocket effect is mainly related to the pellet ablation process and trajectory, which are not significantly affected by the homogenization dynamics, further explanations of these dynamics are outside the scope of this thesis.

3.2 Pellet trajectory

As discussed in the last section, after ablation and ionization, the deposited cold plasma material further drifts outwards. This makes it important that the pellet reaches the plasma core before it is fully disintegrated. The fuelling efficiency is better the deeper the pellet can penetrate the plasma before fully disintegrating (Pégourié, 2007). This consideration is less critical when the pellet is injected from the high-field side (HFS) since then the ablated material drifts towards the plasma core. However, the geometry of a tokamak makes HFS injection challenging because there is little to no space in the centre of the torus. Nevertheless, HFS injection has been performed in tokamak experiments, where the pellet is generated and accelerated outside the LFS, but then guided along a tube towards the HFS (Combs et al., 1998). This type of injection is a much greater engineering challenge. It also restricts the pellet velocity and size, which is especially unfavourable for disruption mitigation, where a large amount of pellet material has to be deposited in the plasma quickly. In most cases, injection from the LFS is preferable. From both the LFS and HFS, pellets have to be injected at the right speeds to reach the plasma core but not shoot through the plasma towards the opposite wall. To find the right injection speed, injection angle and the right pellet size, predictions about the ablation and homogenization dynamics have to be accompanied by predictions of the pellet trajectory based on physical principles.

During the early stages of research on pellet injection technology for MCF, it was believed that the high velocities of around 100 to 1000 m/s would allow the pellet to traverse the plasma in a straight line. The gravitational acceleration on earth of $9.8\,\mathrm{m/s^2}$ is too weak to significantly affect the pellet trajectory. Furthermore, the neutrality of the pellet combined with the low density of the fusion plasma suggested that no other significant forces would act on the pellet.

However, several experimental observations have indicated that the pellet is both deflected and slowed down in the fusion plasma (Pégourié, 2007). One of those experimental results is shown in fig. 1.3, where Waller et al. (2003) measured the ablation profile of a pellet injected into the Tore Supra tokamak. The pellet trajectory could be reconstructed by observation of the H_α emission due to the excitation of the hydrogen atoms ablated from the pellet. A clear deflection of the pellet in the toroidal direction is visible. Radial and toroidal acceleration of the pellet was also observed in the ASDEX Upgrade tokamak by Kocsis et al. (2004) and Müller et al. (2002). A deflection in the vertical direction of the TJ-II stellarator was measured by Medina-Roque (2021).

The observed changes in the pellet trajectory are commonly attributed to the *pellet rocket effect*, resulting from asymmetric heating. For example, in the case of a pellet being deflected in the toroidal direction, it is related to the toroidal plasma current. In the case of acceleration (or deceleration) along the major radius, the asymmetry is induced by the mentioned outwards drift of the plasmoid, creating a shielding length asymmetry across the pellet. The only other plausible explanation for the pellet's acceleration are drag forces between the drifting plasmoid and the neutral ablation cloud (or the pellet directly) (Pégourié, 2007). Polevoi and Shimada (2001)

predicted that this could cause a pellet acceleration 3 to 4 orders of magnitude lower than the plasmoid drift acceleration. Predictions for the pellet rocket effect show this difference to be of around 2 to 3 orders of magnitude (Samulyak, 2023; Vallhagen et al., 2023). Thus, while drag forces could contribute to pellet acceleration, the rocket effect is predicted to be the main mechanism and this thesis does not further consider these viscosity effects.

Two main attempts were previously made, to predict and quantify pellet rocket acceleration. First, a model developed by Senichenkov et al. (2007) associates an enhanced ablation on one side of the pellet with the shielding asymmetry due to the plasmoid drift. The model is based on the ablation model presented by Rozhansky and Senichenkov (2005), which provides analytical scaling laws from first principles, including also the plasmoid physics, but which is not used as much as the NGS model. The plasmoid drift is considered in a simplified way, and the spatial dependence of the ablation cloud properties are mostly neglected. These effects are, however, essential to model in more detail. Second, a semi-empirical model developed by Szepesi et al. (2007) associates the rocket acceleration to a difference in pressure on both sides of the pellet. Although the isotropic pressure is taken from the NGS model, the asymmetry factor is a model parameter, that has to be calculated from experimental observations of pellet trajectories or from simulation results. Recently, Samulyak (2023) presented predictions for the pellet rocket acceleration based on pressure asymmetries calculated in a Lagrangian particle simulation, which included the plasmoid drift and plasmoid shielding dynamics. The developed models are not widely used, and this thesis develops the concepts further into a new semi-analytical model for the pellet rocket effect.

4

Modelling the pellet rocket effect

The underlying principle of the pellet rocket effect is that any asymmetric heating of the pellet and the ablation cloud will lead to a higher ablation and pressure on one side of the pellet. This results in a rocket-like force on the pellet, which accelerates it towards the less heated side. In general, this phenomenon involves complex, three-dimensional, non-linear dynamics. Fortunately, in the case of pellet injection in magnetic confinement fusion, the pellet heating can be seen as predominantly spherically symmetric. Taking the anisotropic pellet ablation dynamics as a linear perturbation on top of the isotropic dynamics enables us to develop a semi-analytical model for the pellet rocket effect.

Conceptually, the model we use is divided into three different parts. The first part, as described in section 4.1, considers the momentum transfer to the pellet surface to calculate the net force on the pellet. Expanding the angular dependence of the gas properties at the pellet surface in spherical harmonics yields a formula for the pellet rocket force, involving only the first order mode ($\cos\theta$-dependence) of the ablation rate and pressure at the pellet surface.

The second part of the model, as described in section 4.2, quantifies the shielding of the pellet from an external asymmetric heating source by the neutral gas ablation cloud. The NGS model, originally developed by Parks and Turnbull (1978), is widely used for predicting isotropic pellet ablation dynamics. Quasi-steady state fluid equations for an ideal gas are solved under two major approximations. First, the external source of heat is assumed as a mono-energetic beam of incoming electrons. Second, all ablation cloud dynamics are simplified to a spherically symmetric geometry. This model is in good agreement with experimental data and while several more sophisticated models were developed, most models yield similar results (Pégourié, 2007). Therefore, the NGS model is used as the basis of our model and is referred to in the following as the *isotropic NGS model*. The asymmetric ablation dynamics are then added as a perturbation in our model, which we refer to as the *asymmetric NGS model*. Since the full radial solution of the isotropic NGS model is needed to calculate the asymmetric dynamics, the isotropic NGS model is described in detail in section 4.2.1. The asymmetric perturbation dynamics are then modelled as described in section 4.2.3, given the external heating source parameters. The most important prediction of this model for the pellet rocket effect is the quantified pressure asymmetry at the pellet surface.

While the asymmetric NGS model can be used by itself, if the heat source into

the neutral ablation cloud is known, our goal is to provide predictions of the pellet rocket acceleration along the major radius of a tokamak for given background plasma parameters. Therefore, the third part of our model, as described in section 4.3, determines the heat source asymmetry induced by the outward drift of the plasmoid of ablated material. How this drift results in a finite and varying shielding length of the electrons through the plasmoid is described in section 4.3.1. In section 4.3.2, the shielding length is used to estimate the heat source at the boundary of the neutral gas cloud.

Finally, in section 4.4, all three parts of our model are combined to make predictions for specific pellet injection parameters in the tokamaks ASDEX Upgrade and ITER. Those predictions are then compared to previous simulation results presented by Samulyak (2023).

4.1 Force on the pellet surface

Consider a spherical pellet of radius r_p surrounded by a neutral gas. Physically, the force on the pellet arises from the combination of ablated particles leaving the pellet surface and the gas pressure pushing on the pellet surface. In the following, a formula for this force is derived under the assumption that the anisotropic dynamics are small compared to the spherically symmetric dynamics.

Mathematically, the momentum transfer at a point $\vec{r}$ in the gas is expressed through the momentum flux tensor

$$\vec{\vec{\Pi}} = \rho \vec{v}\vec{v} + p\vec{\vec{\mathbb{1}}} \,,$$

with the mass density $\rho(\vec{r})$, the fluid velocity $\vec{v}(\vec{r})$ and the pressure $p(\vec{r})$. The notation $\vec{v}\vec{v}$ represents the dyadic product[1], and $\vec{\vec{\mathbb{1}}}$ denotes the 3-dimensional identity tensor. Assuming local momentum conservation at the pellet surface S, the net force on the pellet is

$$\vec{F} = -\iint_S \vec{\vec{\Pi}} \cdot \mathrm{d}\vec{S} \,,$$

where the minus sign indicates that this is the force exerted on the pellet, while the surface element $\mathrm{d}\vec{S}$ points outwards. We choose spherical coordinates $\{r, \theta, \varphi\}$ so that the pellet is centred at the origin and a positive force F points in the negative $\hat{z}$-direction, as shown in fig. 4.1. The force then becomes

$$F = -\hat{z} \cdot \vec{F} = r_\mathrm{p}^2 \iint_S \left[\rho \left(\hat{z} \cdot \vec{v}\vec{v} \cdot \hat{r}\right) + p \left(\hat{z} \cdot \hat{r}\right)\right] \mathrm{d}\Omega \,,$$

with the differential solid angle $\mathrm{d}\Omega = \sin\theta \, \mathrm{d}\theta \, \mathrm{d}\varphi$. Expressing $\vec{v} = v_r \hat{r} + v_\theta \hat{\theta} + v_\varphi \hat{\varphi}$ and using geometric relations between the unit vectors leads to

$$F = r_\mathrm{p}^2 \iint_S \left[\rho v_r (v_r \cos\theta + v_\theta \sin\theta) + p \cos\theta\right] \mathrm{d}\Omega \,.$$

At this point, the first and only approximation for deriving the force formula has to be made. The anisotropic dynamics are taken as a small perturbation on the

[1] Equivalent to a tensor product.

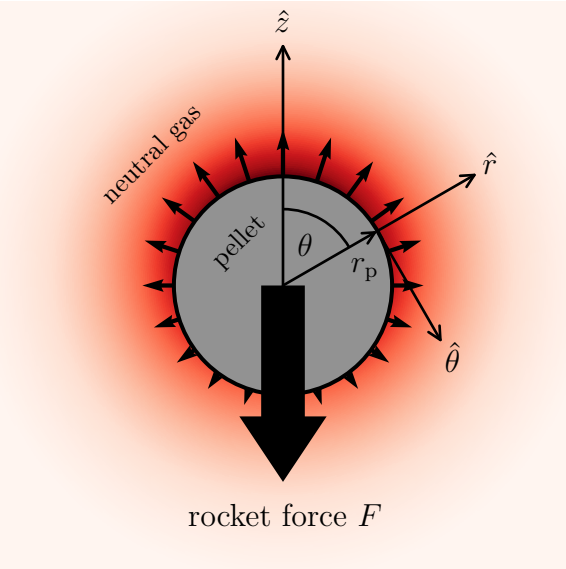

Figure 4.1: Illustration of how the pellet rocket force arises from both an asymmetry in pressure on the pellet surface (visualized by the red background) and an asymmetric ablation (visualized by the vectors). Additionally, the coordinate system used throughout this thesis is indicated. The unit vector $\hat{z}$ denotes the axis of asymmetry. $\hat{r}$ and $\hat{\theta}$ denote the spherical coordinates, in which $\hat{\varphi}$ would point into the paper. The pellet is modelled as a solid sphere of radius r_p.

spherically symmetric dynamics in the form

$$\begin{aligned} v_r(\vec{r}) &= v_0(r) + \delta v_r\,(r,\theta,\varphi), & v_\theta(\vec{r}) &= 0 + \delta v_\theta\,(r,\theta,\varphi), \\ \rho(\vec{r}) &= \rho_0(r) + \delta\rho\,(r,\theta,\varphi), & p(\vec{r}) &= p_0(r) + \delta p\,(r,\theta,\varphi)\,. \end{aligned}$$

Linearizing the force in this perturbation and using $\int_0^\pi \cos\theta\,\mathrm{d}\theta = 0$ leads to

$$F = r_\mathrm{p}^2 \int_{\theta=0}^{\pi}\int_{\varphi=0}^{2\pi} \Big(\big(\delta\rho\, v_0^2 + 2\rho_0 v_0\,\delta v_r + \delta p\big)\cos\theta + \rho_0 v_0\,\delta v_\theta \sin\theta\Big)\,\sin\theta\,\mathrm{d}\theta\,\mathrm{d}\varphi\ . \quad (4.1)$$

The last term can be rewritten as a term proportional to $\cos\theta$ through integration by parts

$$\int_0^\pi \delta v_\theta \sin^2\theta\,\mathrm{d}\theta = \underbrace{\Big[\Big(\int \delta v_\theta\,\mathrm{d}\theta\Big)\sin^2\theta\Big]_0^\pi}_{=0} - \int_0^\pi \Big(\int \delta v_\theta\,\mathrm{d}\theta\Big)\,2\cos\theta\sin\theta\,\mathrm{d}\theta\ ,$$

assuming that $(\int \delta v_\theta\,\mathrm{d}\theta)$ is finite. The surface integral can then be solved by expanding $\delta\rho$, δv_r, δp and $(\int \delta v_\theta\,\mathrm{d}\theta)$ in terms of spherical harmonics

$$Y_l^m(\theta,\varphi) = \sqrt{\frac{(l-m)!}{(l+m)!}}\mathcal{P}_l^m(\cos\theta)e^{im\varphi}\,,$$

with the associated Legendre polynomials $\mathcal{P}_l^m$. Spherical harmonics are orthogonal in the sense

$$\int_{\theta=0}^{\pi}\int_{\varphi=0}^{2\pi} Y_l^m (Y_{l'}^{m'})^*\sin\theta\,\mathrm{d}\theta\,\mathrm{d}\varphi = \begin{cases} \frac{4\pi}{2l+1} & \text{for } l=l'\,,\ m=m' \\ 0 & \text{otherwise} \end{cases}\,,$$

which is helpful because $Y_1^0 = \cos\theta$ appears in front of every term in the surface integral eq. (4.1). Therefore, for any general variations $\delta\rho$, δv_r, δp and $\int \delta v_\theta \, \mathrm{d}\theta$, only their projection onto $\cos\theta$, i.e. the coefficient of the $l = 1$, $m = 0$ mode, contributes to the force. Note that for δv_θ the projection onto $-\sin\theta$ is relevant, since only the integral $\int \delta v_\theta \, \mathrm{d}\theta$ is expanded in terms of spherical harmonics. Inserting the relevant expansions

$$\begin{aligned} \delta\rho\,(r,\theta,\varphi) &= \rho_1(r)\cos\theta + \dots\,, & \delta p\,(r,\theta,\varphi) &= p_1(r)\cos\theta + \dots\,, \\ \delta v_r\,(r,\theta,\varphi) &= v_{1,r}(r)\cos\theta + \dots\,, & \delta v_\theta\,(r,\theta,\varphi) &= -v_{1,\theta}(r)\sin\theta + \dots \end{aligned}$$

into eq. (4.1) yields the formula for the pellet rocket force

$$\boxed{F = \frac{4\pi r_\mathrm{p}^2}{3}\left(\rho_1 v_0^2 + 2\rho_0 v_0 (v_{1,r} - v_{1,\theta}) + p_1\right)_{r=r_\mathrm{p}}}. \tag{4.2}$$

This formula can also be understood physically. The ablation rate per unit area g, i.e. the mass flux through the pellet surface, is

$$g(\theta) = \rho\vec{v}\cdot\hat{r} \approx \left(\rho_0 v_0 + (\rho_1 v_0 + \rho_0 v_{1,r})\cos\theta + \dots\right)_{r=r_\mathrm{p}} = g_0 + g_1\cos\theta + \dots\,.$$

Therefore, the first two terms in eq. (4.2) describe the force arising from asymmetric ablation. The term $\rho_0 v_0 v_{1,\theta}$ describes a force from mass flowing around the pellet surface, and the last term p_1 describes the gas pressure asymmetry. All of this is integrated over the pellet surface area $4\pi r_\mathrm{p}^2$.

Under the self-regulating shielding assumptions, used in the next parts of this model, the pellet rocket force is predominantly caused by the pressure asymmetry in the neutral gas ablation cloud. Therefore, the pellet rocket force is

$$F = \frac{4\pi r_\mathrm{p}^2}{3} p_1(r_\mathrm{p})\,, \tag{4.3}$$

which is essentially the same formula as used for the empirical model developed by Szepesi et al. (2007). The main challenge of this thesis is to develop a model for the pressure asymmetry at the pellet surface $p_1(r_\mathrm{p})$ given an external heating source. This is the subject of the following sections, by developing the asymmetric NGS model.

4.2 Neutral gas shielding (NGS)

As noted in the introduction to chapter 4, the basis of our model is the isotropic NGS model, developed by Parks and Turnbull (1978). Most of this section is dedicated to describing and reproducing this semi-analytical model. The underlying physics processes related to ablation of hydrogen pellets were described already in section 3.1 and will not be repeated here. The following text describes first the general ideas and approximations of the NGS model, which are used for both the isotropic and the asymmetric model. Then the mathematical details of how solutions are found in

the isotropic case are presented in section 4.2.1. Finally, section 4.2.3 describes the perturbative extension in the form of our asymmetric NGS model.

Since the neutral ablation cloud can be considered a transonic ideal gas, the equation of state is

$$\frac{\rho}{m} = \frac{p}{T} \qquad \text{(ideal gas law)}\,, \tag{4.4}$$

with mass density ρ, pressure p, temperature T (in units of energy) and mass m of one molecule (or atom) in the gas. The full gas dynamics are obtained by considering the steady state conservation laws

$$\vec{\nabla} \cdot (\rho \vec{v}) = 0 \qquad \text{(mass conservation)}\,, \tag{4.5}$$

$$\rho(\vec{v} \cdot \vec{\nabla})\vec{v} = -\vec{\nabla} p \qquad \text{(momentum conservation)}\,, \tag{4.6}$$

$$\vec{\nabla} \cdot \left[\left(\frac{\rho v^2}{2} + \frac{\gamma p}{\gamma - 1} \right) \vec{v} \right] = Q \qquad \text{(energy conservation)}\,, \tag{4.7}$$

also known as Euler equations, with flow velocity $\vec{v}$, external heat source Q and the adiabatic index[2] of the gas γ. In an ideal gas, the adiabatic index is related to the number of degrees of freedom f of the gas particles through $\gamma = 1 + 2/f$, so it can be assumed to be $\gamma = 5/3$ for a monatomic gas, $\gamma = 7/5$ for a diatomic gas and $\gamma = 9/7$ for a linear triatomic gas. In the case of frozen deuterium pellets, the temperature close to the pellet is so low that dissociation can be neglected, and the whole neutral ablation cloud is approximated as a D_2 gas.

The external heat source Q at each point in the gas is subject to the major approximations of the NGS model. Heat conduction in the neutral cloud is neglected, since this occurs only on a much slower timescale than the heating from highly energetic electrons losing energy in the cloud through elastic scattering and inelastic processes (Parks & Turnbull, 1978). While, in reality, the incoming electrons are constrained by the magnetic field to traverse the cloud on straight parallel lines, the NGS model approximates this path with an equivalent radial path, as illustrated in fig. 4.2. Denoting the energy flux of the incoming electrons by $\vec{q}(\vec{r})$, the heat source

$$Q = -\mu \vec{\nabla} \cdot \vec{q} = \mu \frac{\partial q}{\partial x} \approx \mu \frac{\partial q}{\partial r} \tag{4.8}$$

is thus modelled as if the electrons lose their energy radially inwards instead of along the field lines in the direction x. is modelled as if the electrons lose their energy radially inwards instead of along the field lines in the direction x. This approximation is motivated by the fact that the energy flux reaching a spherical shell depends on the integrated density along the electron trajectory, which is geometrically similar for both the radial and the parallel paths (Parks et al., 1977). Considering the success of the isotropic NGS model, this approximation is retained in our model. Only a fraction μ of the electron energy loss goes into heating the gas, while the rest goes mainly into Bremsstrahlung radiation and backscattered electrons. Parks and Turnbull (1978) state that the fraction μ is fairly well modelled to be between 60% and 70%

[2] Also called heat capacity ratio.

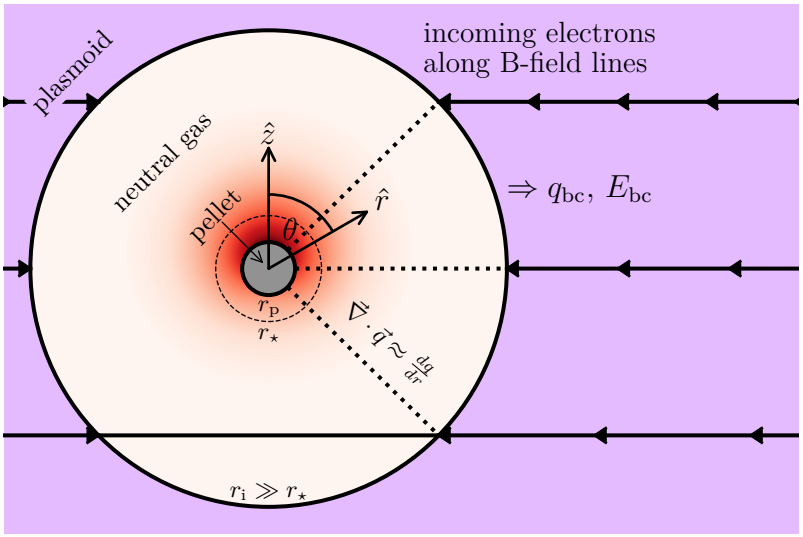

Figure 4.2: Illustration of the asymmetric heating of the neutral gas ablation cloud by incoming electrons travelling along the magnetic field lines. Most of the heating occurs inside the sonic radius $r_\star$, close to the pellet radius r_{p}. The boundary between the neutral ablation cloud and the ionized ablation cloud is comparatively far away at r_{i}. The electrons are modelled to lose their energy radially inwards, while in reality they traverse the neutral ablation cloud on parallel straight lines from two sides.

at all points in the cloud in the case of a hydrogenic gas. Additionally, the incident electrons are approximated to all have the same energy once they reach the point $\vec{r}$ in the neutral ablation cloud. These strong approximations of a mono-energetic beam of incoming electrons losing energy radially have been found to be sufficiently accurate for predicting pellet ablation rates in magnetic confinement fusion. How those approximations degrade the accuracy of predictions of the pellet rocket effect has to be evaluated by comparison to experiments or numerical simulations.

Modelling the exact dynamics of how the electrons lose energy on their path through the gas is a non-trivial task. Therefore, the NGS model uses empirical scaling laws for the scattering cross-sections of electrons in a hydrogen gas. The electron dynamics are thus governed by the differential equations for the energy E and heat flux q

$$\frac{\mathrm{d}E}{\mathrm{d}r} = 2\frac{\rho}{m}L(E) \qquad \text{(electron energy loss)}\,, \tag{4.9}$$

$$\frac{\mathrm{d}q}{\mathrm{d}r} = \frac{q}{\lambda_{\mathrm{mfp}}(E)} = \frac{\rho}{m}q\Lambda(E) \qquad \text{(effective heat flux)}\,, \tag{4.10}$$

where the mean free path λ_{mfp} is modelled through the effective energy flux cross-section $\Lambda(E) = \hat{\sigma}_T(E) + 2L(E)/E$, with the empirical energy loss function

$$L(E > 20\,\mathrm{eV}) = \frac{8.62 \times 10^{-15}\,\mathrm{eV\,cm^2}}{\left(\frac{E/\mathrm{eV}}{100}\right)^{0.823} + \left(\frac{E/\mathrm{eV}}{60}\right)^{-0.125} + \left(\frac{E/\mathrm{eV}}{48}\right)^{-1.94}}\,, \tag{4.11}$$

derived by Miles et al. (1972). The corresponding effective backscattering cross-

section

$$\hat{\sigma}_T(E) = \begin{cases} \left(\dfrac{8.8 \times 10^{-13}}{(E/\mathrm{eV})^{1.71}} - \dfrac{1.62 \times 10^{-12}}{(E/\mathrm{eV})^{1.932}} \right) \mathrm{cm}^2 & \text{for } E > 100\,\mathrm{eV} \\ \left(\dfrac{1.1 \times 10^{-14}}{(E/\mathrm{eV})} \right) \mathrm{cm}^2 & \text{for } E < 100\,\mathrm{eV} \end{cases} \tag{4.12}$$

was derived by Parks et al. (1977) based on experimentally measured values by Maecker et al. (1955). These functions are visualized in fig. 4.3.

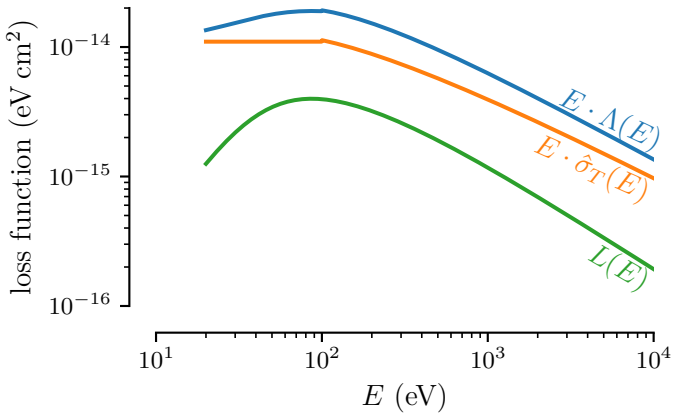

Figure 4.3: Empirical functions $\Lambda(E)$, $L(E)$ and $\hat{\sigma}_T(E)$ used in the NGS model by Parks and Turnbull (1978) for the energy loss of electrons in a hydrogen gas.

The interdependence between the electron heat flux and the ablation cloud density at each point means that the full system of eqs. (4.4) to (4.10) needs to be solved self-consistently. For that, the correct number of boundary conditions have to be motivated that describe the physical system. The low sublimation energy of hydrogen is the reason that the ablation cloud establishes itself to nearly fully shield the pellet. Therefore, the heat flux as well as the gas temperature at the pellet surface can be neglected and taken to be exactly zero. Considering that the back pressure from the fusion plasma and the heat conduction play no significant role in the ablation dynamics, the boundary of the neutral ablation cloud can be seen as infinitely far away ($r_i \to \infty$) from the pellet with negligible pressure. Given the heat flux and average energy of the electrons reaching the neutral ablation cloud, the boundary conditions can be summarized as

$$\begin{gathered} q(r_\mathrm{p}) = 0, \quad T(r_\mathrm{p}) = 0, \\ p(r \to \infty) = 0, \quad q(r \to \infty) = q_\mathrm{bc}, \quad E(r \to \infty) = E_\mathrm{bc}\,. \end{gathered} \tag{4.13}$$

The heating parameters $q_\mathrm{bc}(\theta, \varphi)$ and $E_\mathrm{bc}(\theta, \varphi)$ depend on the plasmoid shielding of the background plasma electrons at temperature T_bg and density n_bg, as modelled further down in section 4.3. Note that no assumptions have to be made on the velocity at which ablated molecules leave the pellet surface, but it is found to be negligible in the numerical solutions under these boundary conditions. However, for our asymmetric NGS model, we have to additionally assume the angular flow velocity at the pellet surface to be zero.

4.2.1 Isotropic NGS model

Consider now the case of full spherical symmetry, where each quantity only depends on the radial coordinate r and the velocity is purely radial ($\vec{v} = v\hat{r}$). Using this symmetry to evaluate and integrate the mass conservation eq. (4.5) leads to

$$4\pi r^2 \frac{\rho}{m} v = const = G\,. \tag{4.14}$$

This radially constant quantity represents the total outflow of particles through any spherical shell and is equal to the particle ablation rate[3] G. Similarly, using eq. (4.14) and the ideal gas law eq. (4.4), the momentum conservation eq. (4.6) and the energy conservation eq. (4.7) become

$$\rho v \frac{\partial v}{\partial r} = -\frac{\partial p}{\partial r} \qquad \text{and} \tag{4.15}$$

$$\frac{G}{4\pi r^2}\frac{\partial}{\partial r}\left(\frac{m}{2}v^2 + \frac{\gamma}{\gamma - 1}T\right) = \mu\frac{\partial q}{\partial r} \tag{4.16}$$

respectively. Together with eqs. (4.9) and (4.10) describing the incident electron dynamics and the boundary conditions in eq. (4.13), the full radial solutions can be determined.

A fully analytical expression for the solution is not tractable, so the equations were prepared for numerical integration. It turns out to be useful to normalize all quantities to their values at the sonic radius $r_\star$, i.e. the radius at which the flow velocity v transitions between subsonic to supersonic speeds, in the form

$$\begin{gathered} \widetilde{\rho} = \frac{\rho}{\rho_\star}, \quad \widetilde{p} = \frac{p}{p_\star}, \quad \widetilde{T} = \frac{T}{T_\star}, \quad \widetilde{v} = \frac{v}{v_\star}, \quad \widetilde{r} = \frac{r}{r_\star} \\ \widetilde{q} = \frac{q}{q_\star}, \quad \widetilde{E} = \frac{E}{E_\star}, \quad \widetilde{\Lambda} = \frac{\Lambda}{\Lambda_\star}, \quad \widetilde{L} = \frac{L}{E_\star \Lambda_\star}, \quad \text{with} \quad \Lambda_\star = \Lambda(E_\star). \end{gathered} \tag{4.17}$$

In this thesis, all quantities denoted with a $\star$ represent their physical values at the sonic radius. Here, variables with a tilde represent their normalized, dimensionless version. However, the tildes will be omitted in the following to prevent visual clutter and all quantities can be considered normalized, if not stated otherwise.

Substituting the physical quantities by the normalized quantities in the ideal gas law eq. (4.4) and the mass conservation eq. (4.14) gives

$$\rho = \frac{p}{T} \quad \text{and} \tag{4.18}$$

$$r^2 \frac{p}{T} v = 1\,. \tag{4.19}$$

The normalized set of differential equations is then obtained after some lengthy but straightforward algebra by additionally using the definition of the speed of sound in an ideal gas

$$v_\star = \sqrt{\frac{\gamma T_\star}{m}}\,. \tag{4.20}$$

[3]Note that Parks and Turnbull (1978) defined G to be the mass ablation rate $G_{\text{Parks}} = m \cdot G$.

The system of eqs. (4.9), (4.10), (4.15) and (4.16) can thus be rewritten in the normalized form

$$\frac{\partial v^2}{\partial r} = \frac{4v^2 T}{(T-v^2)r}\left(\frac{q\Lambda r}{Tv} - 1\right), \tag{4.21}$$

$$\frac{\partial T}{\partial r} = \frac{2\Lambda q}{v} - \frac{1}{2}(\gamma-1)\frac{\partial v^2}{\partial r}, \tag{4.22}$$

$$\frac{\partial E}{\partial r} = 2\lambda_\star \frac{L}{r^2 v}, \tag{4.23}$$

$$\frac{\partial q}{\partial r} = \lambda_\star \frac{q\Lambda}{v r^2}. \tag{4.24}$$

No approximations were made in this derivation and all normalization constants were combined into a single dimensionless quantity

$$\lambda_\star = r_\star \Lambda_\star \frac{p_\star}{T_\star}. \tag{4.25}$$

Since, by design, all normalized quantities (except L) are 1 at the sonic radius $r = 1$, the full radial dependence of $v(r)$, $T(r)$, $E(r)$ and $q(r)$ is determined by providing γ, $\lambda_\star$ and $E_\star$ (implicit in Λ and L). While γ is a material dependent parameter, $\lambda_\star$ and $E_\star$ will be shown to be functions only of E_{bc} for the chosen boundary conditions in eq. (4.13).

Considering $T(1) = v(1) = 1$ introduces an apparent singularity in eq. (4.21) in the form of $1/(T - v^2)$. However, requiring that $\partial v^2/\partial r$ is finite at the sonic radius produces an additional constraint on the normalization constants, found during the derivation of eqs. (4.21) and (4.22) to be

$$\frac{4\pi r_\star^2}{G}\frac{(\gamma-1)}{\gamma}\frac{\lambda_\star \mu q_\star}{T_\star} = 2. \tag{4.26}$$

Using L'Hôpital's rule enables evaluation of the apparent singularity at the sonic radius, yielding

$$\chi_\star := \left.\frac{\partial v^2}{\partial r}\right|_{r=1} = \frac{2}{\gamma+1}\left((3-\gamma) + \sqrt{(3-\gamma)^2 - 2(\lambda_\star + \Psi_\star - 1)(\gamma+1)}\right), \tag{4.27}$$

with an additional shorthand defined as $\Psi_\star := 2\lambda_\star \left(L\frac{\partial \Lambda}{\partial E}\right)_{E=1}$. Now everything is known to start finding numerical solutions for the normalized quantities, which directly determine the physical quantities.

4.2.2 Numerical solution of the isotropic NGS model

The goal of the procedure described below is to find numerical solutions for $v(r)$, $T(r)$, $E(r)$ and $q(r)$, which satisfy both the differential eqs. (4.21) to (4.24) and the boundary conditions in eq. (4.13). For this purpose, for some chosen γ and $E_\star$, we adjust $\lambda_\star$ so that $T(r_p) = 0 = q(r_p)$ at some normalized radius $r_p < 1$, which is then interpreted as the normalized pellet radius. Together with the values $q(\infty)$ and

$E(\infty)$ all normalization constants are determined, and the full physical solution can be calculated. Remember that $E_\star$ denotes the incident electron energy at the sonic radius, which is not known a priori. As a first guess, it suffices to set $E_\star \approx E_{\mathrm{bc}}$, since most of the energy is absorbed only inside the sonic radius.

Many different methods exist to solve a set of first order differential equations numerically. Knowing that

$$v(r=1)=1, \quad T(r=1)=1, \quad E(r=1)=1, \quad q(r=1)=1,$$

any method would work which solves initial value problems. Since the derivatives are determined if all quantities at one radial position are known, the full spatial dependence can be built up iteratively. The method of numerical integration found to work well here is an "implicit multi-step variable-order (1 to 5) method based on a backward differentiation formula for the derivative approximation"[4] based on the implementation by Shampine and Reichelt (1997). The solutions are calculated from $r = 1$ in the directions of both increasing and decreasing r. Optimization of $\lambda_\star$ is done through minimizing the error of the boundary conditions $T(r_p) = q(r_p) = 0$. Here, "a modification of the Powell hybrid method as implemented in MINPACK"[5] is used (Moré et al., 1980).

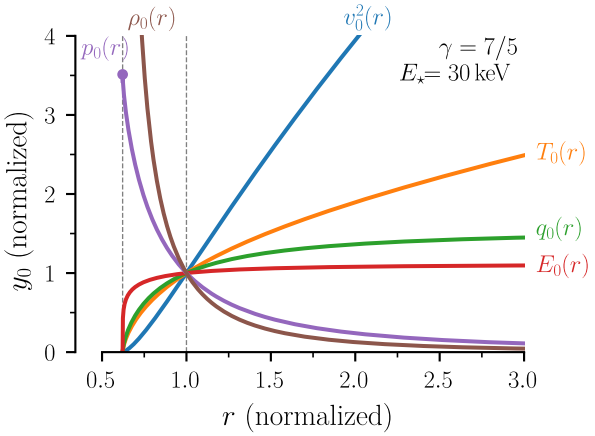

Figure 4.4: Numerical example solution of the normalized isotropic ablation dynamics. Chosen are the parameters $\gamma = 7/5$ and $E_\star = 30\,\mathrm{keV} \approx E_{\mathrm{bc}}$ to have a direct comparison to the solution shown by Parks and Turnbull (1978).

An example solution for $\gamma = 7/5$ and $E_\star = 30\,\mathrm{keV}$ is shown in fig. 4.4, where the subscript 0 denotes the isotropic NGS model quantities as opposed to the asymmetric NGS model quantities with a subscript 1, as introduced in the next section. This same solution is shown by Parks and Turnbull (1978) in their figs. 3 and 4, which serves as a validation of our implemented numerical procedure. Visible is that $E(\infty) = E_{\mathrm{bc}}/E_\star \approx 1$, which justifies $E_\star \approx E_{\mathrm{bc}}$ in this particular case.

To further quantify the energy dependence of the normalized solution, parameter scans over γ and E_{bc} are performed. Figure 4.5 shows the results for $\lambda_\star$, r_{p}, $E(\infty)$

[4] See `https://docs.scipy.org/doc/scipy/reference/generated/scipy.integrate.solve_ivp.html` .
[5] See `https://docs.scipy.org/doc/scipy/reference/generated/scipy.optimize.root.html` .

and $q(\infty)$ after having adjusted $\lambda_\star$ for each parameter combination. Again, we see a match to figs. 1 and 2 of the paper by Parks and Turnbull (1978). Additionally, our results agree well with the scaling laws for $\gamma = 5/3$ (dotted lines) given in the paper. Therefore, these parameter scans serve as another validation of our implementation. It is important to note that in fig. 4.5 the energy dependence is shown on a logarithmic x-axis, while the variation on the y-axis is small and linear. Thus, the dependence on E_{bc} is very weak, and the quantities can be considered nearly constant. The scaling laws representing our solution (dashed lines) are given in appendix A.1.

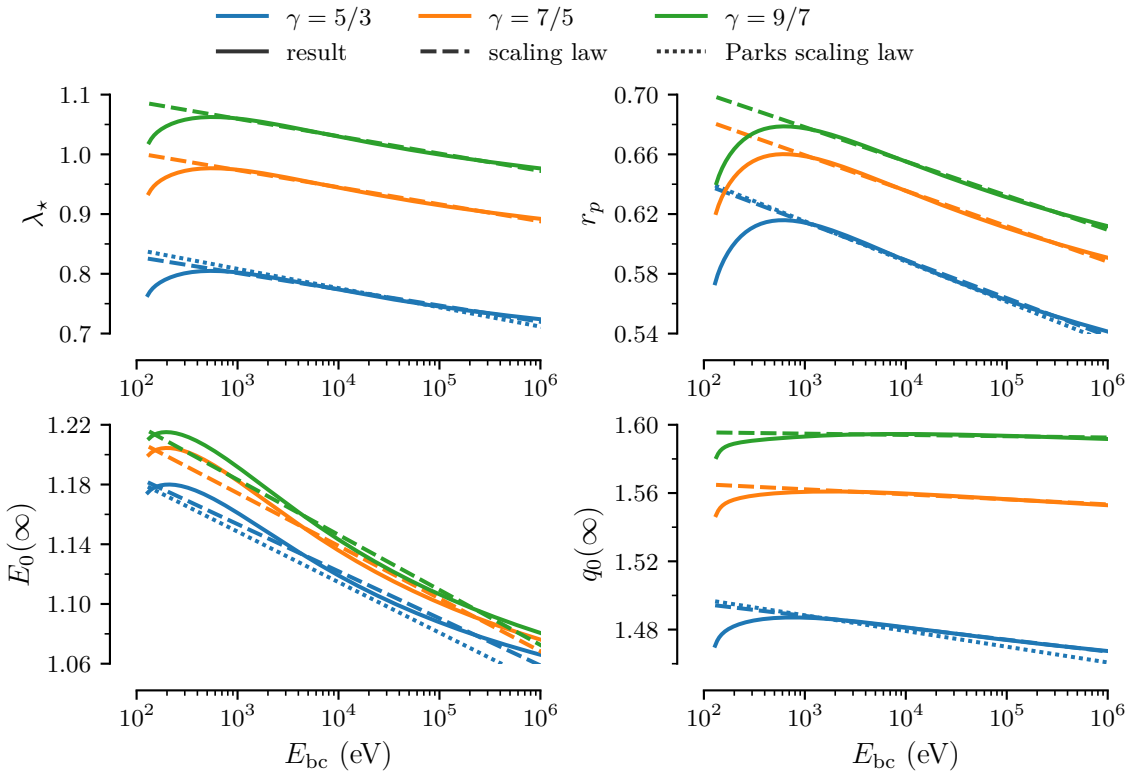

Figure 4.5: Weak dependence on γ and E_{bc} of the normalized isotropic NGS model output. The shown quantities $\lambda_\star$, r_{p}, $E_0(\infty)$ and $q_0(\infty)$ are needed to calculate the physical ablation dynamics.

The solution of the normalized spherically symmetric quantities is all that is needed to model the normalized asymmetric perturbation, as described in the next section about the asymmetric NGS model. However, to calculate any physical quantities, the sonic normalization constants, as defined in eq. (4.17), must be known. Given the physical boundary conditions, i.e. model input parameters, r_{p}, E_{bc} and q_{bc}, the results as presented in fig. 4.5 allow the direct calculation of

$$r_\star = \frac{r_p}{\widetilde{r}_p}, \quad E_\star = \frac{E_{\mathrm{bc}}}{\widetilde{E}(\infty)}, \quad \text{and} \quad q_\star = \frac{q_{\mathrm{bc}}}{\widetilde{q}(\infty)}\,. \tag{4.28}$$

Apart from the sonic density $\rho_\star = m p_\star / T_\star$ (ideal gas law), the remaining unknown normalization constants are $p_\star$, $T_\star$ and $v_\star$. These quantities, together with the

particle ablation rate G, are determined by solving the system of eqs. (4.14), (4.20), (4.25) and (4.26), yielding

$$\boxed{p_\star = \underbrace{\frac{\lambda_\star}{\gamma}\left(\frac{\widetilde{r}_\mathrm{p}(\gamma-1)^2}{4\widetilde{q}^2(\infty)}\right)^{\frac{1}{3}}}_{f_p(E_\mathrm{bc},\gamma)} \cdot \left[\frac{m(\mu q_\mathrm{bc})^2}{\Lambda_\star r_\mathrm{p}}\right]^{\frac{1}{3}}}, \tag{4.29}$$

$$T_\star = \underbrace{\frac{1}{\gamma}\left(\frac{\gamma-1}{2\widetilde{r}_\mathrm{p}\widetilde{q}(\infty)}\right)^{\frac{2}{3}}}_{f_T(E_\mathrm{bc},\gamma)} \cdot \left[\sqrt{m}\Lambda_\star \mu q_\mathrm{bc} r_\mathrm{p}\right]^{\frac{2}{3}}, \tag{4.30}$$

$$v_\star = \underbrace{\left(\frac{\gamma-1}{2\widetilde{r}_\mathrm{p}\widetilde{q}(\infty)}\right)^{\frac{1}{3}}}_{f_v(E_\mathrm{bc},\gamma)} \cdot \left[\frac{\Lambda_\star \mu q_\mathrm{bc} r_\mathrm{p}}{m}\right]^{\frac{1}{3}}, \tag{4.31}$$

$$G = \underbrace{4\pi\lambda_\star\left(\frac{\gamma-1}{2\widetilde{r}_\mathrm{p}^4\widetilde{q}(\infty)}\right)^{\frac{1}{3}}}_{f_G(E_\mathrm{bc},\gamma)} \cdot \left[\frac{\mu q_\mathrm{bc} r_\mathrm{p}^4}{\Lambda_\star^2 m}\right]^{\frac{1}{3}}. \tag{4.32}$$

The physical quantities in the square brackets are the main contributions. The prefactors f_p, f_T, f_v and f_G combine all dimensionless factors and are shown to only weakly depend on E_bc in fig. 4.6. Scaling laws for those prefactors are provided in appendix A.1. Since the pellet rocket effect mainly depends on the pressure asymmetry at the pellet surface, the most important formula here is eq. (4.29), where $f_p \approx 0.15$ and as stated earlier $\mu \approx 0.65$. The importance of $p_\star$ will become clearer towards the end of the next section, in which our approach of modelling asymmetry in the ablation dynamics is detailed.

4.2.3 Asymmetric NGS model

Given the procedure described in the previous sections to calculate the full ablation dynamics under the assumption of spherical symmetry, it is now possible to describe the asymmetry in the ablation dynamics by a perturbative model. The baseline model is the previously described isotropic NGS model, which will be assumed as fully known. It will be denoted from now on with the subscript 0. Assuming the real ablation process is described well by the isotropic NGS model quantities $y_0(r)$ with a small correction $\delta y\,(r,\theta)$, which depends on the asymmetry along one axis (z-axis in fig. 4.2), the full physical quantities can be modelled as

$$\begin{aligned} \rho &= \rho_0 + \delta\rho\,, \quad & p &= p_0 + \delta p\,, \\ T &= T_0 + \delta T\,, \quad & \vec{v} &= \hat{r}(v_0 + \delta v_r) + \hat{\theta}(0 + \delta v_\theta)\,, \\ q &= q_0 + \delta q\,, \quad & E &= E_0 + \delta E\,. \end{aligned} \tag{4.33}$$

The spherical coordinate system is chosen as depicted in figs. 4.1 and 4.2, while any φ-dependence is neglected because it would not contribute to the pellet rocket force.

The system is treated as a quasi-steady state ideal gas, as described at the beginning of section 4.2. Therefore, eqs. (4.4) to (4.10) form the basis of our asymmetric

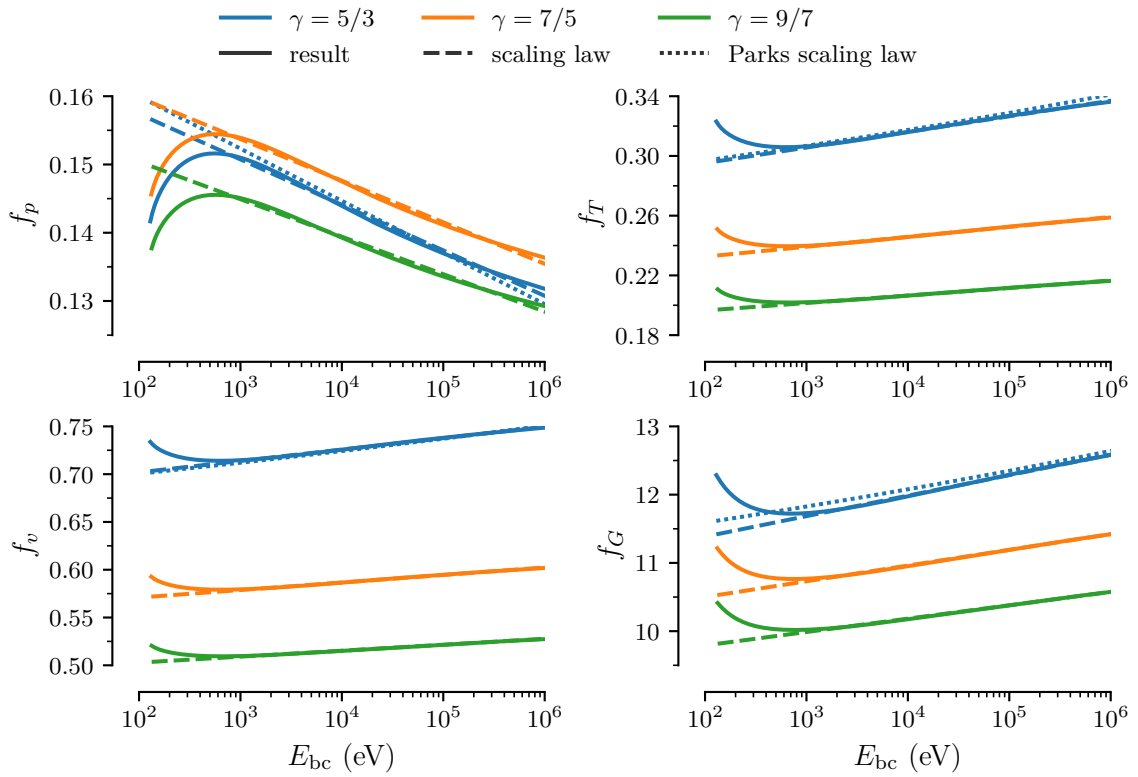

Figure 4.6: Weak dependence on γ and E_{bc} of the dimensionless prefactors for $p_\star$, $T_\star$, $v_\star$ and G of the isotropic NGS model in eqs. (4.29) to (4.32).

NGS model. This includes the approximation of a radial flux of electrons being equivalent to the parallel flux along the magnetic field lines, as represented by eq. (4.8). Linearizing the set of equations in the perturbation quantities δy, combined with the fact that the quantities y_0 satisfy those equations themselves, yields

the ideal gas law

$$\delta\rho = m\frac{\delta p}{T_0} - m\frac{p_0}{T_0^2}\,\delta T\ , \tag{4.34}$$

the mass conservation equation

$$\vec{\nabla}\cdot(\delta\rho\,\vec{v}_0 + \rho_0\,\delta\vec{v}) = 0\,, \tag{4.35}$$

the momentum conservation equation

$$\rho_0(\vec{v}_0\cdot\vec{\nabla})\,\delta\vec{v} + \rho_0(\delta\vec{v}\cdot\vec{\nabla})\vec{v}_0 + \delta\rho\,(\vec{v}_0\cdot\vec{\nabla})\vec{v}_0 = -\vec{\nabla}\,\delta p\ , \tag{4.36}$$

the energy conservation equation

$$\vec{\nabla}\cdot\left[\left(\frac{1}{2}\rho_0 v_0^2 + \frac{\gamma}{\gamma-1}p_0\right)\delta\vec{v} + \left(\frac{1}{2}\,\delta\rho\,v_0^2 + \rho_0(\vec{v}_0\cdot\delta\vec{v}) + \frac{\gamma}{\gamma-1}\,\delta p\right)\vec{v}_0\right] = \mu\frac{\partial\,\delta q}{\partial r}\ , \tag{4.37}$$

the electron energy loss equation

$$\frac{\partial\,\delta E}{\partial r} = 2\frac{\delta\rho}{m}L(E_0) + 2\frac{\rho_0}{m}\left.\frac{\partial L}{\partial E}\right|_{E_0}\delta E \tag{4.38}$$

and the effective heat flux equation

$$\frac{\partial\,\delta q}{\partial r} = \frac{\delta\rho}{m} q_0 \Lambda(E_0) + \frac{\rho_0}{m}\,\delta q\,\Lambda(E_0) + \frac{\rho_0}{m} q_0 \left.\frac{\partial\Lambda}{\partial E}\right|_{E_0} \delta E\ . \tag{4.39}$$

Now we want to find a set of equations for the r-dependence and a separate set of equations for the θ-dependence. Fortunately, this is possible without further approximations by expanding the perturbation in terms of general fully orthogonal basis functions $\{X_l(\theta)\}$ in the form

$$\begin{aligned} \delta\rho &= \sum_l \rho_l(r) X_l(\theta)\,, \quad & \delta p &= \sum_l p_l(r) X_l(\theta)\,, \\ \delta T &= \sum_l T_l(r) X_l(\theta)\,, \quad & \delta v_r &= \sum_l v_{l,r}(r) X_l(\theta)\,, \\ \delta q &= \sum_l q_l(r) X_l(\theta)\,, \quad & \delta E &= \sum_l E_l(r) X_l(\theta)\,, \end{aligned} \tag{4.40}$$

while expanding only δv_θ in terms of a different general basis[6] $\{X'_l(\theta)\}$ as

$$\delta v_\theta = \sum_l v_{l,\theta}(r) X'_l(\theta)\,. \tag{4.41}$$

Taking the derivatives in terms of spherical coordinates, the only θ-derivative appearing in eqs. (4.35) and (4.37) is

$$\vec{\nabla}\cdot(\delta v_\theta\,\hat{\theta}) = \frac{1}{r\sin\theta}\frac{\partial}{\partial\theta}(\sin\theta\,\delta v_\theta)\,,$$

while all other terms are linear in the θ-dependence. Therefore, separating the r-from the θ-dependence in those equations is possible by requiring

$$X_l(\theta) \propto \frac{1}{\sin\theta}\frac{\partial}{\partial\theta}(\sin\theta X'_l(\theta))\,. \tag{4.42}$$

Similarly, the only θ-derivative in eq. (4.36) is

$$\hat{\theta}\cdot\vec{\nabla}\,\delta p = \frac{1}{r}\frac{\partial\,\delta p}{\partial\theta}\,,$$

while the only other components in the $\hat{\theta}$-direction are linear in δv_θ. This leads us to require

$$X'_l(\theta) = \frac{\partial X_l}{\partial\theta}\,. \tag{4.43}$$

The last two eqs. (4.38) and (4.39) by design do not contain θ-derivatives or δv_θ. Combining those two requirements of eqs. (4.42) and (4.43) and choosing the proportionality constant in eq. (4.42) to be $-1/(l(l+1))$ leads to the defining differential equation for associated Legendre polynomials $X_l(\theta) = P_l^0(\cos\theta)$. These are precisely the $m = 0$ spherical harmonics with no φ-dependence. Thus, the θ-dependence of

[6] We initially assume no relation between X_l and X'_l.

each mode l is known and leads to a set of equations for the r-dependent coefficients of each mode l. Note that the $l = 0$ mode is independent of θ, which motivates our choice of notation y_0 for the isotropic NGS model quantities.

After a rather lengthy derivation, the set of equations determining the r-dependence of the asymmetric neutral ablation cloud quantities is

$$\rho_l = m\left(\frac{p_l}{T_0} - \frac{p_0}{T_0^2}T_l\right), \tag{4.44}$$

$$\frac{\partial\rho_0}{\partial r}v_{l,r} + \rho_0\left[\frac{1}{r^2}\frac{\partial}{\partial r}\Big(r^2 v_{l,r}\Big) - \frac{l(l+1)}{r}v_{l,\theta}\right] + v_0\frac{\partial\rho_l}{\partial r} + \frac{1}{r^2}\frac{\partial}{\partial r}\Big(r^2 v_0\Big)\rho_l = 0\,, \tag{4.45}$$

$$\rho_0 v_0\frac{\partial v_{l,r}}{\partial r} + \rho_0\frac{\partial v_0}{\partial r}v_{l,r} + v_0\frac{\partial v_0}{\partial r}\rho_l = -\frac{\partial p_l}{\partial r}\,, \tag{4.46}$$

$$\rho_0 v_0\frac{\partial v_{l,\theta}}{\partial r} + \rho_0\frac{v_0}{r}v_{l,\theta} = -\frac{p_l}{r}\,, \tag{4.47}$$

$$\begin{aligned}&\left[v_{l,r}\frac{\partial}{\partial r} + \frac{1}{r^2}\frac{\partial}{\partial r}\Big(r^2 v_{l,r}\Big) - \frac{l(l+1)}{r}v_{l,\theta}\right]\left(\frac{1}{2}\rho v_0^2 + \frac{\gamma}{\gamma-1}p_0\right)\\ &+\left[v_0\frac{\partial}{\partial r} + \frac{1}{r^2}\frac{\partial}{\partial r}\Big(r^2 v_0\Big)\right]\left(\frac{1}{2}\rho_l v_0^2 + \rho_0 v_0 v_{l,r} + \frac{\gamma}{\gamma-1}p_l\right) = \mu\frac{\partial q_l}{\partial r}\,,\end{aligned} \tag{4.48}$$

while the electron dynamics in the neutral gas is described by

$$\frac{\partial E_l}{\partial r} = 2\frac{\rho_l}{m}L(E_0) + 2\frac{\rho_0}{m}\left.\frac{\partial L}{\partial E}\right|_{E_0}E_l\,, \tag{4.49}$$

$$\frac{\partial q_l}{\partial r} = \frac{\rho_l}{m}q_0\Lambda(E_0) + \frac{\rho_0}{m}q_l\Lambda(E_0) + \frac{\rho_0}{m}q_0\left.\frac{\partial\Lambda}{\partial E}\right|_{E_0}E_l\,. \tag{4.50}$$

Apart from enabling the separation of variables, expansion in terms of Legendre polynomials is convenient for calculating the pellet rocket force. As shown in section 4.1, the pellet rocket force only depends on the projection of $\delta\rho$, δv_r, δp and $\int \delta v_\theta\,\mathrm{d}\theta$ onto $P_1^0 = \cos\theta$ at the pellet surface. Since the ablation dynamics of all l-modes are independent here, only the $l = 1$ mode is needed in our model. Without loss of generality, it suffices to see the perturbation quantities as

$$\begin{aligned}&\delta\rho = \rho_1(r)\cos\theta\,, \quad \delta p = p_1(r)\cos\theta\,,\\ &\delta T = T_1(r)\cos\theta\,, \quad \delta\vec{v} = \hat{r}v_{1,r}(r)\cos\theta - \hat{\theta}v_{1,\theta}(r)\sin\theta\,,\\ &\delta q = q_1(r)\cos\theta\,, \quad \delta E = E_1(r)\cos\theta\,.\end{aligned} \tag{4.51}$$

Physically, this means that for positive coefficients $y_1(r)$, the full quantity $y(\vec{r})$ has slightly increased values in the positive $\hat{z}$ direction and slightly decreased values in the negative $\hat{z}$ direction, while at $z = 0$ the isotropic NGS model is unperturbed. Since only the angular velocity was expanded in the different basis $X_l'(\theta)$, the perturbation δv_θ is now proportional to $-\sin\theta$. In other words, the angular flow is going from positive z to negative z in the case of negative $v_{1,\theta}(r)$, and vice versa. However, the angular flow is always zero at $\theta = 0, \pi$ and the strongest at $\theta = \pi/2$.

The boundary conditions for the asymmetric NGS model quantities are derived from the general NGS boundary conditions in eq. (4.13) by assuming the perturbation to be small, which yields

$$\begin{gathered} q_1(r_p) = 0, \quad T_1(r_p) = 0, \quad v_{1,\theta}(r_p) = 0, \quad p_1(r \to \infty) = 0, \\ q_1(r \to \infty) = \frac{3}{2} \int_0^\pi q_{\mathrm{bc}}(\theta) \cos\theta \sin\theta \, \mathrm{d}\theta \,, \\ E_1(r \to \infty) = \frac{3}{2} \int_0^\pi E_{\mathrm{bc}}(\theta) \cos\theta \sin\theta \, \mathrm{d}\theta \,. \end{gathered} \tag{4.52}$$

Since introducing $v_{1,\theta}$ adds the need for one additional boundary condition, we assume $v_{1,\theta}(r_p) = 0$. The incoming electron heat flux and energy are projected onto the $\cos\theta$ mode, without assuming a particular θ-dependence.

Solving for the perturbative ablation dynamics is again not possible analytically, and the equations need to be prepared for numerical analysis. A convenient way to quantify the degree of asymmetry in the external heat source is by defining

$$q_{\mathrm{rel}} = \frac{q_1(\infty)}{q_0(\infty)} \quad \text{and} \quad E_{\mathrm{rel}} = \frac{E_1(\infty)}{E_0(\infty)} \,. \tag{4.53}$$

These two quantities are the only parameters needed in our asymmetric NGS model, on top of the isotropic NGS model parameters. The perturbation assumption requires $|q_{\mathrm{rel}}| \ll 1$ and $|E_{\mathrm{rel}}| \ll 1$. Furthermore, the signs determine which side of the ablation cloud receives a higher heat flux q or higher average electron energy E. Later on, it will be seen that in the case of drift induced plasmoid shielding asymmetry, as explained in sections 3.1.2 and 4.3, the average energy is typically higher on the side of lower heat flux[7], i.e. $E_{\mathrm{rel}}/q_{\mathrm{rel}} < 0$.

The previously presented normalization of the isotropic NGS model to the sonic radius allowed the complexity of the problem to be reduced by use of additional physics knowledge in the form of the speed of sound definition in eq. (4.20). Such additional knowledge is not available for our asymmetric NGS model. Nevertheless, it turns out to be convenient to also normalize the asymmetric NGS model quantities y_1 to the sonic radius, as

$$\begin{gathered} \widetilde{\rho}_1 = \frac{\rho_1}{\rho_\star q_{\mathrm{rel}}}, \quad \widetilde{p}_1 = \frac{p_1}{p_\star q_{\mathrm{rel}}}, \quad \widetilde{T}_1 = \frac{T_1}{T_\star q_{\mathrm{rel}}}, \quad \widetilde{v}_{1,r} = \frac{v_{1,r}}{v_\star q_{\mathrm{rel}}}, \quad \widetilde{v}_{1,\theta} = \frac{v_{1,\theta}}{v_\star q_{\mathrm{rel}}}, \\ \widetilde{q}_1 = \frac{q_1}{q_\star q_{\mathrm{rel}}}, \quad \widetilde{E}_1 = \frac{E_1}{E_\star q_{\mathrm{rel}}}, \end{gathered} \tag{4.54}$$

by including the degree of heat flux asymmetry q_{rel} in the definition. Together with normalizing the isotropic NGS model quantities y_0 as previously defined in eq. (4.17), this simplifies the perturbative heat source boundary conditions to

$$\widetilde{q}_1(\infty) = \widetilde{q}_0(\infty) \quad \text{and} \quad \widetilde{E}_1(\infty) = \widetilde{E}_0(\infty) \cdot \frac{E_{\mathrm{rel}}}{q_{\mathrm{rel}}}. \tag{4.55}$$

[7]Remember that the number of incoming electrons changes the heat flux but not the average energy.

Again, the tilde notation is dropped from now on and all quantities can be considered normalized, if not stated otherwise. Note that, in contrast to the normalized isotropic NGS model, the normalized perturbation quantities at the sonic radius are unknown.

The chosen normalization leaves the system of eqs. (4.44) to (4.50) nearly unchanged. In particular, the linearity in the perturbation quantities leads to a cancellation of all q_{rel} factors. The only changes in terms of new factors on the right side of the equations are

$$\begin{aligned} \tfrac{1}{m} \quad & \text{in eq. (4.44),} \\ \tfrac{1}{\gamma} \quad & \text{in eqs. (4.46) and (4.47),} \\ \tfrac{\gamma}{\gamma-1}\tfrac{2}{\lambda_\star \mu} \quad & \text{in eq. (4.48) and} \\ m\lambda_\star \quad & \text{in eqs. (4.49) and (4.50).} \end{aligned}$$

Therefore, apart from the normalized isotropic NGS model parameters γ, $E_\star$ and $\lambda_\star$, the only new parameter needed to determine the normalized asymmetric NGS model is $E_{\mathrm{rel}}/q_{\mathrm{rel}}$.

Since the derived system of equations is linear in both the perturbation quantities y_1 and their derivatives $\partial y_1/\partial r$, it is convenient to write the differential equations in terms of 6×6, y_0-dependent, matrices $A(r)$ and $B(r)$, such that

$$A\frac{\partial \vec{y}_1}{\partial r} = B\vec{y}_1 \quad \text{with} \quad \vec{y}_1 = (p_1, T_1, v_{1,r}, v_{1,\theta}, q_1, E_1)^T \,, \tag{4.56}$$

where ρ_1 was replaced through the linearized and normalized ideal gas law (eq. (4.44) without m). Symbolic computation allows us to find an analytic expression for $C = A^{-1}B$ so that

$$\frac{\partial \vec{y}_1}{\partial r} = C\vec{y}_1 \,. \tag{4.57}$$

Since this expression is large and those details are not necessary here, it is only given in appendix A.2. However, an important feature of C is that it contains the apparent singularity $1/(T_0 - v_0^2)$ in front of the first three rows. Requiring again that $\partial \vec{y}_1/\partial r$ is finite at the sonic radius leads to a matrix $(T_0 - v_0^2)C|_{r=1}$ of which the first three rows have rank 1. Thus, this requirement reduces the number of unknowns at the sonic radius by one through the obtained equation

$$v_{1,\theta}(r=1) = \left[\left(1 - \frac{\chi_\star}{2}\right) v_{1,r} + \left(1 + \frac{\chi_\star}{4}\right) T_1 - q_1 - \frac{\Psi_\star}{2\lambda_\star L(E=1)} E_1\right]_{r=1} \,, \tag{4.58}$$

where $\chi_\star$ and $\Psi_\star$ are shorthands defined by eq. (4.27). Equivalently to the normalized NGS model, the derivatives at $r = 1$ can then be evaluated using L'Hôpital's rule. The corresponding large expression for $C_\star = C|_{r=1}$ is given in appendix A.2. Having solved this apparent singularity, everything is provided to start finding numerical solutions.

4.2.4 Numerical solution of the asymmetric NGS model

The procedure to find the numerical solution of the normalized perturbation quantities is chosen to be similar to the procedure used for the isotropic dynamics. Even though

the chosen normalization in eq. (4.54) does not introduce unknown parameters into the system of equations, it also does not bring knowledge about starting values for numerical integration. It is difficult to start from the normalized pellet radius r_p because, there, the derivatives diverge. Starting from $r \to \infty$ is difficult to handle numerically. Having found a way to eliminate one unknown at $r = 1$ through eq. (4.58), this poses as a convenient starting point for solving the perturbation dynamics. The differential eq. (4.57) is solved for both increasing and decreasing r, and the guesses for $\vec{y}_1(r = 1)$ are adjusted so that the boundary conditions in eqs. (4.52) and (4.53) are fulfilled. Note, that reducing the unknowns at $r = 1$ also removed the need for one of the boundary conditions, and it turns out that $p_1(\infty) = 0$ is always fulfilled. The numerical methods used here are the same as those described in section 4.2.2. After adjustment of numerical tolerances and testing different optimization schemes, a robust algorithm was developed to reliably solve the asymmetric perturbation dynamics with high precision.

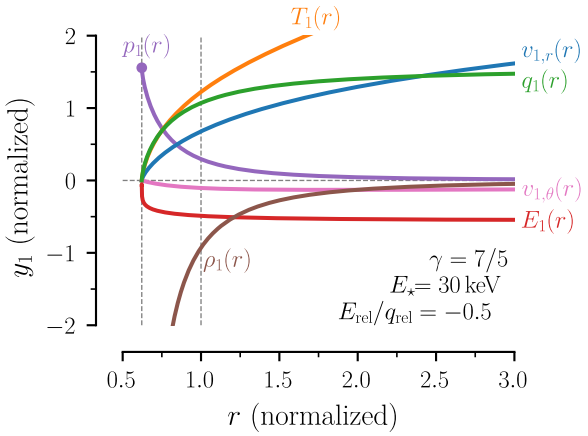

Figure 4.7: Radial dependence of a numerical example solution to the normalized perturbative ablation dynamics. The corresponding isotropic solution is shown in fig. 4.4 with the parameters $\gamma = 7/5$ and $E_\star(E_\mathrm{bc}) = 30\,\mathrm{keV}$. The heat source asymmetry is characterized here by $E_\mathrm{rel}/q_\mathrm{rel} = -0.5$.

An example solution is shown in fig. 4.7. This is the corresponding perturbation to the isotropic solution shown in fig. 4.4 ($\gamma = 7/5$, $E_\star = 30\,\mathrm{keV}$), with a heating asymmetry ratio $E_\mathrm{rel}/q_\mathrm{rel} = -0.5$. While this plot shows the radial dependence of the asymmetry perturbation, it might be easier to interpret the asymmetry through visualization of the full radial and angular dependence. Therefore, fig. 4.8 shows half of the 2D spatial variation of both the isotropic dynamics (on the left) and the asymmetric perturbation (on the right). The pellet is visualized by the grey circle in the middle, and the dashed line around it indicates the sonic radius. In reality, the neutral ablation cloud boundary is much further away than visualized, but it can be considered a zoomed-in view. Scalar quantities are presented through a variation in colour, where darker values mean higher absolute values. For the perturbation quantities, red means an increase and blue means a decrease compared to the isotropic NGS model. Note that this visualization shows all quantities as their normalized version, while the physical perturbation quantities are much smaller than the isotropic quantities. While both the isotropic pressure p_0 and the isotropic

density ρ_0 are largest close to the pellet surface, the pressure asymmetry p_1 shows opposite behaviour of the density asymmetry ρ_1. The quantities T, q, E show clearly that the major part of heating the neutral gas happens close to the pellet and the asymmetry in temperature T_1 follows the asymmetry in heat flux q_1. The flow velocity is presented as a vector field, showing a radial outflow in the isotropic dynamics and a flow from the upper side to the lower side is evident in the perturbation.

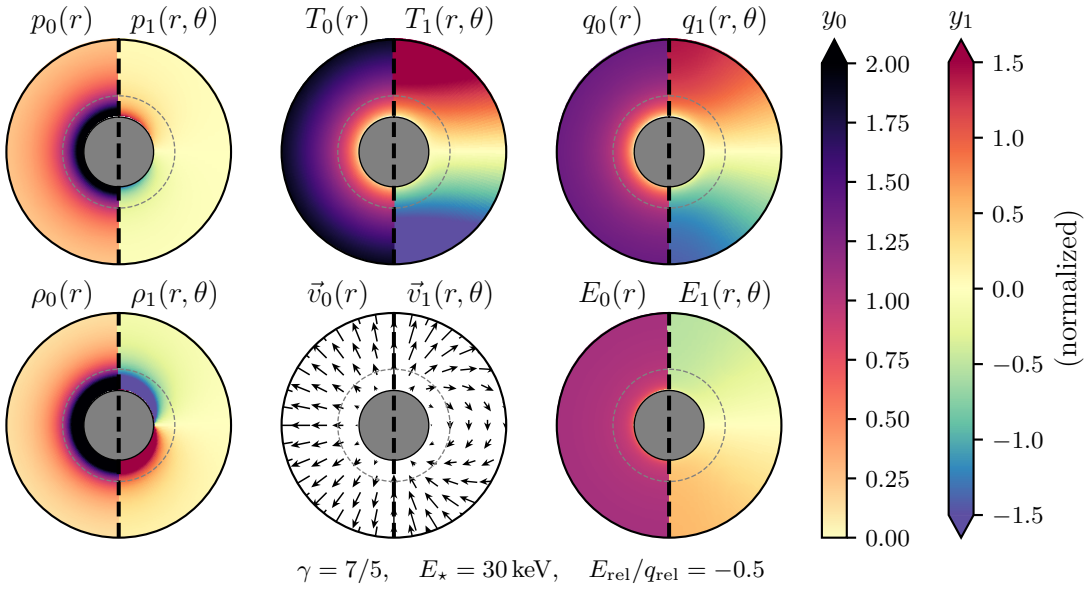

Figure 4.8: Full spatial dependence of the chosen numerical example solution for the perturbative ablation dynamics. The left sides show the NGS model solution, as in fig. 4.4. The right sides show the $\cos\theta$ perturbation solutions, with the radial dependence as shown in fig. 4.7. For illustrative purposes, $v_{1,\theta}$ is scaled up by a factor of 4. The dashed circle marks the sonic radius.

Overall, it must be noted that fig. 4.8 is only one specific solution. While the dynamics changes only slightly with γ and E_bc, the asymmetry parameter $E_\mathrm{rel}/q_\mathrm{rel}$ can change the dynamics on a qualitative level. The solution shown in fig. 4.8 agrees well with our expectation of how an asymmetric heat source changes the ablation dynamics. However, the two further solutions shown in fig. 4.9 give surprising insights into ablation physics.

With an increased average electron energy on the same side as the increased heat flux, i.e. $E_\mathrm{rel}/q_\mathrm{rel} = +1$, as shown in fig. 4.9a, the ablation cloud temperature and flow velocity can be larger on the opposite side. At first, this might seem unphysical. However, it can be understood, as the increased density leads to an increase in required energy to raise the temperature the same amount. It also leads to a higher pressure asymmetry at the pellet surface compared to the $E_\mathrm{rel}/q_\mathrm{rel} = -0.5$ dynamics.

Another qualitatively different solution, which is more relevant for modelling the pellet rocket effect, is shown in fig. 4.9b with $E_\mathrm{rel}/q_\mathrm{rel} = -1.5$. This means the asymmetry in average incident electron energy is opposite to the asymmetry in incident heat flux. This was, to a lesser extent, also the case in the first solution,

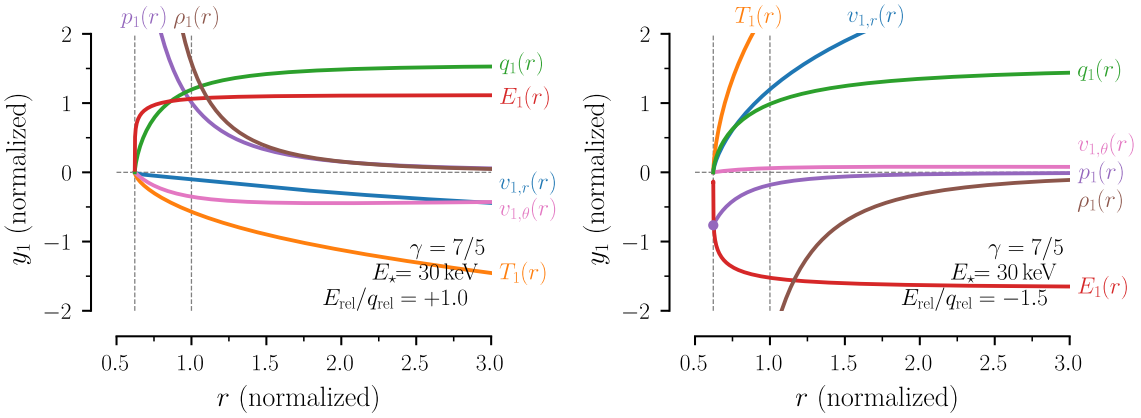

Figure 4.9: Further numerical solutions of the perturbative ablation dynamics. The corresponding isotropic quantities are shown in fig. 4.4. The left figure (with $E_{\mathrm{rel}}/q_{\mathrm{rel}} = +1$) shows a temperature increase on the low heat flux side. The right figure (with $E_{\mathrm{rel}}/q_{\mathrm{rel}} = -1.5$) shows a pressure increase on the low heat flux side, leading to a pellet rocket force towards the high heat flux side, the grey region indicates the pellet.

shown in fig. 4.7 with $E_{\mathrm{rel}}/q_{\mathrm{rel}} = -0.5$. However, here, the pressure asymmetry at the pellet radius becomes negative. This would result in a negative pellet rocket force, i.e. towards the high external heat flux side. Whether this reversed rocket force is physically accurate cannot be evaluated in this thesis. It might be an artifact from the approximations of mono-energetic electrons losing heat radially.

The three example solutions illustrate that the pellet rocket force, which stems mainly from $p_1(r_{\mathrm{p}})$, is highly dependent on $E_{\mathrm{rel}}/q_{\mathrm{rel}}$. To quantify this phenomenon, a parameter scan is performed over γ, E_{bc} and $E_{\mathrm{rel}}/q_{\mathrm{rel}}$. The corresponding optimized values at the sonic radius are shown in appendix A.3 for completeness. The resulting $p_1(r_{\mathrm{p}})$ are shown in fig. 4.10. Marked with a vertical dashed line is the value $E_{\mathrm{rel}}/q_{\mathrm{rel}} \approx -1.17$, where the pressure asymmetry, and consequently the pellet rocket force, changes polarity. Prominently, the dependence on $E_{\mathrm{rel}}/q_{\mathrm{rel}}$ is found to be purely linear, with the slope and position only depending weakly on γ and E_{bc}. Linear regression has shown relative fit errors of less than 1% in the tested orders of magnitude of $|E_{\mathrm{rel}}/q_{\mathrm{rel}}|$ from 1×10^{-2} to 1×10^{6}. This linear dependence is convenient, since it allows for a simple semi-analytical formula connecting the normalized pressure asymmetry to the degree of asymmetry of the external heating source

$$p_1(r_{\mathrm{p}}) = a \cdot \left(\frac{E_{\mathrm{rel}}}{q_{\mathrm{rel}}} - b \right) , \tag{4.59}$$

where a is the slope and b is the root (where $p_1(r_{\mathrm{p}})$ changes polarity). The fit parameters are found to be $a \approx 2.0$ to 2.9 and $b \approx -1.21$ to -1.17. The explicit dependence on γ and E_{bc} values is shown in fig. 4.11. Corresponding scaling laws are provided in appendix A.1.

There is one special case that has been neglected in our analysis. If there is no asymmetry in the external heat flux, i.e. $q_{\mathrm{rel}} = 0$, but the average energy of incident

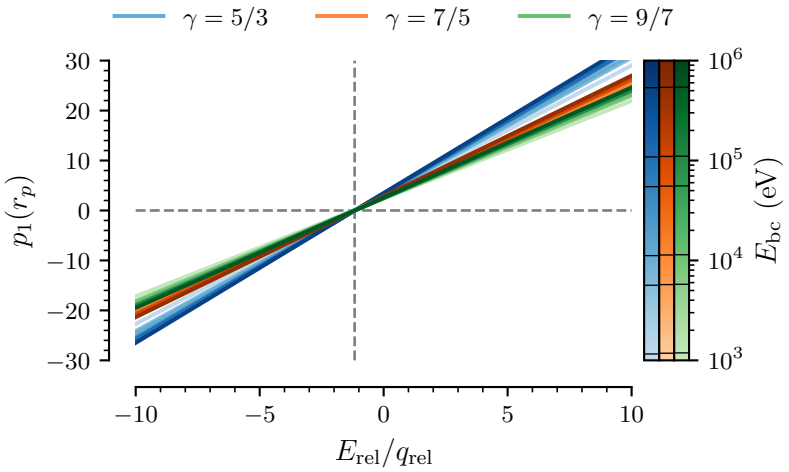

Figure 4.10: Linear dependence of the pressure asymmetry at the pellet surface on the parameter $E_{\mathrm{rel}}/q_{\mathrm{rel}}$. The vertical dashed line at -1.17 shows the change in polarity. The colour of the lines denote γ, while the brightness denotes E_{bc}, with the exact values shown by the black lines on the colour bars.

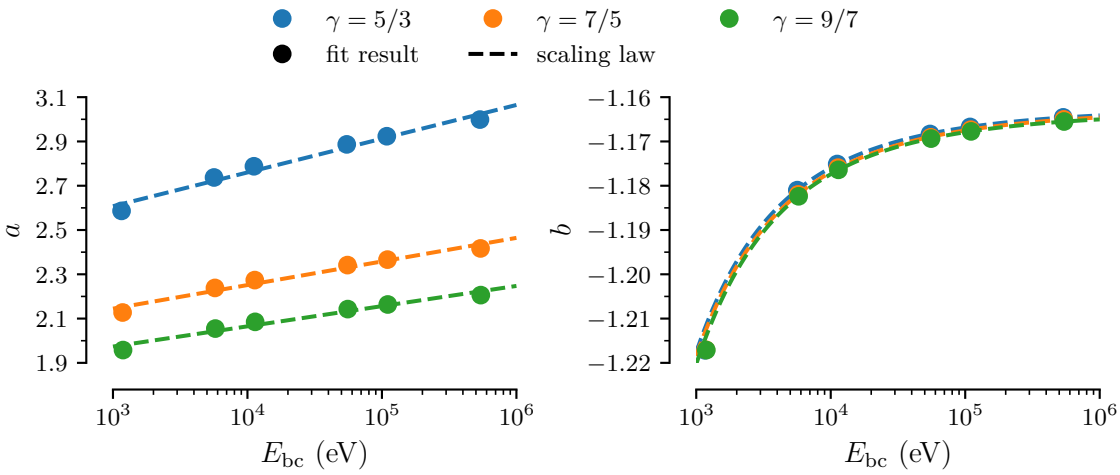

Figure 4.11: Linear regression parameters for $p_1(r_{\mathrm{p}})$ dependence on $E_{\mathrm{rel}}/q_{\mathrm{rel}}$. Shown is the dependence on γ and E_{bc}. a is the slope and b is the value at which $p_1(r_{\mathrm{p}})$ changes sign.

electrons varies over the $\hat{z}$-axis, i.e. $E_{\mathrm{rel}} \neq 0$, the chosen normalization in eq. (4.54) is not valid. In the same way that the factor q_{rel} cancelled out in the normalized system of equations, the expressions remain unchanged when normalizing to E_{rel} instead. Only the normalized boundary conditions change to

$$\frac{q_1(r \to \infty)}{q_\star E_{\mathrm{rel}}} = 0 \quad \text{and} \quad \frac{E_1(r \to \infty)}{E_\star E_{\mathrm{rel}}} = \widetilde{E}_0(r \to \infty)\,. \tag{4.60}$$

Solving the dynamics numerically in the same way as before yields similar results as for $q_{\mathrm{rel}} \neq 0$. It is found that

$$\frac{p_1(r_p)|_{q_{\mathrm{rel}}=0}}{p_\star E_{\mathrm{rel}}} = a\,, \tag{4.61}$$

with the same values of a as shown in fig. 4.11.

Finally, it was mentioned in section 4.1 that the pellet rocket force depends mainly on $p_1(r_{\mathrm{p}})$. This statement will now be supported by evidence, given our choice of approximations and boundary conditions. Inserting the normalized perturbation quantities into the formula for the pellet rocket force in eq. (4.2) and using the definition of the sound speed ($\rho_\star v_\star^2 = \gamma p_\star$) gives

$$F = \frac{4\pi r_{\mathrm{p}}^2}{3} p_\star q_{\mathrm{rel}} \underbrace{\left(\gamma \widetilde{v}_0^2 \widetilde{\rho}_1 + 2\gamma \widetilde{\rho}_0 \widetilde{v}_0 (\widetilde{v}_{1,r} - \widetilde{v}_{1,\theta}) + \widetilde{p}_1\right)_{r=r_{\mathrm{p}}}}_{\widetilde{F}}\,. \tag{4.62}$$

The chosen boundary condition $v_{1,\theta}(r_{\mathrm{p}}) = 0$ together with the fact that $r^2 \rho_0 v_0^2 = \textit{const.}$ results in the corresponding term in the force being zero. Asymptotic analysis on the other terms is non-trivial, since $v_0(r_{\mathrm{p}}) \to 0$ and $v_{1,r}(r_{\mathrm{p}}) \to 0$ but $\rho_0(r_{\mathrm{p}}) \to \infty$ and $\rho_1(r_{\mathrm{p}}) \to \infty$. Therefore, this analysis has to be done numerically and fig. 4.12 shows the relative contribution of the non-pressure terms in $\widetilde{F}$. This shows clearly that the pressure asymmetry is the only quantity that is important for the pellet rocket force, whereas adding other terms would change the result only in the third or fourth significant figure. Note that the noise in fig. 4.12 is a result of accumulated numerical errors when calculating the numerical solutions and a finite precision when optimizing the boundary conditions. However, the achieved numerical precision is considered sufficient, given the approximations of the NGS model.

Overall, it has been shown here that it is possible to find numerical solutions to the perturbative dynamics in the neutral ablation cloud. A semi-analytical model for the pellet rocket force is derived as

$$\boxed{F = \frac{4\pi r_{\mathrm{p}}^2}{3} p_\star \left(a E_{\mathrm{rel}} - ab q_{\mathrm{rel}}\right)\,,} \tag{4.63}$$

by combining eqs. (4.59) and (4.62), with $p_\star$ given through eq. (4.29) and a and b given in fig. 4.11. Therefore, only the shielding of the neutral ablation cloud from the background plasma electrons is still needed to model the pellet rocket effect. How the plasmoid shielding leads to estimates for the parameters E_{bc}, q_{bc}, E_{rel} and q_{rel} is the topic of the next section.

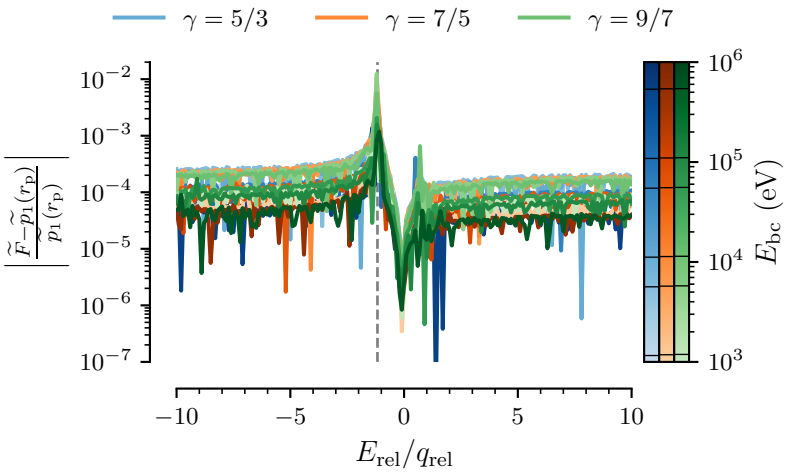

Figure 4.12: Relative contribution of non-pressure asymmetry ($\widetilde{p}_1(r_\mathrm{p})$) quantities to the dimensionless terms $\widetilde{F}$ in the pellet rocket force.

4.3 Plasmoid shielding

Even though the major part of the heating occurs in the neutral gas close to the pellet, the electrons already lose some energy while traversing the ionized part of the ablation cloud. This *plasmoid shielding* of the background plasma electrons depends mainly on the integrated density along the electron path through the plasmoid. As described in section 3.1.2, the ablated material becomes confined by the magnetic field lines once it is ionized, while the pellet and the neutral ablation cloud move unaffected by the magnetic field. Additionally, the plasmoid drifts towards the low-field side due to an $\vec{E} \times \vec{B}$-drift, as described in section 3.1.2. In section 4.3.1 we quantify how the drift of the ionized ablation material leads to a varying shielding length across the magnetic field lines, which in turn affects the pellet ablation dynamics. section 4.3.2 describes then our model for calculating the effective heat flux and effective electron energy arriving at the neutral cloud and their asymmetries, which are considered as boundary conditions for the neutral ablation cloud dynamics.

4.3.1 Drift induced shielding length asymmetry

As described in section 3.1, the flow velocity at the boundary of the neutral ablation cloud rapidly drops to subsonic speeds and a shock front forms. Beyond this shock front, at ionization radius[8] r_i, the ablated material can be considered fully ionized and forms the plasmoid ablation cloud. Radial expansion of the plasmoid due to heating is restricted in the direction perpendicular to the magnetic field lines. Thus, the plasmoid expands in a tube parallel to the field lines at the speed of sound

$$c_\mathrm{s} = \sqrt{\frac{(\gamma_e \langle Z \rangle + \gamma_i) T_\mathrm{pl}}{\langle m_i \rangle}}\,, \tag{4.64}$$

[8]Not to be confused with the sonic radius $r_\star$ much closer to the pellet.

where plasmoid temperature T_{pl} (in units of energy). In the case of pellets containing only a given hydrogen isotope, the adiabatic indices are $\gamma_e = 1$, $\gamma_i = 3$, the average charge number is $\langle Z \rangle = 1$ and the average ion mass is $\langle m_i \rangle = m_{\mathrm{H}}$, m_{D} or m_{T} (Vallhagen et al., 2023).

Assuming the pellet is injected radially inwards from the low-field side, the ionized ablated material initially moves, relative to the pellet, at the pellet velocity v_{p} outward along the major radius. Additionally, the $\vec{E} \times \vec{B}$-drift towards the low-field side gradually accelerates material across the field lines and the plasmoid bends outwards compared to the flux surfaces, as illustrated in fig. 4.13. As modelled by Vallhagen et al. (2023), plasmoid material at the major radius R_{m} is under constant acceleration

$$\dot{v}_{\mathrm{pl}} = \frac{2(1 + \langle Z \rangle)}{\langle m_i \rangle R_{\mathrm{m}}} \left(T_{\mathrm{pl}} - \frac{2 n_{\mathrm{bg}}}{(1 + \langle Z \rangle) n_{\mathrm{pl}}} T_{\mathrm{bg}} \right) \tag{4.65}$$

shortly after ionization, where T_{bg} and n_{bg} are the electron temperature and electron density of the background plasma and n_{pl} is the electron density in the plasmoid.

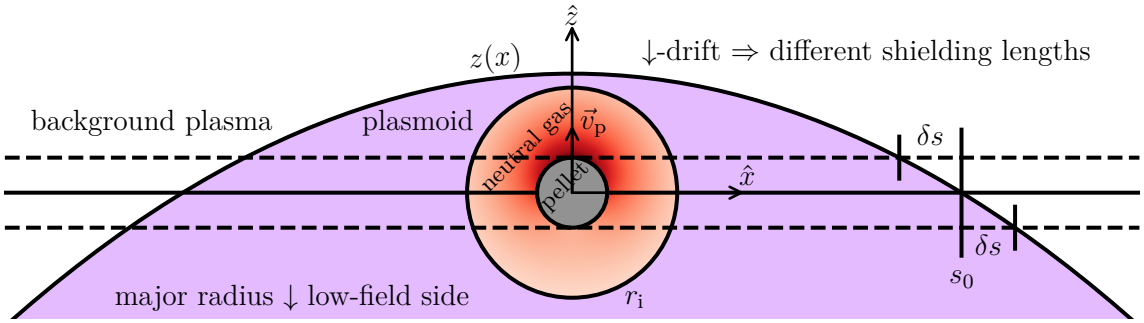

Figure 4.13: Illustration of the plasmoid shielding asymmetry of the ablation cloud. The drift towards the low-field side induces a shorter shielding length at the high-field side. Note that this is not to scale. The pellet is much smaller than the neutral ablation cloud and the plasmoid shielding length is much longer than the ionization radius, with a less pronounced shielding length difference.

Since the particles, once ionized, stop their motion in the positive $\hat{z}$-direction nearly instantaneously, the plasmoid boundary $z(x)$, as depicted in fig. 4.13 with the pellet at the origin, is determined by the trajectory of particles, which are ionized at $(x = 0, z = r_{\mathrm{i}})$. These particles follow the equation of motion

$$\vec{r}(t) = (\pm c_{\mathrm{s}} t)\hat{x} + \left(r_{\mathrm{i}} - v_{\mathrm{p}} t - \frac{1}{2} \dot{v}_{\mathrm{pl}} t^2 \right) \hat{z} \,. \tag{4.66}$$

The shielding length $s(z)$ along a field line at position z is the distance from the plasmoid boundary to the neutral ablation cloud boundary (which lies at $x = \pm\sqrt{r_{\mathrm{i}}^2 - z^2}$). Therefore, the shielding length can be estimated by eliminating the time dependence

in the equation of motion[9] and taking the absolute value, which gives

$$s(z) = c_\mathrm{s}\left(-\frac{v_\mathrm{p}}{\dot{v}_\mathrm{pl}} + \sqrt{\left(\frac{v_\mathrm{p}}{\dot{v}_\mathrm{pl}}\right)^2 + \frac{2}{\dot{v}_\mathrm{pl}}(r_\mathrm{i} - z)}\right) - \sqrt{r_\mathrm{i}^2 - z^2}\,. \tag{4.67}$$

The spherically symmetric ablation dynamics are considered to be determined solely through the central shielding length

$$s_0 = s(z=0) = c_\mathrm{s}\frac{v_\mathrm{p}}{\dot{v}_\mathrm{pl}}\left(-1 + \sqrt{1 + \frac{2\dot{v}_\mathrm{pl}}{v_\mathrm{p}^2}r_\mathrm{i}}\right) - r_\mathrm{i}\,. \tag{4.68}$$

The asymmetry in the neutral ablation cloud heating is determined by the shielding length variation δs across the field lines hitting the pellet. Ideally, one would consider the shielding length variation across the whole neutral ablation cloud. However, this would largely overestimate the degree of asymmetry in our model. The reason follows from the approximation of a purely radial flux of electrons $\vec{\nabla}\cdot\vec{q} \approx \partial q/\partial r$, as illustrated in fig. 4.2. Since the heating close to the pellet surface dominates, the field lines in the interval $z \in [-r_\mathrm{p}, r_\mathrm{p}]$ are assumed to correspond to the full range $\theta \in [0, \pi]$ of heat flux in our model. Under the assumption that the shielding length varies nearly linear in this interval, the variation becomes

$$\delta s\,(z) = \left.\frac{\mathrm{d}s}{\mathrm{d}z}\right|_{z=0} \cdot z = \left.\frac{\mathrm{d}s}{\mathrm{d}z}\right|_{z=0} \cdot r_\mathrm{p}\cos\theta\,, \tag{4.69}$$

$$\text{with} \quad \left.\frac{\mathrm{d}s}{\mathrm{d}z}\right|_{z=0} = \frac{-c_\mathrm{s}}{\sqrt{v_\mathrm{p}^2 + 2\dot{v}_\mathrm{pl}r_\mathrm{i}}}\,. \tag{4.70}$$

4.3.2 Heat flux attenuation

The full dynamics of hot electrons losing energy while traversing a colder plasma involves multiple different mechanisms. A rigorous description of this plasma shielding is ultimately kinetic, and it is outside the scope of this thesis. Therefore, we approximate the heat flux attenuation by assuming that electrons only reach the neutral ablation cloud if their mean free path λ_mfp is longer than the distance d that they travel through the plasmoid. Additionally, we assume that the electrons which reach the neutral ablation cloud are unaffected by the plasmoid and retain their thermal kinetic energy from the background plasma.

Although the electrons travel along the magnetic field lines according to the shielding lengths, as derived in section 4.3.2, their gyration around the field line leads to a longer total distance travelled through the plasmoid. Let ξ be the cosine of the pitch angle of an electron, i.e. the angle between the total velocity vector $\vec{v}_e$ and the velocity $\vec{v}_\parallel$ parallel to the magnetic field line. Assuming the pitch angle of each electron stays constant while traversing the plasmoid, electrons contribute to heating the neutral ablation cloud if

$$d = \frac{s}{\xi} < \lambda_\mathrm{mfp}\,. \tag{4.71}$$

[9] We assume a constant acceleration over the whole trajectory.

Hot electrons slowing down in a cold plasma (the plasmoid) experience dominant collisions with the cold plasma electrons. The corresponding mean free path is

$$\lambda_{\mathrm{mfp}} = \frac{v_e}{\nu_{ee}} = \frac{4\pi\varepsilon_0^2 m_e^2 v_e^4}{n_{\mathrm{pl}} e^4 \ln\Lambda} = \left(\frac{v_e}{v_{\mathrm{th}}}\right)^4 \lambda_T \,, \tag{4.72}$$

with the collision frequency ν_{ee}, the hot electron velocity v_e, the cold electron density n_{pl} in the plasmoid and the electron mass m_e (Helander & Sigmar, 2005). For convenience, we define the mean free path λ_T at thermal velocity $v_{\mathrm{th}} = \sqrt{2T_{\mathrm{bg}}/m_e}$. The Coulomb-logarithm

$$\ln\Lambda = \ln\left(\lambda_{\mathrm{D}} \cdot b_{\mathrm{min}}^{-1}\right) = \ln\left(\sqrt{\frac{\varepsilon_0 T_{\mathrm{pl}}}{n_{\mathrm{pl}} e^2}} \cdot \left(\frac{\langle Z\rangle e^2}{2\pi\varepsilon_0 m_e v_{\mathrm{th}}^2}\right)^{-1}\right) \tag{4.73}$$

is the order of magnitude of the number of particles in the Debye sphere of the plasma, which is typically between 10 and 20 in MCF plasmas (Helander & Sigmar, 2005).

Since the mean free path depends mainly on the hot electron velocity, the condition for passing through the plasmoid unaffected can be written in terms of a critical velocity v_{c} as

$$v_e > v_{\mathrm{c}} \quad \text{with} \quad v_{\mathrm{c}} = \left(\frac{s}{\xi\lambda_T}\right)^{\frac{1}{4}} v_{\mathrm{th}} \,. \tag{4.74}$$

We assume that the hot electrons in the background plasma are distributed according to the three-dimensional Maxwellian distribution

$$f_{\mathrm{Maxwell}}(\vec{v}) = \left(\frac{1}{\sqrt{\pi} v_{\mathrm{th}}}\right)^3 \exp\left[-\left(\frac{v}{v_{\mathrm{th}}}\right)^2\right] . \tag{4.75}$$

Then, the heat flux boundary condition for the neutral ablation cloud can be estimated by averaging the energy flux $q(\vec{v})$ over the velocities sufficient to pass through the plasmoid as

$$q_{\mathrm{pl}} = \iiint\limits_{\substack{|\vec{v}_e|>v_{\mathrm{c}} \\ \xi\in[0,1]}} \underbrace{\underbrace{\xi v_e}_{v_\parallel} \frac{m_e v_e^2}{2} n_{\mathrm{bg}} \, f_{\mathrm{Maxwell}}(\vec{v}_e)}_{q(\vec{v}_e)} \, \mathrm{d}^3 v_e \,. \tag{4.76}$$

This integral can be solved exactly by substituting $u := v_e/v_{\mathrm{th}} \Rightarrow u(v_{\mathrm{c}}) = (\xi\alpha)^{-1/4}$, with the shorthand $\alpha := \lambda_T/s$. The result is

$$\boxed{q_{\mathrm{pl}}(s) = \underbrace{2\sqrt{\frac{T_{\mathrm{bg}}^3}{2\pi m_e}} n_{\mathrm{bg}}}_{q_{\mathrm{Parks}}} \underbrace{\frac{1}{\alpha^2}\left[e^{\frac{-1}{\sqrt{\alpha}}}\left(-\frac{1}{2}\sqrt{\alpha} + \frac{1}{2}\alpha + \alpha^{3/2} + \alpha^2\right) - \frac{1}{2}\mathrm{Ei}\left(-\frac{1}{\sqrt{\alpha}}\right)\right]}_{f_q(\alpha)}} \,, \tag{4.77}$$

with the exponential integral $\mathrm{Ei}(x) = -\int_{-x}^{\infty} \exp(-t)/t \, \mathrm{d}t$. Consequently, the heat flux without any plasmoid shielding q_{Parks}, as assumed by Parks and Turnbull (1978), is scaled down in our model by the shielding length-dependent dimensionless function $f_q(\alpha)$.

The effective electron energy at the neutral ablation cloud boundary is assumed to be

$$E_{\mathrm{pl}} = \frac{q_{\mathrm{pl}}}{\Gamma_{\mathrm{pl}}} , \tag{4.78}$$

where the particle flux Γ_{pl} of electrons reaching the neutral ablation cloud is estimated similarly to the heat flux as

$$\Gamma_{\mathrm{pl}}(\theta) = \iiint\limits_{\substack{|\vec{v}_e|>v_c \\ \xi\in[0,1]}} \underbrace{\xi v_e n_{\mathrm{bg}}}_{\Gamma(\vec{v}_e)} f_{\mathrm{Maxwell}}(\vec{v}_e) \, \mathrm{d}^3 v_e \ . \tag{4.79}$$

The result is again a scaling of the effective energy assumed by Parks and Turnbull (1978) E_{Parks} by a dimensionless function $f_E(\alpha)$, as

$$\boxed{E_{\mathrm{pl}}(s) = \underbrace{2T_{\mathrm{bg}}}_{E_{\mathrm{Parks}}} \underbrace{\left[\frac{e^{\frac{-1}{\sqrt{\alpha}}} \left(-\frac{1}{2}\sqrt{\alpha} + \frac{1}{2}\alpha + \alpha^{3/2} + \alpha^2 \right) - \frac{1}{2}\mathrm{Ei}\left(-\frac{1}{\sqrt{\alpha}} \right)}{e^{\frac{-1}{\sqrt{\alpha}}} \left(+\frac{1}{2}\sqrt{\alpha} - \frac{1}{2}\alpha + \alpha^{3/2} + \alpha^2 \right) + \frac{1}{2}\mathrm{Ei}\left(-\frac{1}{\sqrt{\alpha}} \right)} \right]}_{f_E(\alpha)} .} \tag{4.80}$$

The dimensionless functions $f_q(\alpha)$ and $f_E(\alpha)$ are visualized in fig. 4.14. While increasing shielding length s, i.e. decreasing α, attenuates the heat flux, the average energy is enhanced. This can be explained qualitatively by noticing that, with a longer shielding length through the plasmoid, fewer electrons reach the neutral cloud, but on average, those electrons are more energetic. Whether the quantitative prediction of this effect is accurate will need further investigation.

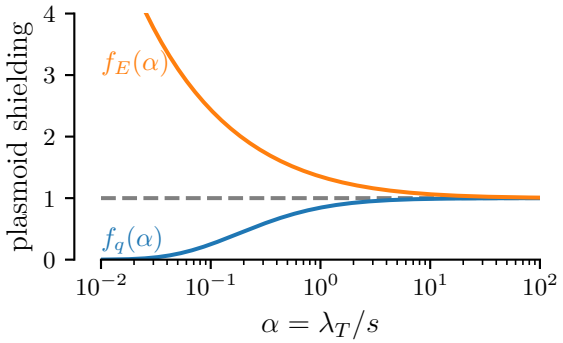

Figure 4.14: Scaling functions for the heat flux and energy boundary conditions due to plasmoid shielding, inversely depending on the shielding length s.

After modelling how the heat flux and effective energy into the neutral ablation cloud depends on the shielding length, it can be combined with the shielding length

prediction across different field lines to provide expressions for the boundary conditions to our model. The central shielding length s_0 in eq. (4.68) directly determines the boundary conditions to the isotropic NGS model as

$$\boxed{\begin{aligned} q_{\mathrm{bc}} &= q_{\mathrm{pl}}(s_0) = q_{\mathrm{Parks}} f_q(\alpha_0) \qquad \text{and} \\ E_{\mathrm{bc}} &= E_{\mathrm{pl}}(s_0) = E_{\mathrm{Parks}} f_E(\alpha_0) \end{aligned}}, \tag{4.81}$$

with $\alpha_0 := \lambda_T / s_0$.

The degree of asymmetry in heating the neutral ablation cloud depends on the shielding length variation given in eqs. (4.69) and (4.70). However, an additional source of asymmetry are the temperature and electron density gradients of the background plasma. Consider thus the first order variation

$$\delta q_{\mathrm{pl}}(z) = \left.\frac{\mathrm{d}q_{\mathrm{pl}}}{\mathrm{d}z}\right|_{z=0} z \tag{4.82}$$

$$= \left[\frac{\partial q_{\mathrm{pl}}}{\partial T_{\mathrm{bg}}}\frac{\mathrm{d}T_{\mathrm{bg}}}{\mathrm{d}z} + \frac{\partial q_{\mathrm{pl}}}{\partial n_{\mathrm{bg}}}\frac{\mathrm{d}n_{\mathrm{bg}}}{\mathrm{d}z} + \frac{\partial q_{\mathrm{pl}}}{\partial \alpha}\left(\frac{\partial \alpha}{\partial T_{\mathrm{bg}}}\frac{\mathrm{d}T_{\mathrm{bg}}}{\mathrm{d}z} + \frac{\partial \alpha}{\partial s}\frac{\mathrm{d}s}{\mathrm{d}z}\right)\right]_{z=0} z \tag{4.83}$$

$$= \left[\frac{3}{2}\frac{q_{\mathrm{pl}}}{T_{\mathrm{bg}}}\frac{\mathrm{d}T_{\mathrm{bg}}}{\mathrm{d}z} + \frac{q_{\mathrm{pl}}}{n_{\mathrm{bg}}}\frac{\mathrm{d}n_{\mathrm{bg}}}{\mathrm{d}z} + q_{\mathrm{Parks}} f_q'\left(\frac{2\alpha}{\sqrt{T_{\mathrm{bg}}}}\frac{\mathrm{d}T_{\mathrm{bg}}}{\mathrm{d}z} - \frac{\alpha}{s}\frac{\mathrm{d}s}{\mathrm{d}z}\right)\right]_{z=0} z\,, \tag{4.84}$$

where f_q' denotes $\partial f_q / \partial \alpha$. While the heat flux asymmetry depends on the temperature and density gradients, this dependence is assumed to be negligible for the shielding length. Thus $\partial \alpha / \partial T_{\mathrm{bg}}$ is derived from the definition of λ_T in eq. (4.72) alone[10]. Equivalently to the shielding length variation, we let $z = r_{\mathrm{p}} \cos\theta$. Consequently, the variation δq_{pl} corresponds to $q_1(\infty)\cos\theta$ in our asymmetric NGS model. Comparison to the definition of the heat flux asymmetry parameter in eq. (4.53) then leads to

$$q_{\mathrm{rel}} = \frac{q_1(\infty)}{q_{\mathrm{bc}}} = \frac{1}{q_{\mathrm{pl}}(s_0)} \left.\frac{\mathrm{d}q_{\mathrm{pl}}}{\mathrm{d}z}\right|_{z=0} r_{\mathrm{p}}\,. \tag{4.85}$$

Inserting the expressions of eqs. (4.81) and (4.84) and performing an equivalent derivation for the effective energy asymmetry finally gives

$$\boxed{\begin{aligned} q_{\mathrm{rel}} &= r_{\mathrm{p}} \left[\left(\frac{3}{2}\frac{1}{T_{\mathrm{bg}}} + \frac{f_q'}{f_q}\frac{2\alpha}{\sqrt{T_{\mathrm{bg}}}}\right)\frac{\mathrm{d}T_{\mathrm{bg}}}{\mathrm{d}z} + \frac{1}{n_{\mathrm{bg}}}\frac{\mathrm{d}n_{\mathrm{bg}}}{\mathrm{d}z} - \frac{f_q'}{f_q}\frac{\alpha}{s}\frac{\mathrm{d}s}{\mathrm{d}z}\right]_{z=0} \qquad \text{and} \\ E_{\mathrm{rel}} &= r_{\mathrm{p}} \left[\left(\frac{1}{T_{\mathrm{bg}}} + \frac{f_E'}{f_E}\frac{2\alpha}{\sqrt{T_{\mathrm{bg}}}}\right)\frac{\mathrm{d}T_{\mathrm{bg}}}{\mathrm{d}z} - \frac{f_E'}{f_E}\frac{\alpha}{s}\frac{\mathrm{d}s}{\mathrm{d}z}\right]_{z=0} \end{aligned}}, \tag{4.86}$$

where the plasmoid shielding functions $f_q(\alpha)$ and $f_E(\alpha)$ are given by eqs. (4.77) and (4.80), and the shielding length variation $\mathrm{d}s/\mathrm{d}z|_{z=0}$ is described by eq. (4.70). Note that in this model, q_{rel} is always positive, but for a moderate temperature gradient, E_{rel} is always negative. Thus, $E_{\mathrm{rel}}/q_{\mathrm{rel}} \lesssim -1.17$ is possible, which would mean a pellet rocket acceleration towards the high-field side, according to fig. 4.10.

[10] Neglecting also the Coulomb logarithm dependence $\partial \ln\Lambda / \partial T_{\mathrm{bg}}$.

In summary, the plasmoid shielding depends mainly on the pellet injection parameters v_p and r_p, the background plasma parameters T_bg and n_bg (and their gradients), and the pellet position along the major radius of the magnetic confinement device R_m. Since the plasmoid formation is not fully modelled here, values have to be given for the plasmoid temperature T_pl and the ionization radius r_i. Whereas, the plasmoid electron density can be estimated as

$$n_\mathrm{pl} = \frac{\mathcal{G}}{2\langle m_i \rangle c_\mathrm{s}(T_\mathrm{pl})\pi r_\mathrm{i}^2} \tag{4.87}$$

by considering that ablated material is outflowing at the mass ablation rate $\mathcal{G} = mG$ along a tube of cross-sectional area πr_i^2. Note that m is the mass of the ablated molecules, i.e. before dissociation, and $\langle m_i \rangle$ is the mass of the ionized atoms. However, the particle ablation rate G, as predicted by the isotropic NGS model in eq. (4.32), depends itself on the heat flux q_bc and effective electron energy E_bc. Therefore, the plasmoid shielding, as estimated by eq. (4.81), has to be calculated in a self-consistent iteration until the particle ablation rate G is converged. Then, the heat source asymmetry parameters in eq. (4.86) can be used in eq. (4.63) to predict the pellet rocket force.

4.4 Quantifying the radial acceleration of pellets in tokamaks

Having developed and presented our self-consistent semi-analytical model for the pellet rocket force, it can now be used to predict the magnitude of the radial pellet acceleration in example tokamak scenarios. The tokamaks chosen here are ASDEX Upgrade (AUG), which is operational in Germany, and ITER, which is currently under construction in France. Specifically, choosing the same plasma and pellet parameters as used by Samulyak (2023) enables direct quantitative comparison. The simulations presented by Samulyak (2023) use a three-dimensional Lagrangian particle code (Samulyak et al., 2021), which is more sophisticated and has a higher computational cost than our scaling laws and formulas.

In both cases, the injected pellets are assumed to consist of pure deuterium. This makes the neutral gas cloud around the pellet a mostly diatomic gas of D_2, which suggests the adiabatic index $\gamma = 7/5$. Deuterium atoms (and ions) have a mass of $\sim 2\,\mathrm{u}$ and the D_2 molecules have a mass of $\sim 4\,\mathrm{u}$, where the atomic mass unit is $1\,\mathrm{u} = 1.661 \times 10^{-27}\,\mathrm{kg}$. Assuming spherical pellets, the pellet rocket force F, leads to an expression for the pellet rocket acceleration as

$$a = \frac{F}{\frac{4}{3}\pi r_\mathrm{p}^3 \rho_\mathrm{p}}\,, \tag{4.88}$$

where $\rho_\mathrm{p} \approx 204\,\mathrm{kg/m^3}$ (Senichenkov et al., 2007) is the typical density of cryogenic deuterium pellets.

Samulyak (2023) presents his results for AUG together with the used pellet radii, plasma temperatures and plasma densities. However, the radial position R_m of the

pellet, the pellet velocity v_p and the gradients have to be assumed here. The plasma in AUG has a major radius of 1.65 m and a minor radius of 0.5 m. Assuming the pellet is close to the low-field side edge, but not in the pedestal[11], a radial position of $R_\mathrm{m} = 2\,\mathrm{m}$ is reasonable. A related experiment performed by Müller et al. (2002) notes radial pellet velocities of $v_\mathrm{p} = 240\,\mathrm{m/s}$, which is thus assumed here. Assuming a linear temperature gradient, with a temperature of 2 keV in the centre and a pedestal height of 50%, we estimate the temperature gradient to be $\frac{\mathrm{d}T_\mathrm{bg}}{\mathrm{d}z} \approx 2\,\mathrm{keV/m}$. The density gradient does not play a significant role and is neglected here.

For the ablation cloud, several additional parameters have to be provided. Based on a simulation by Matsuyama (2022) and experimental observations by Müller et al. (2002) of the ablation dynamics under similar conditions, the ionization radius is estimated as $r_\mathrm{i} \approx 1\,\mathrm{cm}$ (similar to Samulyak's figures) and the plasmoid cloud temperature is estimated as $T_\mathrm{pl} \approx 2\,\mathrm{eV}$. The fraction of electron energy loss going into heating the neutral gas cloud is taken to be $\mu = 0.65$, in line with predictions by Parks and Turnbull (1978).

T_bg (keV)	n_bg ($1/\mathrm{m}^3$)	r_p (mm)	$a_\text{our model}$ ($\mathrm{m/s}^2$)	a_Samulyak ($\mathrm{m/s}^2$)
2.0	6.0×10^{19}	1.0	$(1.45 - 3.92) \times 10^5$	1.7×10^5
2.0	6.0×10^{19}	0.5	$(0.47 - 2.60) \times 10^5$	2.4×10^5
2.2	9.4×10^{19}	0.5	$(0.98 - 4.84) \times 10^5$	7.0×10^5

Table 4.1: Predictions for the pellet rocket acceleration in ASDEX Upgrade in comparison to predictions by Samulyak (2023). The lower estimate is the full model prediction and the upper estimate is the prediction while setting $E_\mathrm{rel} = 0$. Note that, except for the listed parameters, Samulyak (2023) might have used different assumptions and their results are given just for reference.

The results for three different plasma and pellet parameter combinations are listed in table 4.1, together with Samulyak's predictions. In addition to the model prediction as described in the previous sections (lower prediction), an upper prediction is given by assuming that the plasmoid shielding overpredicts the effective energy asymmetry and setting $E_\mathrm{rel} = 0$ in eq. (4.63). This was motivated by the fact that the full model predicts a negative acceleration when neglecting the temperature gradient. The observed overestimation of E_rel could be a result of reducing the Maxwellian-distributed electrons traversing the plasmoid to a mono-energetic beam traversing the neutral cloud. The temperature gradient was found to account for about 10% to 30% of the acceleration when setting $E_\mathrm{rel} = 0$. Overall, the estimates of the pellet rocket acceleration agree reasonably well with the predictions by Samulyak (2023). Experimental observations have shown an average acceleration of $\sim 5 \times 10^5\,\mathrm{m/s}^2$ (Müller et al., 2002). Similar values are obtained in our model, and our compares even better with the experiment than with Samulyak's simulation results.

However, it must be noted that changing the above estimated parameters ($\frac{\mathrm{d}T_\mathrm{bg}}{\mathrm{d}z}$, r_i, T_pl, μ, γ) individually within reasonable ranges can change the prediction by around

[11] The pedestal in a tokamak is the region at the plasma edge, where the density and temperature rapidly increase.

50%. Varying the radial position or pellet velocity does not significantly change the predicted acceleration. Our plasmoid shielding model is particularly sensitive to r_i, where in the last case listed in table 4.1 increasing r_i by $\sim 0.25\,\mathrm{cm}$ causes a_pl to flip sign, which is leads to unphysical results. With this larger ionization radius, our model predicts a plasmoid pressure which is lower than in the background plasma, indicating that the plasmoid would in reality not expand to such a large radius.

Qualitative comparison of the parameter dependence in table 4.1 with Samulyak's results shows a much weaker dependence on T_bg and n_bg in our model. Furthermore, Samulyak's model predicts a larger acceleration for smaller pellets, our model predicts the opposite. However, when a large enough temperature gradient is given, this r_p dependence in our model flips. Resolving these discrepancies is non-trivial. Thorough investigation of how all parameters are involved in our model predictions, i.e. a proper qualitative and quantitative benchmark of our model, is outside the scope of this thesis.

$a_\mathrm{pl}\,(\mathrm{m/s^2})$	$s_0 \pm \delta s\,(r_\mathrm{p})\,(\mathrm{cm})$	f_q	f_E	q_rel	$\frac{E_\mathrm{rel}}{q_\mathrm{rel}}$	$p_\star\,(\mathrm{atm})$
1.6×10^8	18 ± 1.0	0.82	1.39	0.014	-0.75	22
1.1×10^8	22 ± 0.7	0.92	1.22	0.004	-0.97	28
0.9×10^8	23 ± 0.7	0.90	1.26	0.004	-0.94	44

Table 4.2: Predictions of ablation cloud quantities estimated from the plasmoid shielding and isotropic NGS model. The rows correspond to the pellet rocket effect results and parameters listed in table 4.1.

Some of the predicted ablation cloud and shielding quantities are listed in table 4.2, where the rows correspond to the same parameters as listed in table 4.1. The predicted central shielding length in our model of $s_0 \sim 20\,\mathrm{cm}$ with a variation across the pellet of $\delta s\,(r_\mathrm{p}) \sim \pm 1\,\mathrm{cm}$ is in line with Samulyak's prediction. The listed degrees of asymmetry in the heating source, q_rel and E_rel, validate our assumption of the asymmetry in the ablation dynamics being only a small perturbative effect.

Finally, Samulyak also predicts the pellet rocket acceleration for the expected larger pellets in the ITER tokamak. The parameters used are $R_\mathrm{m} = 8\,\mathrm{m}$, $v_\mathrm{p} = 500\,\mathrm{m/s}$, $r_\mathrm{p} = 5\,\mathrm{mm}$, $n_\mathrm{bg} = 10^{20}\,\mathrm{m^{-3}}$, $T_\mathrm{bg} = 5\,\mathrm{keV}$, $\frac{\mathrm{d}n_\mathrm{bg}}{\mathrm{d}z} = 6 \times 10^{19}\,\mathrm{m^{-4}}$ and $\frac{\mathrm{d}T_\mathrm{bg}}{\mathrm{d}z} = 10\,\mathrm{keV/m}$. The rest of the parameters are assumed to be the same as for AUG. The resulting pellet rocket acceleration is predicted in our model to be $\sim 5 \times 10^6\,\mathrm{m/s^2}$ while Samulyak's model predicts $\sim 1 \times 10^6\,\mathrm{m/s^2}$. However, with a larger pellet, the plasmoid cloud could be larger than simulated by Matsuyama (2022), which would give the plasmoid material more time to heat up while drifting across the pellet. Our model shows similar predictions to Samulyak's model, when assuming the plasmoid cloud parameters as $r_\mathrm{i} \approx 3\,\mathrm{cm}$ and $T_\mathrm{pl} \approx 5\,\mathrm{eV}$. This indicates that our model captures the essential physics of the pellet rocket effect, provided that an accurate plasmoid cloud temperature and ionization radius are given.

5

Concluding remarks

In summary, this thesis presented a semi-analytical model for the pellet rocket effect that predicts similar magnitudes of the radial pellet acceleration to those found in earlier simulations and experiments. Evaluating the asymmetry of the ablation cloud and the pellet heating is a remarkably complex physics problem. We have reduced this complexity through theoretical model development, using several assumptions and approximations. This enabled us to develop a model of low computational cost but evaluating the accuracy of the predictions is beyond this thesis.

In this final part of the thesis, the developed model is summarized, and its limitations are discussed in section 5.1. Then, an outlook is given in section 5.2 on how future models of the pellet rocket effect could build on the presented ideas.

5.1 Model summary and discussion

The main premise of our model is the assumption of dominantly isotropic pellet ablation dynamics, onto which a small asymmetric perturbation is added. This is presumably the case in most MCF pellet injection scenarios, and our estimates for the heat source asymmetry in example scenarios confirm this assumption. The perturbative assumption alone is sufficient to derive an expression for the force on the pellet (eq. (4.2)), by considering the fluid dynamical momentum transfer between the pellet surface and its surrounding neutral gas. In an expansion of the neutral gas properties at the pellet surface in terms of spherical harmonics, all contributions orthogonal to the $\cos\theta$ dependence ($l = 1, m = 0$) cancel out. Consequently, only the asymmetries in the pressure and ablation rate contribute to the total force on the pellet.

Building on this assumption, we decided to model the isotropic dynamics of the neutral ablation cloud according to the NGS model as developed by Parks and Turnbull (1978). The involved empirical electron cross-sections directly limit our thesis to the case of hydrogenic pellets. The success of the NGS model in predicting pellet ablation rates suggests that the essential physics is captured well. However, all related approximations had to be carried over to our asymmetric NGS model. While the underlying assumption of quasi-steady state ideal gas dynamics is expected to not differ under asymmetric heating, the two major approximations for the incident electron heat flux might affect the accuracy of our model.

First, instead of treating the electrons kinetically with a Maxwellian energy distribution, this distribution is replaced with a mono-energetic beam for each field line. This approximation leads to a slightly underestimated ablation rate in the isotropic case (Pégourié, 2007), and could therefore lead to an underestimated pellet rocket force in our model.

Second, the flux of electrons through the neutral ablation cloud is expected to follow the magnetic field lines in reality. In the NGS model, this path is replaced by a "fictitious" radial path according to geometric reasoning that the line integrated density is equivalent. This overestimates the ablation rate and thus partially compensates for the error introduced by the mono-energetic beam approximation (Pégourié, 2007). Even though the validity of this approximation in the case of an asymmetric heat flux is unclear, it was needed to make the problem essentially one dimensional and thus solvable semi-analytically. The impact it might have on the accuracy of our model is difficult to evaluate. Additionally, it introduces some ambiguity in how to model the external heat flux asymmetry. Since the neutral ablation cloud dynamics are most important close to the pellet, a reasonable assumption is to quantify the degree of asymmetry by only considering the field lines that hit the pellet surface and artificially "spreading" them over the whole neutral cloud. This could potentially underestimate the asymmetry in the cloud and thus balance the mentioned overestimated ablation rate, as in the isotropic case.

Additionally, Parks and Turnbull (1978) state that only around 60 to 70 percent of the energy lost by electrons in the neutral ablation cloud is transferred as heat, while the rest is lost due to backscattering and emission of radiation. Again, the success of the isotropic NGS model suggests the validity of this assumption. However, this factor enters our expression for the pellet rocket force in a power of 2/3 (through $\mu^{2/3}$ in eq. (4.29)) and could thus affect our predictions significantly.

With assumed boundary conditions of no heat flux onto the cryogenic pellet surface and the external heat source set far away, numerical solutions of the radial dependencies were calculated. Since the dynamical equations are first normalized[1], these numerical solutions span all relevant parameter regions. This means that the essential physical quantities are provided in the form of scaling laws and no costly simulations are needed to use our semi-analytical model (eq. (4.63)).

While the isotropic solutions coincide with the scaling laws provided by Parks and Turnbull (1978), the asymmetric solutions give new insights into the physics of the pellet rocket effect. First, the pressure asymmetry at the pellet surface is found to be linear in the degrees of asymmetry of the external heat flux and average external electron energy. This linearity is presumably a result of the first order perturbation. However, this also means that for a large enough discrepancy in the polarity of both of those asymmetry factors, our model can predict a larger pressure on the side opposite to the higher heat flux. In other words, a pellet could be accelerated towards the more heated side, where the ablation dynamics are driven by more highly energetic electrons on the other side. It remains unclear whether this phenomenon

[1]Normalization to the neutral gas quantities at the sonic radius and the degree of asymmetry in the external heat flux.

of a reversed pellet rocket effect reflects a physical possibility or is an artifact of our approximations.

Another prediction of our model is that the momentum gained by the pellet depends mainly on the pressure asymmetry. The asymmetry in ablation rate is predicted to be 2 to 6 orders of magnitude smaller. This finding opposes the fundamental assumption in the pellet rocket model developed by Senichenkov et al. (2007). It may depend on the boundary conditions at the pellet surface, where we neglected the finite sublimation energy. Again, the physical validity of this result is unclear, but it supports the semi-empirical model developed by Szepesi et al. (2007).

To provide a full model of the pellet rocket effect, the plasmoid shielding and the induced heat flux asymmetry at the neutral-ionized boundary have to be modelled. The developed asymmetric NGS model can in principle be applied to all different hydrogenic pellet acceleration phenomena in MCF plasmas. However, the use case is restricted in this thesis to the pellet rocket effect along the major radius of a tokamak. The drift of the ionized ablated material down the magnetic field gradient is modelled based on the ideas presented by Vallhagen et al. (2023). This leads to an asymmetry in shielding length across the different field lines hitting the pellet. The energy and heat flux attenuation of electrons passing through the plasmoid is then modelled through two major approximations. First, electrons are assumed to be fully stopped if their mean free path[2] is shorter than the shielding length along the field line they follow. Second, the electrons that reach the neutral ablation cloud are assumed not to be slowed down at all in the plasmoid cloud. These assumptions are inspired by the ideas of Senichenkov et al. (2007) and serve as a crude estimate of the plasmoid shielding. While this enables predictions for the heat source at the neutral-ionized boundary, the resulting asymmetry in average electron energy could be highly overestimated. Additionally, the plasmoid temperature and the ionization radius are not modelled in this thesis and are taken as input parameters, which have to be provided by further modelling efforts.

Applying our model to the case of ASDEX Upgrade LFS pellet injection predicts pellet rocket accelerations on the order of $10^5\,\mathrm{m/s^2}$. This result coincides with previous theoretical and experimental efforts. However, we note that overestimating the asymmetry of the electron energy severely decreases the predicted acceleration. When disregarding the temperature gradient in the plasma, our model even predicts an acceleration towards the HFS. Better agreement with previous predictions is obtained when ignoring the predicted asymmetry in average electron energy. Predictions for pellet rocket accelerations in ITER on the order of $10^6\,\mathrm{m/s^2}$ also roughly agree with predictions by Samulyak (2023).

5.2 Outlook

Our predictions confirm the potentially fast pellet deceleration in ITER, which could severely impact the effectiveness of pellet injection schemes in reactor grade devices. This emphasizes the importance of developing accurate models for the pellet rocket

[2]We consider mainly the slowing down due to collisions with the cold plasmoid electrons.

effect. While the accuracy of the presented model could not be fully evaluated yet, several areas of improvement are already clear.

First and foremost, the plasmoid shielding dynamics are considered in a simplified way. This is indicated by the fact that the effect of the average electron energy asymmetry is overestimated enough to cause a reversed pellet rocket effect, which has not yet been observed in experiments or more advanced numerical models. In future modelling efforts, the hot electron dynamics in the cold plasmoid could be treated with a more sophisticated kinetic model.

Additionally, the energy sink due to ionization of the ablated material may be considered. Not only could this better inform the choice of ionization radius and plasmoid temperature, it could also lower the incident electron energy and heat flux.

The important areas for improvement of the asymmetric NGS model are the mono-energetic beam approximation and the replacement of the path along the field lines with an equivalent radial path. The former could be resolved by treating the incident electron dynamics kinetically. While considering a radial heat flux is reasonable in the isotropic case, anisotropic dynamics are very much relevant to the pellet rocket effect. Lifting this latter limitation could be done by solving the full two-dimensional problem numerically, or by finding other ways to project the system of equations onto the $\cos\theta$ dependence.

Finally, further investigation of the pellet rocket effect is also needed on the experimental side. Insights into the ablation cloud dynamics as well as the pellet trajectory could inform theoretical modelling efforts. Proper comparison between theoretical predictions and experimental observations will be needed to develop tools that can inform the planning and operation of pellet injection systems in future fusion reactors.

Bibliography

Baylor, L. R. (2016). *Projected fueling efficiency and implications for a DEMO fusion reactor* [IAEA DEMO Workshop]. URL: https://nucleus.iaea.org/sites/fusionportal/Technical%20Meeting%20Proceedings/4th%20DEMO/website/talks/November%2015%20Sessions/Baylor.pdf

Chen, F. F. (2011). *An indispensable truth*. Springer New York. URL: https://doi.org/10.1007/978-1-4419-7820-2

Chen, F. F. (2016). *Introduction to plasma physics and controlled fusion*. Springer Cham. URL: https://doi.org/10.1007/978-3-319-22309-4

Combs, S. K., Baylor, L. R., Foust, C. R., Gouge, M. J., Jernigan, T. C., Milora, S. L., Artaud, J.-F., & Géraud, A. (1998). *High-field-side pellet injection technology*. Fusion Technology, **34**, 419. URL: https://doi.org/10.13182/FST98-A11963649

Commaux, N., Baylor, L., Jernigan, T., Hollmann, E., Parks, P., Humphreys, D., Wesley, J., & Yu, J. (2010). *Demonstration of rapid shutdown using large shattered deuterium pellet injection in DIII-D*. Nuclear Fusion, **50**, 112001. URL: https://doi.org/10.1088/0029-5515/50/11/112001

Freidberg, J. P. (2007). *Plasma physics and fusion energy*. Cambridge University Press. URL: https://doi.org/10.1017/CBO9780511755705

Gebhart, T. E., Baylor, L. R., & Meitner, S. J. (2020). *Experimental pellet shatter thresholds and analysis of shatter tube ejecta for disruption mitigation cryogenic pellets*. IEEE Transactions on Plasma Science, **48**, 1598. URL: https://doi.org/10.1109/TPS.2019.2957968

Helander, P., & Sigmar, D. J. (2005). *Collisional transport in magnetized plasmas*. Cambridge University Press.

Hender, T., Wesley, J., Bialek, J., Bondeson, A., Boozer, A., Buttery, R., Garofalo, A., Goodman, T., Granetz, R., ... the ITPA MHD, Disruption and Magnetic Control Topical Group. (2007). *Chapter 3: MHD stability, operational limits and disruptions*. Nuclear Fusion, **47**, S128. URL: https://doi.org/10.1088/0029-5515/47/6/S03

Hollmann, E. M., Aleynikov, P. B., Fülöp, T., Humphreys, D. A., Izzo, V. A., Lehnen, M., Lukash, V. E., Papp, G., Pautasso, G., ... Snipes, J. A. (2015). *Status of research toward the ITER disruption mitigation system*. Physics of Plasmas, **22**, 021802. URL: https://doi.org/10.1063/1.4901251

IPCC. (2023). *Summary for policymakers* (Core Writing Team, H. Lee, & J. Romero, Eds.). Climate Change 2023: Synthesis Report. Contribution of Working Groups I, II and III to the Sixth Assessment Report of the Intergovernmental

Panel on Climate Change, 1. URL: https://doi.org/10.59327/IPCC/AR6-9789291691647.001

Ishizaki, R., Nakajima, N., Okamoto, M., & Parks, P. B. (2003). *Fluid simulation on pellet ablation with atomic process*. Journal of Nuclear Materials, **313-316**, 579. URL: https://doi.org/10.1016/S0022-3115(02)01414-9

Kocsis, G., Kálvin, S., Veres, G., Cierpka, P., Lang, P. T., Neuhauser, J., Wittman, C., & Team, A. U. (2004). *A fast framing camera system for observation of acceleration and ablation of cryogenic hydrogen pellet in ASDEX Upgrade plasmas*. Review of Scientific Instruments, **75**, 4754. URL: https://doi.org/10.1063/1.1808897

Lazzaro, E., Gervasini, G., Ghezzi, F., Uccello, A., & JET contributors. (2020). *Rocket effect on dust particles in the tokamak SOL*. Physica Scripta, **95**, 055605. URL: https://doi.org/10.1088/1402-4896/ab5ab2

Li, S., Jiang, H., Ren, Z., & Xu, C. (2014). *Optimal tracking for a divergent-type parabolic PDE system in current profile control*. Abstract and Applied Analysis, **2014**, 1. URL: https://doi.org/10.1155/2014/940965

Maecker, H., Peters, T., & Schenk, H. (1955). *Ionen- und Atomquerschnitte im Plasma verschiedener Gase*. Zeitschrift für Physik, **140**, 119. URL: https://doi.org/10.1007/BF01349371

Matsuyama, A. (2022). *Neutral gas and plasma shielding (NGPS) model and cross-field motion of ablated material for hydrogen–neon mixed pellet injection*. Physics of Plasmas, **29**, 042501. URL: https://doi.org/10.1063/5.0084586

Medina-Roque, D. (2021). *Studies of the dynamics of injected hydrogen pellets in the stellarator TJ-II* [Master's Thesis]. Charles III University of Madrid. URL: https://info.fusion.ciemat.es/MasterThesis/Medina.pdf

Miles, W. T., Thompson, R., & Green, A. E. S. (1972). *Electron-impact cross sections and energy deposition in molecular hydrogen*. Journal of Applied Physics, **43**, 678. URL: https://doi.org/10.1063/1.1661176

Moré, J. J., Garbow, B. S., & Hillstrom, K. E. (1980). *User guide for MINPACK-1* (ANL-80-74). Argonne National Laboratory. URL: https://digital.library.unt.edu/ark:/67531/metadc283470/

Müller, H. W., Dux, R., Kaufmann, M., Lang, P. T., Lorenz, A., Maraschek, M., Mertens, V., Neuhauser, J., & ASDEX Upgrade Team. (2002). *High β plasmoid formation, drift and striations during pellet ablation in ASDEX Upgrade*. Nuclear Fusion, **42**, 301. URL: https://doi.org/10.1088/0029-5515/42/3/311

Panadero, N., Koechl, F., Polevoi, A., Baldzuhn, J., Beidler, C., Lang, P., Loarte, A., Matsuyama, A., McCarthy, K., ... Turkin, Y. (2023). *A comparison of the influence of plasmoid-drift mechanisms on plasma fuelling by cryogenic pellets in ITER and Wendelstein 7-X*. Nuclear Fusion, **63**, 046022. URL: https://doi.org/10.1088/1741-4326/acbc34

Parks, P. B., & Turnbull, R. J. (1978). *Effect of transonic flow in the ablation cloud on the lifetime of a solid hydrogen pellet in a plasma*. The Physics of Fluids, **21**, 1735. URL: https://doi.org/10.1063/1.862088

Parks, P. B., Turnbull, R. J., & Foster, C. A. (1977). *A model for the ablation rate of a solid hydrogen pellet in a plasma*. Nuclear Fusion, **17**, 539. URL: https://doi.org/10.1088/0029-5515/17/3/013

Parks, P., Leffler, J., & Fisher, R. (1988). *Analysis of low Z_a impurity pellet ablation for fusion diagnostic studies*. Nuclear Fusion, **28**, 477. URL: https://doi.org/10.1088/0029-5515/28/3/012

Pégourié, B. (2007). *Review: Pellet injection experiments and modelling*. Plasma Physics and Controlled Fusion, **49**, R87. URL: https://doi.org/10.1088/0741-3335/49/8/R01

Polevoi, A. R., & Shimada, M. (2001). *Simplified mass ablation and relocation treatment for pellet injection optimization*. Plasma Physics and Controlled Fusion, **43**, 1525. URL: https://doi.org/10.1088/0741-3335/43/11/307

Rozhansky, V. A., & Senichenkov, I. Y. (2005). *On the ablation models of fuel pellets*. Plasma Physics Reports, **31**, 993. URL: https://doi.org/10.1134/1.2147645

Samulyak, R., Yuan, S., Naitlho, N., & Parks, P. (2021). *Lagrangian particle model for 3D simulation of pellets and SPI fragments in tokamaks*. Nuclear Fusion, **61**, 046007. URL: https://doi.org/10.1088/1741-4326/abdcd2

Samulyak, R. (2023). *Simulation study of the influence of grad-B drift on pellet ablation dynamics* [Theory and Simulation of Disruptions Workshop]. URL: https://tsdw.pppl.gov/Talks/2023/Samulyak.pdf

Senichenkov, I., Rozhansky, V., & Gusakov, P. (2007). *The pellet rocket acceleration caused by ∇B-induced drift*. Europhysics Conference Abstracts, **31F**, P4.094. URL: https://info.fusion.ciemat.es/OCS/EPS2007/pdf/P4_094.pdf

Shampine, L. F., & Reichelt, M. W. (1997). *The MATLAB ODE suite*. SIAM Journal on Scientific Computing, **18**, 1. URL: https://doi.org/10.1137/S1064827594276424

Szepesi, T., Kálvin, S., Kocsis, G., & Lang, P. T. (2007). *Radial acceleration of solid hydrogen pellets in hot tokamak plasmas*. 34th EPS Conference on Plasma Physics, **31F**, P.4037. URL: https://info.fusion.ciemat.es/OCS/EPS2007/pdf/P4_037.pdf

Vallhagen, O., Pusztai, I., Helander, P., Newton, S. L., & Fülöp, T. (2023). *Drift of ablated material after pellet injection in a tokamak*. Journal of Plasma Physics, **89**, 905890306. URL: https://doi.org/10.1017/S0022377823000466

Vallhagen, O. (2023). *Disruption mitigation in tokamaks with massive material injection* [Licentiate Thesis]. Chalmers University of Technology. URL: https://research.chalmers.se/en/publication/535522

Waller, V., Pégourié, B., Giruzzi, G., Huysmans, G. T. A., Garzotti, L., & Géraud, A. (2003). *Investigation of current-density modification during magnetic reconnection by analysis of hydrogen-pellet deflection*. Physical Review Letters, **91**, 205002. URL: https://doi.org/10.1103/PhysRevLett.91.205002

A

Appendix

A.1 Scaling laws of the NGS model

While the full radial dependence in the NGS model has to be calculated numerically as described in section 4.2.1, the normalization constants, i.e. the quantities at the sonic radius only weakly depend on the energy at the boundary condition E_{bc}, as shown in figs. 4.5 and 4.6. Scaling laws for all dimensionless quantities of importance are provided here for convenience, in the form

$$f(E_{\mathrm{bc}}) = a_0 + a_1 \cdot \log_{10} E_{\mathrm{bc}}\,. \tag{A.1}$$

The coefficients $a_0(\gamma)$ and $a_1(\gamma)$ are provided in table A.1. Especially important for the pellet rocket force is $p_\star$ (eq. (4.29)) and the corresponding prefactor f_p. Note that we have found two small mistakes in the corresponding equations given by Parks and Turnbull (1978). For $v_\star$, they missed a factor of $\sqrt{T_{e0}}$ and for $p_\star$ they missed a factor of $\sim 10^{-12}$.

Table A.1: Coefficients for the scaling laws representing our numerical results when calculating the NGS model. While $\lambda_\star$, r_{p}, E_∞ and q_∞ are the direct results of the numerical procedure described in section 4.2.1, the normalized quantities f_p, f_T, f_v and f_G are the dimensionless prefactors for $p_\star$, $T_\star$, $v_\star$ and G in eqs. (4.29) to (4.32).

γ	a	E_∞	q_∞	$\lambda_\star$	r_p	f_T	f_v	f_p	f_G
5/3	a_0	1.2481	1.5089	0.8828	0.6910	0.2742	0.6781	0.1707	10.7839
	a_1	-0.0315	-0.0070	-0.0272	-0.0255	0.0105	0.0119	-0.0067	0.3004
7/5	a_0	1.2802	1.5711	1.0592	0.7307	0.2193	0.5551	0.1720	10.0397
	a_1	-0.0353	-0.0030	-0.0285	-0.0238	0.0066	0.0079	-0.0061	0.2304
9/7	a_0	1.2939	1.5971	1.1466	0.7470	0.1864	0.4903	0.1614	9.3992
	a_1	-0.0369	-0.0008	-0.0291	-0.0229	0.0050	0.0062	-0.0055	0.1961

The perturbative pressure asymmetry $p_1(r_{\mathrm{p}})$ is found to depend linearly on the heat source asymmetry parameter $E_{\mathrm{rel}}/q_{\mathrm{rel}}$ in section 4.2.3. Linear regression in the form

$$p_1(r_{\mathrm{p}}) = a \cdot \left(\frac{E_{\mathrm{rel}}}{q_{\mathrm{rel}}} - b \right) \tag{A.2}$$

is performed on the numerical results. However, the parameters a and b depend on the parameters γ and E_{bc}, as shown in fig. 4.11. Here, we provide scaling laws for these parameters in the form

$$a = a_0 + a_1 \log_{10} E_{\mathrm{bc}} \tag{A.3}$$

$$b = b_0 + b_1 (\log_{10} E_{\mathrm{bc}})^{b_2} \,. \tag{A.4}$$

The corresponding coefficients are listed in table A.2.

Table A.2: Coefficients for the scaling laws representing the linear fits of the numerical solutions for the perturbative pressure asymmetry $p_1(r_{\mathrm{p}})$.

γ	a_0	a_1	b_0	b_1	b_2
5/3	2.1504	0.1524	-1.1622	-11.3156	-4.8415
7/5	1.8252	0.1066	-1.1624	-9.6307	-4.6843
9/7	1.6999	0.0913	-1.1629	-11.0180	-4.7866

A.2 Asymmetric NGS model expressions derived with SymPy

This section provides the full expressions found for the normalized asymmetric NGS model, as explained in section 4.2.3. Algebraic operations were performed using the Python package SymPy, since the expressions are too large to handle manually. Consider the system of eqs. (4.44) to (4.50) with $l = 1$ and the changes due to normalization listed after eq. (4.53). It describes the normalized perturbation $\vec{y}_1$ to the isotropic NGS model $\vec{y}_0$ and is now written in the form

$$A \frac{\partial \vec{y}_1}{\partial r} = B \vec{y}_1 \quad \text{with} \quad \vec{y}_1 = (p_1, T_1, v_{1,r}, v_{1,\theta}, q_1, E_1)^T \,. \tag{A.5}$$

Since all the following expressions contain only the isotropic NGS model quantities, the subscript 0 is omitted. We also denote $y' = \partial y / \partial r$ and $\lambda = \lambda_\star$. The corresponding matrices are

$$A = \begin{pmatrix} -\frac{v}{T} & \frac{\rho v}{T} & -\rho & 0 & 0 & 0 \\ -\frac{1}{\gamma} & 0 & -\rho v & 0 & 0 & 0 \\ 0 & 0 & 0 & -\rho v & 0 & 0 \\ -\frac{v}{\gamma - 1} - \frac{v^3}{2T} & \frac{\rho v^3}{2T} & -\rho v^2 - k & 0 & \frac{2}{\lambda\,(\gamma - 1)} & 0 \\ 0 & 0 & 0 & 0 & 1 & 0 \\ 0 & 0 & 0 & 0 & 0 & 1 \end{pmatrix} \tag{A.6}$$

and

$$B = \tag{A.7}$$

$$\begin{pmatrix}
\frac{\partial}{\partial r}\left(\frac{1}{T}\right)v + \frac{1}{T}\left(\vec{\nabla}\cdot\vec{v}\right) & -\frac{\partial}{\partial r}\left(\frac{\rho}{T}\right)v - \frac{\rho}{T}\left(\vec{\nabla}\cdot\vec{v}\right) & \frac{2}{r}\rho + \rho' & -\frac{2}{r}\rho & 0 & 0 \\
\frac{v}{T}v' & -\frac{\rho}{T}vv' & \rho v' & 0 & 0 & 0 \\
\frac{1}{\gamma r} & 0 & 0 & \frac{\rho}{r}v & 0 & 0 \\
B_{41} & -\frac{v}{2}\frac{\partial}{\partial r}\left(\frac{\rho v^2}{T}\right) - \frac{\left(\vec{\nabla}\cdot\vec{v}\right)}{2T}\rho v^2 & B_{43} & -\frac{2}{r}k & 0 & 0 \\
\frac{\Lambda}{T}\lambda q & -\frac{\Lambda}{T}\rho\lambda q & 0 & 0 & \Lambda\rho\lambda & \frac{\partial\Lambda}{\partial E}\rho\lambda q \\
\frac{2}{T}L\lambda & -\frac{2}{T}L\rho\lambda & 0 & 0 & 0 & 2\frac{\partial L}{\partial E}\rho\lambda
\end{pmatrix},$$

with

$$B_{41} = \frac{v}{2}\frac{\partial}{\partial r}\left(\frac{v^2}{T}\right) + \left(\vec{\nabla}\cdot\vec{v}\right)\left(\frac{1}{\gamma-1} + \frac{v^2}{2T}\right), \tag{A.8}$$

$$B_{43} = \frac{\partial}{\partial r}\left(\rho v\right)v + \left(\vec{\nabla}\cdot\vec{v}\right)\rho v + \frac{2}{r}k + k'\,. \tag{A.9}$$

We have denoted

$$k = \frac{1}{2}\rho v^2 + \frac{p}{\gamma-1}\,, \tag{A.10}$$

$$\vec{\nabla}\cdot\vec{v} = \frac{1}{r^2}\cdot\frac{d}{dr}(r^2 v)\,. \tag{A.11}$$

Symbolic computation allows us to find an analytic expression for $C = A^{-1}B$ so that

$$\boxed{\frac{\partial\vec{y}_1}{\partial r} = C\vec{y}_1}\,. \tag{A.12}$$

The expressions for matrix C in terms of 3×3 blocks with $w = v^2$ are provided on the next pages.

$$C = \begin{pmatrix} C_{11} & C_{12} \\ C_{21} & C_{22} \end{pmatrix} \tag{A.13}$$

$$C_{11} = \frac{1}{T - v^2} \begin{pmatrix} \frac{2\gamma w}{r} - \frac{2\Lambda\gamma q\sqrt{w}}{T} & \frac{\gamma w'}{2r^2\sqrt{w}} + \frac{2\Lambda\gamma q}{Tr^2} & \frac{\gamma\left(-Tw' + w\left(T' + \frac{\gamma w'}{2} - \frac{w'}{2}\right)\right)}{r^2 w} \\ (D_{11})_{21} & (D_{11})_{22} & (D_{11})_{23} \\ \frac{r\left(-\frac{Trw'}{2} - 2Tw + 2\Lambda q r\sqrt{w} + \frac{rww'}{2}\right)}{T} & \frac{-2\Lambda q - \frac{\sqrt{w}w'}{2}}{T} & \frac{Tw'}{2w} - T' - \frac{\gamma w'}{2} + w' \end{pmatrix} \tag{A.14}$$

(A.15)

$$(D_{11})_{21} = -T'r^2\sqrt{w} + 2\Lambda q r^2 + 2\gamma r w^{3/2} - 2rw^{3/2} + \frac{T'r^2w^{3/2}}{T} - \frac{2\Lambda\gamma q r^2 w}{T} \tag{A.16}$$

$$(D_{11})_{22} = T' - \frac{2\Lambda q}{\sqrt{w}} + \frac{\gamma w'}{2} - \frac{w'}{2} - \frac{T'w}{T} + \frac{2\Lambda\gamma q\sqrt{w}}{T} \tag{A.17}$$

$$(D_{11})_{23} = \frac{-TT' - \frac{3T\gamma w'}{2} + \frac{3Tw'}{2} + T'\gamma w + \frac{\gamma^2 ww'}{2} - \frac{\gamma ww'}{2}}{\sqrt{w}} \tag{A.18}$$

$$C_{12} = \frac{1}{T - v^2} \begin{pmatrix} -\frac{2T\gamma}{r^3} & -\frac{2\Lambda\gamma}{r^2} & -\frac{2\frac{\partial\Lambda}{\partial E}\gamma q}{r^2} \\ \frac{2T\sqrt{w}\,(1-\gamma)}{r} & \frac{2\Lambda\,(T-\gamma w)}{\sqrt{w}} & \frac{2\frac{\partial\Lambda}{\partial E} q\,(T-\gamma w)}{\sqrt{w}} \\ \frac{2T}{r} & 2\Lambda & 2\frac{\partial\Lambda}{\partial E} q \end{pmatrix} \tag{A.19}$$

$$C_{21} = \begin{pmatrix} -\frac{r}{\gamma} & 0 & 0 \\ \frac{\Lambda\lambda q}{T} & -\frac{\Lambda\lambda q}{Tr^2\sqrt{w}} & 0 \\ \frac{2L\lambda}{T} & -\frac{2L\lambda}{Tr^2\sqrt{w}} & 0 \end{pmatrix} \tag{A.20}$$

$$C_{22} = \begin{pmatrix} -\frac{1}{r} & 0 & 0 \\ 0 & \frac{\Lambda\lambda}{r^2\sqrt{w}} & \frac{\frac{\partial\Lambda}{\partial E}\lambda q}{r^2\sqrt{w}} \\ 0 & 0 & \frac{2\frac{\partial L}{\partial E}\lambda}{r^2\sqrt{w}} \end{pmatrix}. \tag{A.21}$$

As can be seen, the first three rows of C share the apparent singularity $1/(T_0 - v_0^2)$ at $r = 1$. We now require that $\vec{y}_1'(r = 1)$ is finite. Defining the singularity-reduced matrix $D = (T_0 - v_0^2)C$, the first three rows of $D(r = 1)$ are

$$D_1(r=1) = \begin{pmatrix} 0 & \gamma\left(\frac{\chi}{2}+2\right) & \gamma\,(2-\chi) & -2\gamma & -2\gamma & -\frac{\Psi\gamma}{L\lambda} \\ 0 & \frac{\chi\,(\gamma-1)}{2}+2\gamma-2 & -\chi\gamma+\chi+2\gamma-2 & 2-2\gamma & 2-2\gamma & \frac{\Psi\,(1-\gamma)}{L\lambda} \\ 0 & -\frac{\chi}{2}-2 & \chi-2 & 2 & 2 & \frac{\Psi}{L\lambda} \end{pmatrix}, \tag{A.22}$$

where χ and Ψ are defined by eq. (4.27) and L is the empirical electron energy loss function of eq. (4.11) normalized through eq. (4.17). This is a matrix of rank 1 and $D(r = 1)\vec{y}_1$ yields

$$\boxed{v_{1,\theta} = \left(1 - \frac{\chi_\star}{2}\right) v_{1,r} + \left(1 + \frac{\chi_\star}{4}\right) T_1 - q_1 - \frac{\Psi_\star}{2\lambda_\star L(E=1)} E_1}. \tag{A.23}$$

This is used in the numerical procedure for solving for $\vec{y}_1(r)$ to reduce the number of unknowns at the sonic radius by one.

To be able to calculate the derivatives $\vec{y}_1'(r = 1)$, we need to apply L'Hôpital's rule in the sense

$$\begin{aligned} \lim_{r\to1} \vec{y}_1' &= \lim_{r\to1} \frac{1}{\frac{d}{dr}(T-w)} \frac{d}{dr}\left(D\vec{y}_1\right) \\ \Leftrightarrow \lim_{r\to1} \vec{y}_1' &= \lim_{r\to1} \frac{1}{\frac{d}{dr}(T-w)} \left(D'\vec{y}_1 + D\vec{y}_1'\right) \\ \Leftrightarrow \lim_{r\to1} \left(\frac{d}{dr}(T-w)\mathbb{1}_{6x6} - D\right) \vec{y}_1' &= \lim_{r\to1} D'\vec{y}_1 \\ \Leftrightarrow \lim_{r\to1} \vec{y}_1' &= \lim_{r\to1} \left(\frac{d}{dr}(T-w)\mathbb{1}_{6x6} - D\right)^{-1} D'\vec{y}_1. \end{aligned}$$

So we need to find $D'(r = 1)$ and $\left(\frac{d}{dr}(T - w)\mathbb{1}_{6x6} - D\right)^{-1}|_{r=1}$. We also define the matrix

$$C_\star = \lim_{r\to1} \left(\frac{d}{dr}(T-w)\mathbb{1}_{6x6} - D\right)^{-1} D' \tag{A.24}$$

$$\text{so that} \quad \Rightarrow \quad \boxed{\vec{y}_1'(r=1) = C_\star \vec{y}_1(r=1)}. \tag{A.25}$$

We now define $\Xi = 4\lambda L^2|_{E=1} \frac{d^2\Lambda}{dE^2}|_{E=1}$ and provide the resulting large expressions for the elements of $C_\star$ on the next pages.

$$C_{\star(4-6)(1-6)} = \begin{pmatrix} -\frac{1}{\gamma} & 0 & 0 & -1 & 0 & 0 \\ \lambda & -\lambda & 0 & 0 & \lambda & \frac{\Psi}{2L} \\ 2L\lambda & -2L\lambda & 0 & 0 & 0 & 2\lambda \left.\frac{\partial L}{\partial \xi}\right|_{\xi=1} \end{pmatrix}$$

$$C_{\star 11} = \frac{16\Psi\gamma - \chi^2\gamma^2 - \chi^2\gamma + 16\gamma\lambda - 8\gamma - 8}{4\left(\chi\gamma + \chi + 2\gamma - 6\right)}$$

$$C_{\star 12} = \frac{\gamma\left(-16\Psi\chi\gamma - 16\Psi\chi + 64\Psi + \chi^3\gamma^2 + 4\chi^3\gamma + \chi^3 + 8\chi^2\gamma - 12\chi^2 - 16\chi\gamma\lambda + 80\chi\gamma - 16\chi\lambda + 64\gamma + 64\lambda - 256\right)}{4\left(\chi^2\gamma^2 + 2\chi^2\gamma + \chi^2 + 2\chi\gamma^2 - 8\chi\gamma - 10\chi - 8\gamma + 24\right)}$$

$$C_{\star 13} = \frac{\gamma\left(-4\Psi\chi\gamma - 4\Psi\chi + 16\Psi - \chi^3\gamma^2 - 4\chi^3\gamma - \chi^3 + 4\chi^2\gamma + 12\chi^2 - 4\chi\gamma\lambda + 16\chi\gamma - 4\chi\lambda + 24\chi + 32\gamma + 16\lambda - 128\right)}{2\left(\chi^2\gamma^2 + 2\chi^2\gamma + \chi^2 + 2\chi\gamma^2 - 8\chi\gamma - 10\chi - 8\gamma + 24\right)}$$

$$C_{\star 14} = \frac{\gamma\left(-\chi^2\gamma^2 - \chi^2\gamma + 2\chi^2 - 8\chi\gamma - 8\chi - 16\gamma + 48\right)}{\chi^2\gamma^2 + 2\chi^2\gamma + \chi^2 + 2\chi\gamma^2 - 8\chi\gamma - 10\chi - 8\gamma + 24}$$

$$C_{\star 15} = \frac{2\gamma\left(\Psi\chi\gamma + \Psi\chi - 4\Psi - \chi^2\gamma + \chi\gamma\lambda - 8\chi\gamma + \chi\lambda - 2\chi - 8\gamma - 4\lambda + 32\right)}{\chi^2\gamma^2 + 2\chi^2\gamma + \chi^2 + 2\chi\gamma^2 - 8\chi\gamma - 10\chi - 8\gamma + 24}$$

$$C_{\star 16} = \frac{\gamma\left(-\Psi\chi^2\gamma + 2\Psi\chi\gamma\lambda \left.\frac{\partial L}{\partial \xi}\right|_{\xi=1} + 2\Psi\chi\gamma\lambda - 8\Psi\chi\gamma + 2\Psi\chi\lambda \left.\frac{\partial L}{\partial \xi}\right|_{\xi=1} + 2\Psi\chi\lambda - 2\Psi\chi - 8\Psi\gamma - 8\Psi\lambda \left.\frac{\partial L}{\partial \xi}\right|_{\xi=1} - 8\Psi\lambda + 32\Psi + \Xi\chi\gamma\lambda + \Xi\chi\lambda - 4\Xi\lambda\right)}{L\lambda\left(\chi^2\gamma^2 + 2\chi^2\gamma + \chi^2 + 2\chi\gamma^2 - 8\chi\gamma - 10\chi - 8\gamma + 24\right)}$$

$$C_{\star 21} = \frac{16\Psi\gamma^2 - 16\Psi\gamma + \chi^2\gamma^3 - \chi^2\gamma + 4\chi\gamma^3 - 16\chi\gamma^2 + 12\chi\gamma + 16\gamma^2\lambda - 8\gamma^2 - 16\gamma\lambda + 8}{4\gamma\left(\chi\gamma + \chi + 2\gamma - 6\right)}$$

$$C_{\star 22} = \frac{-16\Psi\chi\gamma^2 + 16\Psi\chi + 64\Psi\gamma - 64\Psi - \chi^3\gamma^3 - \chi^3\gamma^2 - \chi^3\gamma + 3\chi^3 - 4\chi^2\gamma^3 + 8\chi^2\gamma^2 - 4\chi^2 - 16\chi\gamma^2\lambda + 32\chi\gamma^2 - 16\chi\gamma + 16\chi\lambda - 16\chi + 64\gamma\lambda - 64\gamma - 64\lambda + 64}{4\chi^2\gamma^2 + 8\chi^2\gamma + 4\chi^2 + 8\chi\gamma^2 - 32\chi\gamma - 40\chi - 32\gamma + 96}$$

$$C_{\star 23} = \frac{\left(\chi\gamma + 3\chi - 8\right)\left(-4\Psi\gamma + 4\Psi - \chi^2\gamma^2 + \chi^2\gamma + 2\chi\gamma - 6\chi - 4\gamma\lambda + 4\lambda + 8\right) + \left(\chi\gamma - \chi - 2\gamma + 2\right)\left(8\Psi + \chi^2\gamma + \chi^2 - 8\chi + 8\lambda\right)}{2\left(\chi^2\gamma^2 + 2\chi^2\gamma + \chi^2 + 2\chi\gamma^2 - 8\chi\gamma - 10\chi - 8\gamma + 24\right)}$$

$$C_{\star 24} = \frac{\chi\left(-\chi\gamma^3 + 2\chi\gamma^2 + 3\chi\gamma - 4\chi + 4\gamma^2 - 16\gamma + 12\right)}{\chi^2\gamma^2 + 2\chi^2\gamma + \chi^2 + 2\chi\gamma^2 - 8\chi\gamma - 10\chi - 8\gamma + 24}$$

$$C_{\star 25} = \frac{2\left(-2\Psi\left(\chi\gamma - \chi - 2\gamma + 2\right) + \lambda\left(\gamma - 1\right)\left(\chi\gamma + \chi - 4\right) + \left(\chi\gamma + 3\chi - 8\right)\left(\Psi\gamma - \Psi + \chi\gamma - 2\right)\right)}{\chi^2\gamma^2 + 2\chi^2\gamma + \chi^2 + 2\chi\gamma^2 - 8\chi\gamma - 10\chi - 8\gamma + 24}$$

$$C_{\star 26} = \frac{\lambda\left(2\Psi\left(\gamma - 1\right)\left(\chi\gamma + \chi - 4\right)\left.\frac{\partial L}{\partial \xi}\right|_{\xi=1} + \Psi\left(\gamma - 1\right)\left(\chi\gamma + \chi - 4\right) - 2\left(\Psi + \Xi\right)\left(\chi\gamma - \chi - 2\gamma + 2\right)\right) - \frac{1}{2}\left(\Psi\left(\chi\left(\gamma - 1\right) - \chi\left(3\gamma - 1\right) + 4\right) - 2\lambda\left(\Psi + \Xi\right)\left(\gamma - 1\right)\right)\left(\chi\gamma + 3\chi - 8\right)}{L\lambda\left(\chi^2\gamma^2 + 2\chi^2\gamma + \chi^2 + 2\chi\gamma^2 - 8\chi\gamma - 10\chi - 8\gamma + 24\right)}$$

$$C_{\star 31} = \frac{-16\Psi\gamma - \chi^2\gamma^2 - \chi^2\gamma - 4\chi\gamma^2 + 12\chi\gamma - 16\gamma\lambda + 8\gamma + 8}{4\gamma\left(\chi\gamma + \chi + 2\gamma - 6\right)}$$

$$C_{\star 32} = \frac{4\Psi\chi\gamma + 4\Psi\chi - 16\Psi + \frac{\chi^3\gamma^2}{4} + \frac{\chi^3}{4} + \chi^2\gamma^2 - 4\chi^2\gamma + 4\chi\gamma\lambda - 12\chi\gamma + 4\chi\lambda + 8\chi - 16\lambda + 16}{\chi^2\gamma^2 + 2\chi^2\gamma + \chi^2 + 2\chi\gamma^2 - 8\chi\gamma - 10\chi - 8\gamma + 24}$$

$$C_{\star 33} = \frac{2\Psi\chi\gamma + 2\Psi\chi - 8\Psi + \chi^3\gamma - \chi^2\gamma^2 - 2\chi^2\gamma - 5\chi^2 + 2\chi\gamma\lambda - 4\chi\gamma + 2\chi\lambda + 8\chi - 8\lambda + 16}{\chi^2\gamma^2 + 2\chi^2\gamma + \chi^2 + 2\chi\gamma^2 - 8\chi\gamma - 10\chi - 8\gamma + 24}$$

$$C_{\star 34} = \frac{\chi^2\left(\gamma^2 + \gamma - 2\right)}{\chi^2\gamma^2 + 2\chi^2\gamma + \chi^2 + 2\chi\gamma^2 - 8\chi\gamma - 10\chi - 8\gamma + 24}$$

$$C_{\star 35} = \frac{2\left(-2\Psi\left(\chi\gamma + 2\gamma - 4\right) - \lambda\left(\chi\gamma + \chi - 4\right) + \left(\chi + 4\right)\left(\Psi\gamma - \Psi + \chi\gamma - 2\right)\right)}{\chi^2\gamma^2 + 2\chi^2\gamma + \chi^2 + 2\chi\gamma^2 - 8\chi\gamma - 10\chi - 8\gamma + 24}$$

$$C_{\star 36} = \frac{\lambda\left(-2\Psi\left(\chi\gamma + \chi - 4\right)\left.\frac{\partial L}{\partial \xi}\right|_{\xi=1} - \Psi\left(\chi\gamma + \chi - 4\right) - 2\left(\Psi + \Xi\right)\left(\chi\gamma + 2\gamma - 4\right)\right) - \frac{1}{2}\left(\chi + 4\right)\left(\Psi\left(\chi\left(\gamma - 1\right) - \chi\left(3\gamma - 1\right) + 4\right) - 2\lambda\left(\Psi + \Xi\right)\left(\gamma - 1\right)\right)}{L\lambda\left(\chi^2\gamma^2 + 2\chi^2\gamma + \chi^2 + 2\chi\gamma^2 - 8\chi\gamma - 10\chi - 8\gamma + 24\right)}.$$

A.3 Asymmetric NGS model parameter scan results

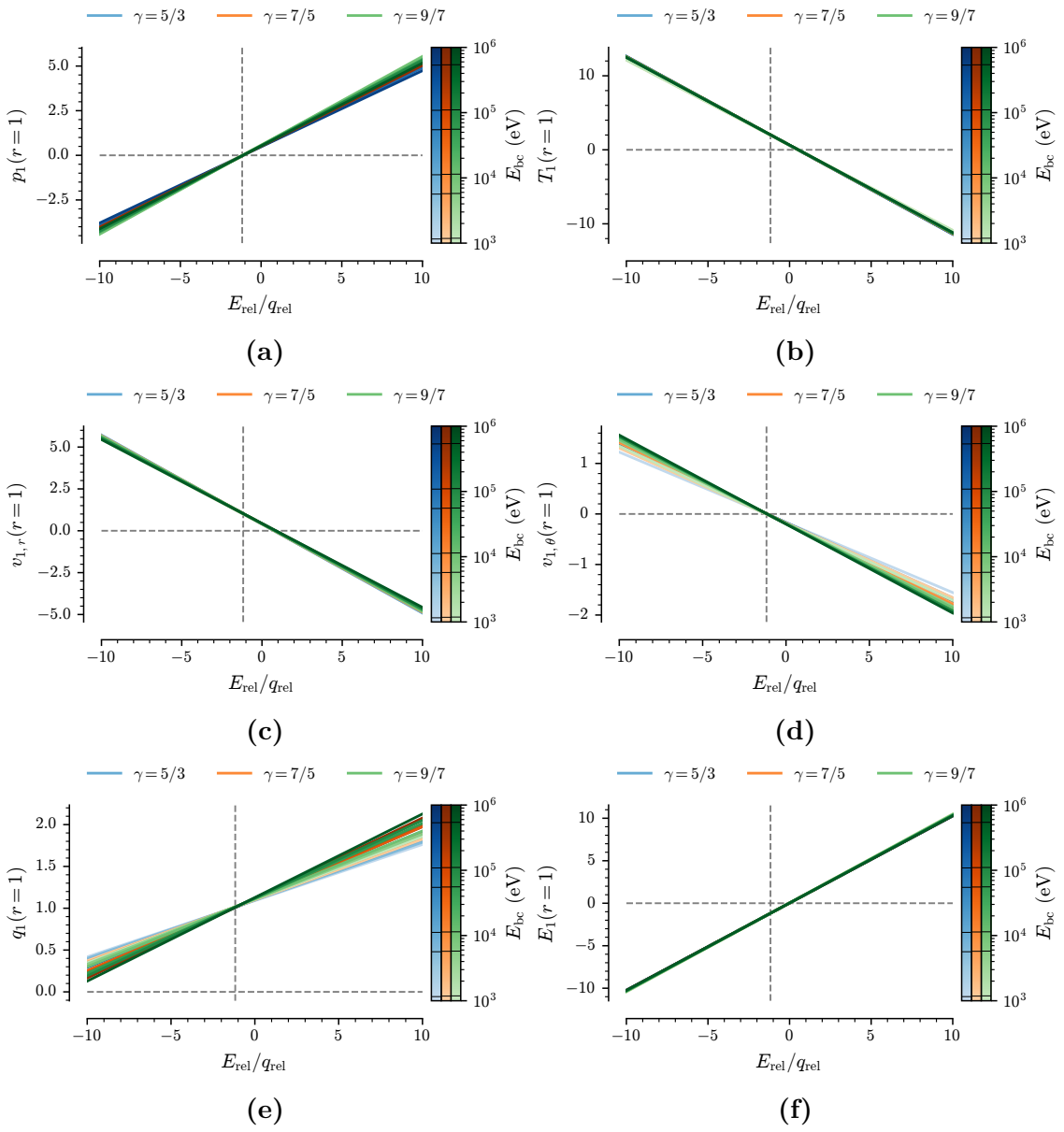

Figure A.1: Optimized sonic values $y_1(r = 1)$ of our asymmetric perturbation model for the neutral ablation cloud dynamics. The relation to $E_{\mathrm{rel}}/q_{\mathrm{rel}}$ is shown to be linear, while γ and $E_\star(E_{\mathrm{bc}})$ change the slope slightly. The vertical dashed line is at $E_{\mathrm{rel}}/q_{\mathrm{rel}} = -1.17$, which is the value where $p_1(r_{\mathrm{p}})$, i.e. the pellet rocket force, becomes negative. Note that $v_{1,\theta}(r = 1)$ shares the same root.

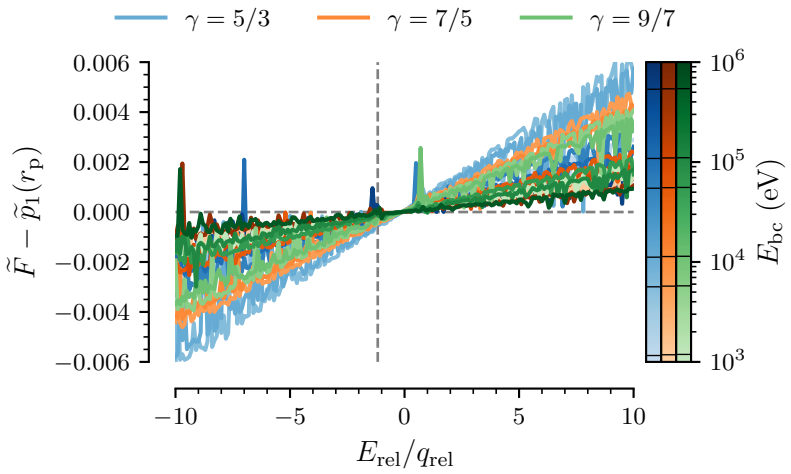

Figure A.2: Contribution of the mass flow to the normalized pellet rocket force in eq. (4.62). Together with figs. 4.10 and 4.12 this indicates that the pressure asymmetry is the dominating contribution to the rocket effect in our asymmetric NGS model.

DEPARTMENT OF PHYSICS
CHALMERS UNIVERSITY OF TECHNOLOGY
Gothenburg, Sweden
www.chalmers.se

CHALMERS
UNIVERSITY OF TECHNOLOGY